Design and Synthesis of Photoactive Metal-Organic Frameworks for Photon Upconversion and Energy Transfer Studies

Jennifer Maria Rowe

Thesis submitted to the faculty of the Virginia Polytechnic Institute and State University in partial fulfillment of the requirements for the degree of

Doctor of Philosophy
In
Chemistry

Amanda J. Morris, Chair
Brian M. Tissue
John R. Morris
James M. Tanko

April 26, 2018
Blacksburg, VA

Keywords: Metal-Organic Frameworks, Photophysics, Photon Upconversion, Energy Transfer

Design and Synthesis of Photoactive Metal-Organic Frameworks for Photon Upconversion and Energy Transfer Studies

Jennifer Maria Rowe

Abstract: The synthesis, characterization and photophysical properties of three Zr-based Metal-organic frameworks (MOFs) assembled from 2,6-anthracenedicarboxylic acid (2,6-ADCA, 2,6-MOF) and 1,4-anthracenedicarboxylic (1,4-ADCA, 1,4-MOF), and 9,10-anthracenedicarboxylic acid (9,10-ADCA, 9,10-MOF) are described. The crystal structure of the 9,10-MOF was elucidated by synchrotron powder X-ray diffraction (PXRD) analysis and is isostructural with the well-known UiO-66 framework. The 2,6-MOFs also form highly crystalline, octahedral-shaped structures and was characterized by PXRD. Le Bail refinement of the powder pattern revealed that the 2,6-MOF also has UiO-type crystal structure. Conversely, incorporation of the 1,4-ADCA ligand results in large rod-shaped crystals. The excited-state properties of the MOFs were examined using stead-state diffuse reflectance, steady-state emission spectroscopy and time-correlated single photon counting (TCSPC) spectroscopy and are compared to those of the corresponding ligand in solution. Both the unique fluorescent properties of the ligand as well as individual framework structure, result in distinctive luminescent behavior and dictate the extent of intermolecular interactions. Specifically, the 2,6-MOF displays monomeric emission with a fluorescence lifetime (τ) of 16.6 ± 1.1 and fluorescence quantum yield (Φ_f). On the other hand, the 1,4-MOF displays both monomeric and excimeric emission, with corresponding lifetime values of 7.5 ± 0.01 and 19.9 ± 0.1, respectively and a quantum yield of 0.002 ± 0.0001.

The propensity for photon upconversion through sensitized triplet-triplet annihilation (TTA-UC) was probed in the three anthracene-based MOFs. The MOFs were surface-modified with Pd(II) mesoporphyrin IX (PdMP) as the triplet sensitizer. Upconverted emission from the 9,10-MOF was observed, with a quantum efficiency (Φ_{UC}) of 0.46 % and a threshold intensity (I_{th})

of 142 mW/cm^2. The variation of the spacing between the anthracene units in the MOFs was found to have significant impact on TTA-UC. As a result, upconverted emission is only displayed by the 9-10-MOF. The distance between anthracene linkers in the 2,6-MOF are too large for TTA to occur, while the short distances in the 1,4-MOF inhibit upconversion through competitive excimer formation.

To further explore the effects of chromophore spacing on energy transfer processes, a series of zinc-based mixed-ligand MOF were constructed from Zn(II) tetrakis(4-carboxyphenyl)porphyrin (ZnTCPP) and pyrazine, 2,2′-bipyridine (pyz) or 4,4′-bipyridyl (bpy) or 1,4-di(4-pyridyl)benzense (dpbz), comprising ZnTCPP/Zn paddlewheel layers. Across this series, the porphyrin spacing was approximately 6 Å, 11 Å and 16 Å for pyz, bpy and dpbz, respectively. The photophysical properties of the MOFs were explored using stead-state diffuse reflectance spectroscopy and steady-state and time-resolved emission spectroscopies. Florescence quenching studies examined the correlation between porphyrin spacing and efficiency of energy transfer.

Design and Synthesis of Photoactive Metal-Organic Frameworks for Photon Upconversion and Energy Transfer Studies

Jennifer Maria Rowe

General Abstract: Metal-organic frameworks (MOFs) are crystalline materials composed of metal clusters connected by organic molecules. Their modular nature and synthetic tunability allows for rational design of MOFs with different functionalities and has afforded their application in a variety of fields including gas storage and separation, catalysis, optoelectronics, energy conversion and storage, chemical sensing and biomedicine. MOFs provide an ideal platform for studying the structure-property relationships that govern energy-transfer processes. Furthermore, efficient and long-ranging, directional energy transfer has been demonstrated in MOFs. The work presented in this dissertation focuses on MOFs with applications in solar energy conversion schemes. The design and synthesis of photoactive MOFs is described and the effects of their structure on energy-transfer processes is explored.

Photovoltaic cells (PVCs) absorb sunlight and convert it into electricity. However, only photons that are high enough in energy are absorbed by the PVC, while the lower energy photons are not absorbed and therefore do not contribute to power production, resulting in decreased efficiency of the solar cell. One approach to enhancing solar cell efficiencies is to collect the lower energy photons and convert them into higher energy photons through a process called sensitized photon upconversion (UC). This process involves a molecule (sensitizer chromophore) that absorbs lower-energy photons and then transfers the absorbed energy to a second molecule (acceptor chromophore), which emits higher-energy photons. In order to understand how to optimize the efficiency of the UC process, we integrated sensitizer and acceptor chromophores

into MOFs various molecular arrangements and probed UC in these materials. Close proximity and he appropriate orientation between chromophores resulted in UC from the framework.

Natural photosynthetic systems contain highly ordered arrays of chromophores that efficiently absorb sunlight and funnel the energy to a reaction center. Energy-harvesting materials that mimic natural photosynthetic processes also have potential applications in solar energy conversion. Porphyrins are often used in artificial photosynthetic systems because of their similarity to chlorophyll pigments found in nature. In order to design highly efficient artificial photosynthetic systems, we first need to understand how energy transfer processes are influenced by the structure of the system. Therefore, we synthesized a series of MOFs containing Zn-porphyrin layers at varied distances and examined the effects of distance between porphyrin layers on the energy-transfer processes within the MOFs. This work provides insight into the structure-property relationships in photoactive MOFs that can serve as a guide for the rational design of light-harvesting MOFs in future studies.

Acknowledgements

I would first like to thank my advisor, Dr. Amanda Morris. Thank you for the guidance and encouragement you have provided me throughout my research. I am extremely grateful for all you have taught me and how you have helped me grow as a scientist throughout my time in graduate school. I would like to express my gratitude to Dr. Brian Tissue, Dr. John Morris and Dr. James Tanko. Thank you for your feedback and the helpful insight you have provided as my committee members. I also wish to extend my gratitude to the members of the Morris group. Thank you for all the valuable feedback and discussions as well as the encouragement you have offered me. Finally, I would like to thank my parents for the support and encouragement you have given me throughout my life, especially during my years in graduate school.

Table of Contents

List of Figures

List of Tables

List of Abbreviations

ADCA = anthracenedicarboxylic acid

ADC^{2-} = anthracenedicarboxylate

bdc = 1,4-benzenedicarboxylate

BET = Brunauer–Emmett–Teller

bpdc = biphenyl-4,4′-dicarboxylate

bpy = 4,4′-bipyridyl

dcbpy = 2,2′-bipyridine-5,5′-dicarboxylic acid

DMF = *N*,*N*′-dimethylformamide

dpa = 9,10-dipyridyl anthracene

dpbz = 1,4-di(4-pyridyl)benzene

ES = excited state

ET = energy transfer

GS = ground state

HOMO = highest occupied molecular orbital

I_{th} = threshold intensity

IC = internal conversion

ISC = intersystem crossing

LMCT = ligand-to-metal charge transfer

LUMO = lowest unoccupied molecular orbital

MLCT = metal-to-ligand charge transfer

MOF = metal-organic framework

NMR = nuclear magnetic resonance

PdMP = Pd(II) mesoporphyrin IX

PdOEP= palladium(II) octaethylporphyrin

pyz = pyrazine

PXRD = powder X-ray diffraction

SBU = secondary building unit

SEM = scanning electron microscopy

TCSPC = time-correlated sing-photon counting

TGA = thermogravimetric analysis

TTA = triplet-triplet annihilation

TTET = triplet-triplet energy transfer

UC = upconversion

vr = vibrational relaxation

XRD = X-ray diffraction

ZnTCPP = Zn(II)tetrakis(4-carboxyphenyl)porphyrin

λ = wavelength

τ = excited-state lifetime

Φ = quantum yield

Attributions

Chapter 2 of this dissertation was adapted from a manuscript published in the Canadian Journal of Chemistry as part of a special issue on electron donor-acceptor interactions. Erin M. Soderstrom assisted with the synthesis of the anthracene-based ligands and the MOFs. Jie Zhu performed gas sorption and TGA measurements of the MOFs. Pavel M. Usov aided in the structural analysis of the MOFs and contributed the PXRD refinement, data interpretation and writing in this section.

The third chapter was adapted from a manuscript, under review at Chemical Communications. Erin M. Soderstrom provided assistance with ligand and MOF syntheses, Jie Zhu performed TGA and gas sorption measurements and assisted in the PXRD analysis and data interpretation and contributed to writing. Dr. Wenqian Xu (Argonne National Laboratory) performed the synchrotron PXRD measurements and structural analysis and also contributed to writing in this section. Yakovenko, Andrey Andreyevic has developed an "Difference Envelope Density" method and applied to several MOF structures to illustrate the solvent distribution.

The results presented in chapter 4 are a portion of a manuscript in preparation. The single-crystal X-ray data was collected by Jeanette Krause (University of Cincinnati). Carla Slebodnick provided the single-crystal data analysis. Erin M. Soderstrom assisted in synthesis of the MOFs. Bradley Gibbons and Jie collected synchrotron PXRD data.

1. Introduction

The development of materials capable of efficient light absorption and energy transfer has application in a wide range of fields, including photovoltaics, photocatalysis, sensors, and optoelectronics. Metal–organic frameworks (MOFs), which are crystalline materials composed of metal ions or clusters linked together by organic ligands, are ideal candidates for rationally designed light-harvesting energy transfer systems. Photoactive ligands or guest molecules can be incorporated into MOFs and the molecular conformations, orientations and distances between chromophores can be determined crystallographically. Furthermore, these properties may be systematically tuned by ligand design and/or synthetic conditions.[1-4] This chapter will focus on energy transfer processes in MOFs with application in artificial photosynthesis and photon upconversion, and the relationship between their structural and photophysical properties will be discussed.

In nature, photosynthesis is initiated by light-harvesting arrays of antenna chromophores, such as chlorophylls and carotenoids, that absorb sunlight and funnel the energy to the reaction centers with > 95% efficiency.[5] Artificial light-harvesting systems, that mimic this highly efficient process have been of interested for their application in solar energy conversion systems. Due to their highly ordered, crystalline nature and synthetic tunability MOFs provide an excellent platform for designing artificial photosynthetic systems.

1.1. Excited-State Dynamics

The electronic states of a molecule and the transitions between them can be illustrated using a Jablonski diagram, shown in Figure 1.1.1. When a molecule in its singlet ground state (^{1}GS) absorbs a photon with the appropriate energy, it is promoted to the singlet excited state (^{1}ES). The ^{1}ES molecule may return to the ^{1}GS through radiative (fluorescence) or non-radiative decay

processes (internal conversion, IC) or may undergo intersystem crossing (ISC) to the triplet excited state (^{3}ES). The ^{3}ES is then deactivated through phosphorescence and/or IC.[6-7]

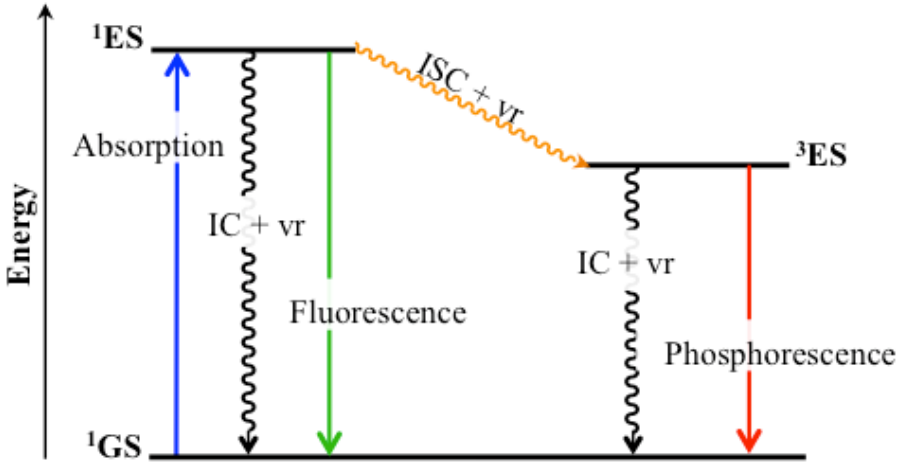

Figure 1.1.1. Jablonski diagram illustrating photoexcitation of a molecule from the ground state (^{1}GS) into the singlet excited state (^{1}ES) and possible deactivation pathways including fluorescence, internal conversion (IC), vibronic relaxation (vr), and intersystem crossing (ISC) to the triplet excited state followed by deactivation through ISC or phosphorescence.

1.2. Excited-State Energy Transfer Processes

1.2.1. Resonance Energy Transfer

Energy transfer between two molecules can occur through either coulombic or resonance interaction (Förster-type) or electron exchange (Dexter-type).[6-8] Resonance energy transfer (Figure 1.2.1.a) results from long-range (~ 10 – 100 Å) dipole-dipole interactions between an excited-state donor and ground-state acceptor. The distance at which energy transfer and spontaneous decay rates are equivalent (i.e. energy transfer efficiency is 50%) is known as the Förster distance and is given by equation 1.2.1 where N_D is Avogadro's number, κ is the dipole orientation factor, Φ_D is the quantum yield of the donor in the absence of acceptor, n is the

refractive index and J is the overlap integral between the normalized spectra of the donor emission and acceptor absorption.

$$R_0{}^6 = \frac{9(ln10)}{128\pi^5 N_D}\left(\frac{\kappa^2 \Phi_D}{n^4}\right)J \tag{1.2.1}$$

The resonance energy transfer rate constant (k_{RET}) is determined by equation 1.2.2 where τ_D is the lifetime of the donor in the absence of the acceptor and r is the distance between the donor and acceptor molecules.

$$k_{RET} = \frac{1}{\tau_D}\left(\frac{R_0}{r}\right)^6 \tag{1.2.2}$$

Thus, the rate constant for resonance energy transfer is directly proportional to r^{-6}. The energy transfer efficiency (η_{RET}) between a donor-acceptor pair at a fixed distance can be determined from the ratio of the donor lifetime in the presence (τ_{DA}) and absence (τ_D) of the acceptor using equation 1.2.3.[7]

$$\eta_{RET} = 1 - \left(\frac{\tau_{DA}}{\tau_D}\right) \tag{1.2.3}$$

According to the spin selection rule, electronic transitions can only occur between states of the same multiplicity.[6] Moreover, because this process also depends on oscillator strength, only singlet-singlet energy transfer traditionally occurs by this mechanism. On the other hand, the electron exchange mechanism offers a means by which either singlet-singlet or triplet-triplet energy transfer can take place. The spin selection rule may be relaxed through spin-orbit coupling, where the presence of a heavy atom induces coupling of the electronic spin angular momentum and orbital angular momentum, giving rise to weak spin-forbidden bands. The symmetry selection rule states that, if a molecule has a center of symmetry, transitions within a set of p or d orbitals are forbidden. Relaxation of the symmetry selection rule occurs via vibronic coupling, in which

allowed vibrations result in molecular asymmetry, or through mixing of. π-acceptor and π-donor ligands with the d-orbitals causing the transitions to no longer be purely d-d.[6-7]

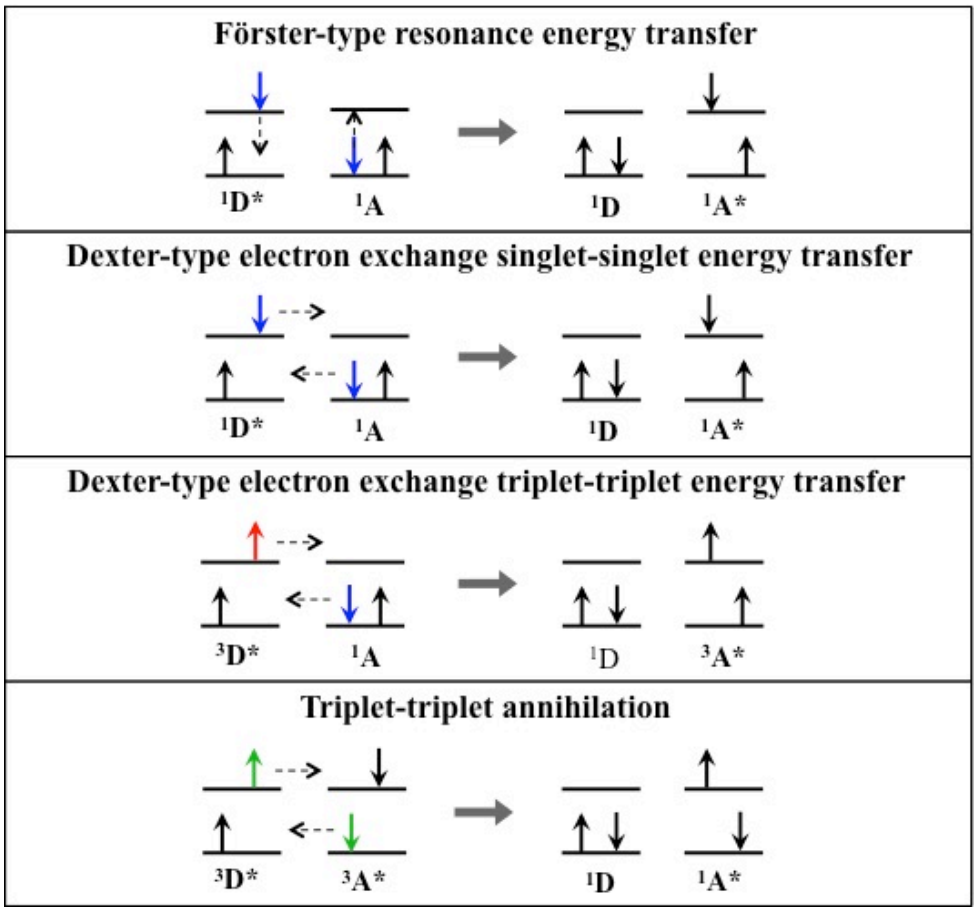

Figure 1.2.1. Schematic representation of energy transfer atomic orbitals and electron configurations involved in the (a) Forster-type, (b) singlet-singlet Dexter-type and (c) triplet-triplet Dexter-type energy transfer mechanisms and (d) triplet-triplet annihilation.

1.2.2. Electron-Exchange Energy Transfer

The Dexter-type mechanism (Figure 1.2.1.b and c) is an electron-exchange process in which an electron moves from the LUMO of a donor, initially in the excited state, to the LUMO of an acceptor in the ground state and an electron from the acceptor HOMO to the donor HOMO. While resonance energy transfer can occur over long donor-accepter distances, energy transfer via an electron exchange mechanism occurs at much shorter distances (< 10 Å), since overlap between

donor and acceptor wavefunctions is required. However, in both cases, the rate of energy transfer is dependent on the overlap integral, *J*. The rate of exchange energy transfer (k_{EET}) decreases exponentially as donor-acceptor distance increases and is given by equation 1.2.4, where *K* is a factor related to specific electronic coupling interactions between the excited states of the donor and acceptor molecules, *J* is the overlap integral, *r* is the donor-acceptor separation distance and *L* is the sum of the Van der Waals radii.[6, 8]

$$k_{EET} = KJ\ exp\left(\frac{-2r}{L}\right) \tag{1.2.4}$$

1.2.2.1. Triplet-Triplet Annihilation

Triplet-triplet annihilation (TTA, Figure 1.2.1) is also an electron exchange process however, in this case, both molecules are initially in the triplet-excited state. This electron exchange process results in a ground state donor and a singlet excited state acceptor. This phenomenon was first discovered in solutions of phenanthrene and anthracene by Parker and Hatchard in 1962.[9] In recent years, TTA has gained increased attention after it was proposed as a means of improving energy conversion efficiencies of photovoltaics through sensitized photon upconversion based on TTA.[10]

1.2.3. Photon Upconversion via Sensitized Triplet-Triplet Annihilation

Sensitized TTA-based photon upconversion (TTA-UC) is a process in which lower-energy light is converted into higher-energy light. The processes involved in TTA-UC are illustrated in Figure 1.2.2. In this mechanism, two sensitizer/donor molecules each absorb a lower-energy photon and undergo ISC to the triplet excited state. Two nearby acceptor/annihilator molecules are promoted from the ground state directly into the triplet excited states via Dexter-type triplet-triplet energy transfer (TTET) from a sensitizer. These two triplet acceptors then interact and undergo

TTA, resulting in one ground-state acceptor and one singlet excited state acceptor. The singlet excited state relaxes to the ground state through fluorescence of a photon higher in energy that the initially absorbed photon.[11]

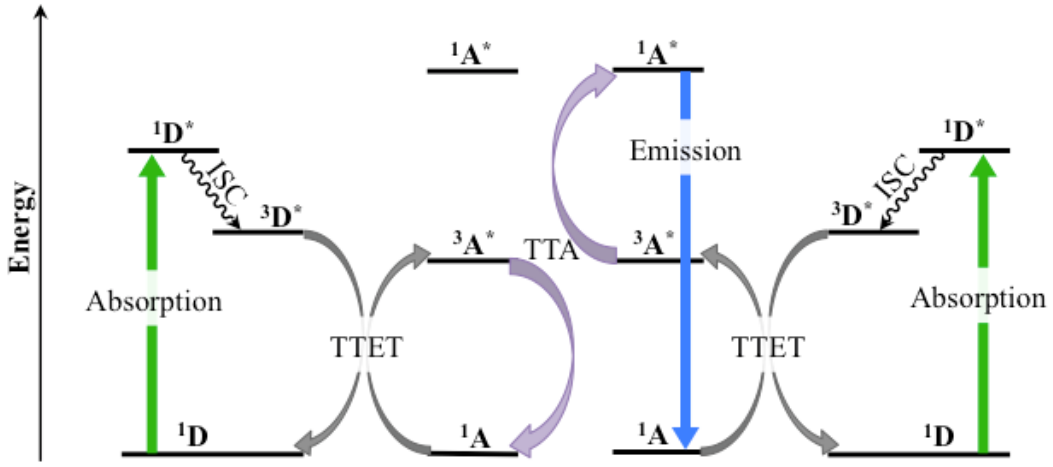

Figure 1.2.2. Schematic diagram of sensitized triplet-triplet annihilation and photon upconversion.

There are several factors that should be considered in choosing a sensitizer/acceptor pair to achieve efficient TTA-UC. First, the sensitizers should display strong visible-to-near-IR light absorption and a relatively long triplet excited state lifetime for effective diffusional energy transfer. Sensitizers that contain heavy metal atoms, such as Ru(II) and Ir(III) metal-to-ligand charge transfer complexes or Pt- and Pd-metalloporphyrins, with low energy π-π* transitions, are commonly employed as sensitizers in TTA-UC schemes due to their enhanced spin-orbit coupling, resulting in intersystem crossing efficiencies (Φ_{ISC}) near unity.[12] The overall upconversion quantum efficiency is also directly proportional to the fluorescence quantum yield (Φ_f) of the acceptor, thus π-conjugated aromatic organic chromophores are often used as acceptors/annihilators in these systems. Furthermore, the energy of the triplet state of the acceptor must lie below that of the sensitizer and a large energy difference facilitates a greater driving force for triplet-triplet energy transfer. Finally, the singlet excited state of the sensitizer should lie below

that of the acceptor, so that the sensitizer's singlet and triplet excited states are "nested" between those of the acceptor.[11]

Bimolecular TTA-UC was first reported by Castellano et al. in a solution of $[Ru(dmb)_3]^{2+}$ (dmb = 4,4′-dimethyl-2,2′-bipyridine) and anthracene.[13] The triplet MLCT excited state of $[Ru(dmb)_3]^{2+}$ is higher in energy than that of anthracene, and is quenched by TTET to anthracene. When anthracene was replaced with 9,10-diphenyl anthracene (9,10-DPA) improved upconversion efficiency was observed owing to the higher fluorescence quantum yield of 9,10-DPA (0.95, λ_{em} = 400 nm) relative to anthracene (0.27, λ_{em} = 440 nm).[13] Upconversion yields were further enhanced when $[Ru(dmb)_3]^{2+}$ (λ_{ex} = 514 nm) was exchanged for palladium(II) octaethylporphyrin (PdOEP, λ_{ex} = 544 nm), which has a higher Φ_{ISC} due to stronger spin orbit coupling of the Pd compound.[13] Moreover, near-IR-to-red upconversion was achieved by replacing PdOEP with palladium *meso*-tetraphenylltetrabenzoporphyrin ($PdPh_4TBP$, λ_{ex} = 635 nm) in conjunction with the acceptor, perylene (λ_{em} = 475 nm).[15]

For practical applications, translation from solution-based systems to the sold-state is necessary. To date, the most common approach to solid-state TTA-UC materials involves suspension of the chromophores in soft rubbery materials or rigid polymer matrices. In fact, a quantum efficiency of 22% for green-to-blue upconversion was realized in a rubbery ethyleneoxide/epichlorohydrin copolymer matrix under continuous wave laser excitation at relatively low power density (200 mW/cm^2).[16] However, chromophore distances and orientations cannot be controlled in these systems and as a result, upconversion efficiencies are reduced by aggregation and self-quenching. More recently, solid-state TTA-UC has been demonstrated in anthracene based metal-organic frameworks (MOFs) and layered porphyrin and anthracene-based surface-anchored MOFs (SURMOFs), which are discussed in more detail in subsection 1.3.3.

The upconversion quantum yield (Φ_{UC}) is determined by equation,

$$\Phi_{UC} = \Phi_{ISC} \times \Phi_{ET} \times \Phi_{TTA} \times \Phi_f \quad (1.2.5)$$

Where Φ_{ISC} is the quantum yield of intersystem crossing for the sensitizer, Φ_{ET} product of the quantum efficiencies of sensitizer-to-acceptor triplet energy transfer, Φ_{TTA} is the yield of triplet-triplet annihilation, and Φ_f is the yield of fluorescence of the acceptor.

The Φ_{TTA} can be calculated using equation 1.2.6.[17]

$$\Phi_{TTA} = \frac{2F_d E_p \lambda_d}{F_p E_d \lambda_p} \quad (1.2.6)$$

Here, F_p and F_d are the prompted and delayed fluorescence intensities, E_p and E_d are the laser pulse energies and λ_p and λ_d are the wavelengths of the prompted and delayed fluorescence. The factor of two is included to scale the maximum possible yield to unity, since each upconverted photon produced requires absorption of two incident photons.[17] The Φ_{UC} of a system is dependent upon a number of factors including chromophore concentrations and excitation power. Φ_{UC} can be determined experimentally by comparison with a standard using the equation 1.2.7.[18]

$$\Phi_{UC} = 2\Phi_{std}\left(\frac{A_{std}}{A_{UC}}\right)\left(\frac{I_{UC}}{I_{std}}\right)\left(\frac{\eta_{UC}}{\eta_{std}}\right)^2 \quad (1.2.7)$$

where Φ, A, I and η denote the fluorescence quantum yield, absorbance, integrated photoluminescence intensity and refractive index of the sample (UC) and the standard (std). The factor of two accounts for the two-to-one photon processes of TTA.[18]

Photon upconversion through TTA displays a quadratic dependence upon incident light power at low excitation intensities and a linear dependence at very high intensities. This phenomenon is consequence of two different factors that limit the decay kinetic of the triplet-excited state acceptor ($^3A^*$) population in each regime.[17,19] The [$^3A^*$] population decay includes a second-order

component from triplet-triplet annihilation (k_{TT}) and a first-order component from both unimolecular decay and pseudo-first-order processes (k_T), and can be described by equation 1.2.8, with the analytical solution presented in equation 1.2.9.[19]

$$\frac{d[^3A^*]_t}{dt} = -k_T[^3A^*]_t - k_{TT}[^3A^*]_t^2 \tag{1.2.8}$$

$$[^3A^*]_t = [^3A^*]_t - \frac{1-\beta}{e^{k_T t} - \beta} \tag{1.2.9}$$

The dimensionless parameter β represents the fraction of initial decay that occurs through the second-order channel, equation 1.2.10.[19]

$$\beta = \frac{k_{TT}[^3A^*]_0}{k_T + k_{TT}[^3A^*]_0} \tag{1.2.10}$$

The upconverted emission intensity (I_F) is proportional to $[^3A^*]$ and can be integrated with respect to time to give N_F (1.2.11).[19]

$$\mathrm{N_F} = \int_0^\infty \mathrm{I_F}(t)dt = \int_0^\infty \Phi_F k_{TT}[^3A^*]_t^2 \tag{1.2.11}$$

In the weak annihilation limit, $k_T > k_{TT}[^3A^*]$ and equation 1.2.7 becomes $[^3A^*]_t = [^3A^*]_0\exp(-k_T t)$. Hence, the emission intensity in this regime, $N_{F,weak}$, is proportional to $[^3A^*]^2$ and quadratic with respect to the incident power (equation 1.2.12).[19]

$$N_{F,weak} = \frac{\Phi_F k_{TT}[^3A^*]_0^2}{2k_T} \tag{1.2.12}$$

In the strong annihilation limit, $k_{TT}[^3A^*] > k_T$ and $[^3A^*]_t = [^3A^*]_0/(1 + k_{TT}[^3A^*]_0 t)$, which can be time-integrated (equation 1.2.13) to give $N_{F,strong}$, which is linearly proportional to $[^3A^*]$ and directly scales with incident power. Therefore, the highest possible upconversion efficiency for a given sample is achieved in this regime.[17, 19]

$$N_{F,strong} = \Phi_F k_{TT}[^3A^*]_0 \quad (1.2.13)$$

This linear intensity dependence is distinct from the intensity dependence of other UC processes such as two-photon absorption, second or higher harmonic generation, sequential multi-photon absorption and in rare-earth ion doped materials, where the upconversion signal shows a quadratic dependence upon the excitation intensity.[36] The excitation intensity at which the kinetic limit transitions from the weak to the strong annihilation regime is called the threshold intensity (I_{th}). I_{th} is established by the cross point of the extrapolated lines of the quadratic and linear dependencies.[20]

1.3. Excited-State Dynamics and Energy Transfer in MOFs

While the solid-state nature of MOFs can allow for the formation of energy bands, in most cases a molecular description is adequate for explaining their luminescence properties. Due to their heterogeneous nature and tunability, a wide-range of phenomena can give rise to luminescence in MOFs including linker-based emission, metal-based emission, ligand-to-metal charge transfer (LMCT) or metal-to-ligand charge transfer (MLCT). Luminescence may also arise from interactions between the MOF and guest species or between two interpenetrating frameworks.[1-2]

MOFs with ligand-based luminescence often demonstration energy transfer between ligands within the MOF assembly, between ligands and guest species, or at an interface between layers of two different MOFs. When designing MOFs with ligand-based luminescence, the difference between the emissive properties of the protonated and deprotonated species should be considered. Emission from the organic linker can also be affected by immobilization within the framework and result in an increase or decrease radiative decay processes. Furthermore, the metal ions of the nodes may impart heavy atom effects and result in an increased rate of ISC to the triplet state. Metal cations with closed shell electron configurations, such as d^0 or d^{10} transition metal cations, typically do not influence photophysics of the ligand.[21]

MOFs provide an excellent platform for studying energy transfer processes. Because of their defined structure and synthetic tunability, a wide-range of chromophores can be incorporated into MOFs. Furthermore, their crystalline nature allows for the distances and orientations of the chromophores within the framework to be determined by X-ray diffraction analysis. The following subsections will focus on resonance energy transfer and electron exchange processes in metalloporphyrin- and ruthenium-based MOFs and their applications in artificial photosynthesis and photon upconversion will be discussed.

1.3.1. Resonance Energy Transfer in Metalloporphyrin-based MOFs

The finite supply of fossil fuels and increasing global energy demands have compelled us to look for alternative, renewable energy sources. The sun provides the most abundant, cleanest source of renewable energy. In nature, plants use photosynthesis to capture energy from sunlight and convert carbon dioxide and water into carbohydrates, where the energy is stored as fuel. Similarly, artificial photosynthesis aims to utilize solar energy, water, and carbon dioxide to produce a chemical fuel. Natural photosynthetic systems employ, highly-ordered arrays of chromophores, such as metalloporphyrins, to harvesting light from the sun and funnel the energy to reaction centers.[22] Because of the highly ordered crystalline structure of MOFs, frameworks based on metalloporphyrin linkers have the potential to mimic these processes and for this reason, have been explored in light-harvesting and energy transfer schemes.[23-25]

Energy transfer in a metalloporphyrin-based MOF was first demonstrated by Hupp et al. in a pillared paddlewheel MOF, referred to as BOP MOF, which contained Zn(II) clusters as nodes a boron-dipyrromethene (bodipy)-based linker as the pillar and Zn(II) tetrakis(4-carboxyphenyl) porphyrin (ZnTCPP) as the paddlewheel linker. An isostructural MOF containing bodipy and a non-chromophoric paddlewheel linker, BOB MOF, was also synthesized as a control. When BOB

MOF was exposed to 543 nm light, the MOF displayed bodipy-based emission at 560 – 615 nm, while excitation of BOP MOF at 543 nm, resulted in ZnTCPP-based emission at 650 – 710 nm and no emission from bodipy was observed. Thus, the bodipy ligands can act as antenna chromophores and efficiently transfer energy to ZnTCPP ligands.[23]

To further understand energy migration in porphyrinic frameworks, two pillared paddlewheel, Zn-based MOFs were constructed from 1,2,4,5-tetrakis(4-carboxyphenyl)benzene (TCPB) pillars Zn(II) porphyrin struts, [5,15-dipyridyl-10,20-bis(pentafluorophenyl)porphinato]zinc-(II) (DA-ZnP) or [5,15-bis[4-(pyridyl)ethynyl]-10,20-diphenylporphinato]-zinc(II) (F-ZnP), referred to as DA-MOF and F-MOF, respectively (Figure 1.3.1 a).[24] DA-MOF and F-MOF were then doped with a ferrocene-based quencher (pyridyl-ferrocene, FcPy). Increased fluorescence quenching was observed with increasing FcPy concentration due to electron transfer from FcPy to the excited-state porphyrin. Theoretical calculations revealed that the exciton migration is directional, with estimated exciton migration distances of ~ 45 porphyrin units in DA-MOF but only ~3 in F-MOF. The enhanced efficiency of exciton migration in DA-MOF compared to F-MOF is attributed to the increased π-conjugation imposed by the additional acetylene moieties of DA-ZnP, which gives rise to stronger Q-band absorption and increased spectral overlap, as shown in Figure 1.3.1 b and c, resulting in enhanced dipole coupling and faster energy transfer between neighboring porphyrins.

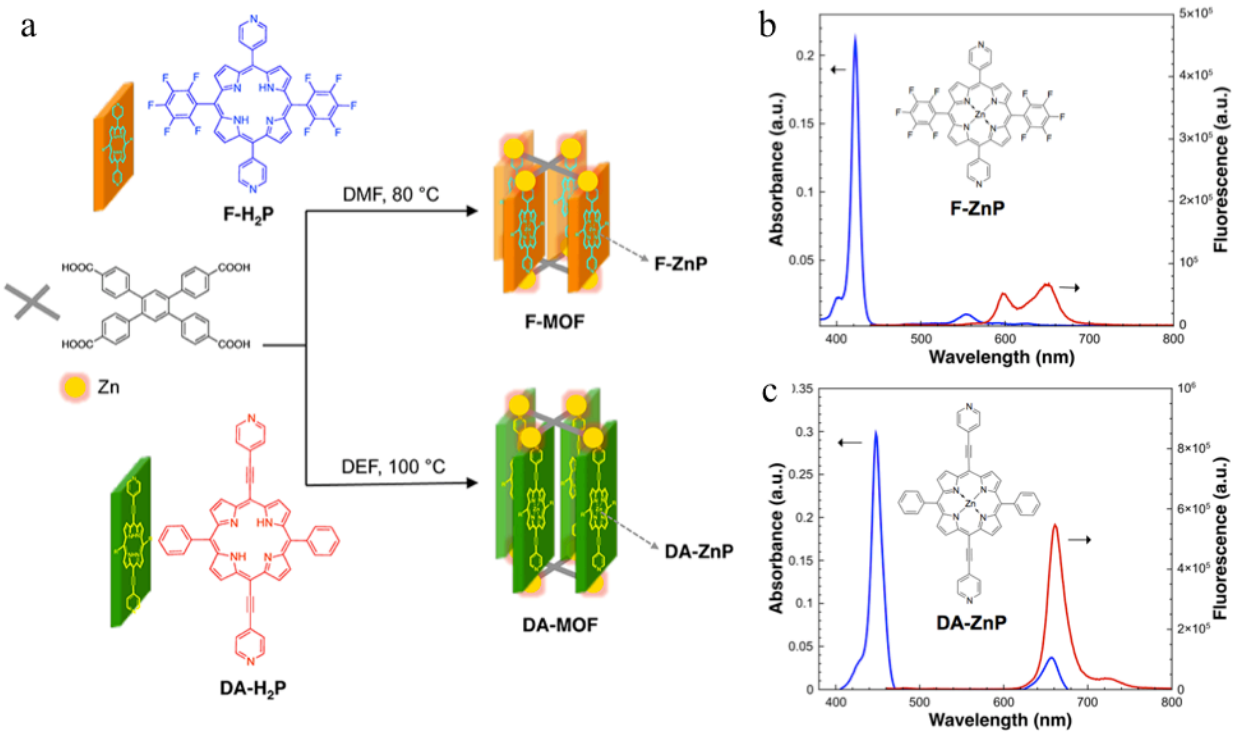

Figure 1.3.1. Schematic representation of synthetic routes for F-MOF and DA-MOF (a) absorption (blue) and emission (red) spectra of FZnP (b) and DA-ZnP (c) ligands in DMF and the corresponding chemical structures. Adapted with permission from ref. 24.

In another study, DA-MOFs were prepared as thin-films with a squarine dye attached to the surface of the film in order to probe energy migration to the surface (Figure 1.3.2 a).[24] The far-red absorption of the squarine dye exhibits efficient overlap with the DA-MOF emission spectrum. Following 450 nm excitation of the DA-MOF film with 450 nm, far-red emission from the squaraine dye was observed, and the porphyrin emission was fully quenched (Figure 1.3.2 b). These results reveal that efficient, long-range resonance energy transfer occurs through multiple porphyrin units (~ 50) to the surface-anchored dye.

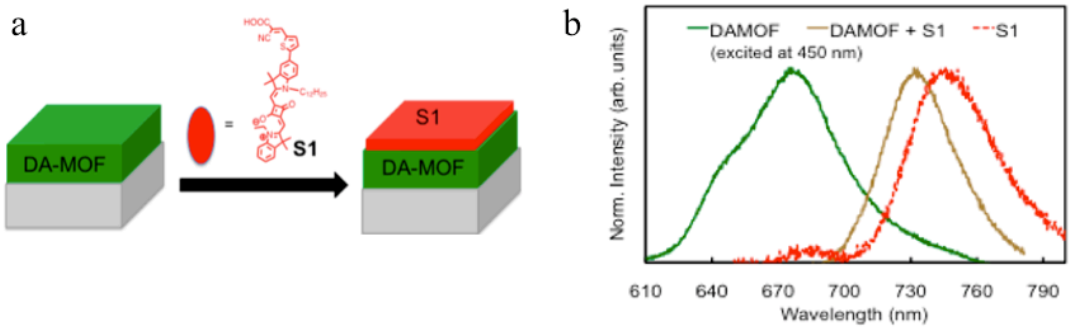

Figure 1.3.2. (a) Schematic diagram of DAMOF film (b) emission spectra of DA-MOF (green), S1 (red), and DA-MOF sensitized with S1 (brown) under 450 nm excitation. Adapted with permission from ref. 30.

1.3.2. Electron-Exchange Energy Transfer in MOFs Based on Ru or Os Complexes

Metal-to-ligand charge transfer (MLCT) excited-state dynamics of photoactive transition-metal complexes, such as $[Ru(bpy)_3]^{2+}$ and $[Os(bpy)_3]^{2+}$ (bpy = 2,2′-bipyridine), have been extensively studied.[26-28] These complexes absorb visible light to form a ^{1}MLCT excited state then efficiently undergo intersystem crossing to a ^{3}MLCT excited state. The long-lived ^{3}MLCT excited state returns to ground states by phosphorescence emission or may be deactivated through redox reactions or triplet-triplet energy transfer.[26] Due to their photophysical characteristics and long-lived ^{3}MLCT excited state redox activity, these complexes have been of particular interest for their applications in artificial photosynthetic systems, as well as a number of other fields.[28] MOFs provide an excellent platform for studying Ru to Os energy-transfer processes due to their crystalline nature, which allows the distances between metal centers to be determined. Kent et al. synthesized MOFs containing Ru(II) complexes with the chemical formula, $[L_{Ru}•Zn]•2DMF•4H_2O)$ where L_{Ru} = $\{Ru[4,4'-(HO_2C)_2\text{-bpy}]_2bpy\}^{2+}$ (Figure 1.3.3 a and b) as well as Os^{II}-doped, $[L_{Ru/Os}•Zn]•2DMF•4H_2O)$ frameworks.[29] Upon excitation, the pure Ru(II) MOF generated characteristic Ru(II) MLCT emission at 620 nm with a lifetime of 171 ns (Figure 1.3.3

c). As Figure 1.3.3 d demonstrates, the Ru emission lifetime decreased with increasing Os(II) doping concentration, indicative of enhanced Ru(II) excited-state quenching at higher Os(II) concentrations. Additionally, an increase in the Os(II) emission at 710 nm infers Ru-to-Ru excited-state energy migration and long-distance Ru-to-Os energy transfer. Subsequent theoretical analysis established that energy transfer occurs predominantly through a Dexter mechanism and that electronic coupling is slightly enhanced in the framework. Furthermore, the directionality of energy transfer can be controlled by tuning the MOF structure.[30]

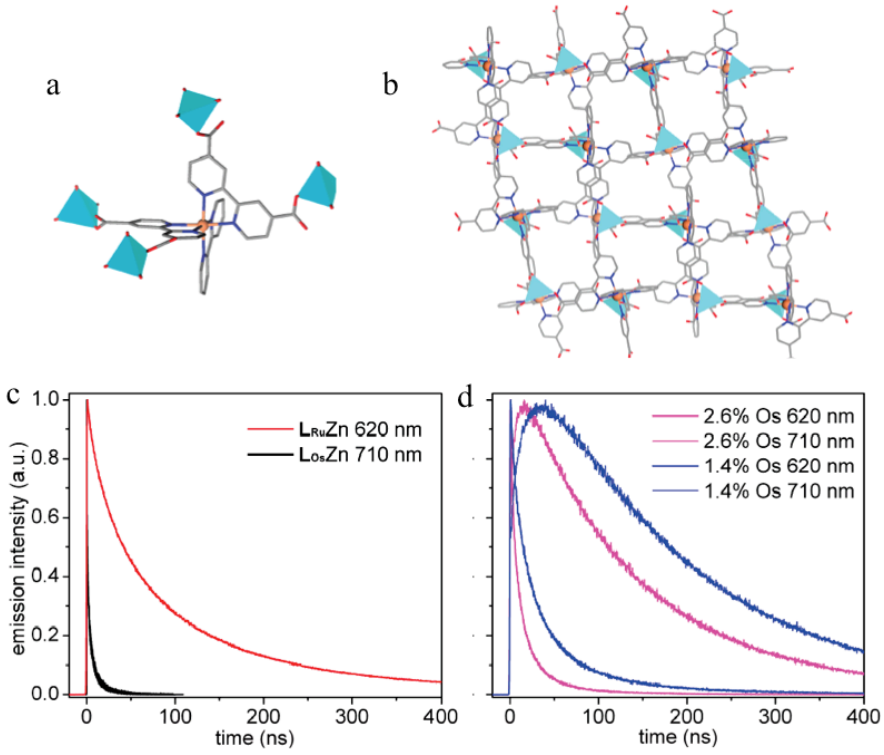

Figure 1.3.3. (a) Stick/polyhedra model of L_{Ru} and Zn centers in the $L_{Ru}Zn$ MOF. (b) Top view of the $L_{Ru}Zn$ MOF 2D bilayer structure along the a axis. (c) Transient emission decay profiles for $L_{Ru}Zn$ and $L_{Os}Zn$ MOFs at 620 and 710 nm, respectively, following two-photon excitation at 850 nm. (d) Transients for 1.4 and 2.6 mol % Os-doped $L_{Ru}Zn$ MOFs at 620 and 710 nm with emission at 620 nm dominated by Ru(II)* and at 710 nm by Os(II)*. Adapted with permission from ref. 29.

An understanding of the effects of chromophore incorporation into a MOF on the observed photophysics is essential for the rational design of such systems for a desired application. Lin and co-workers reported a method of doping the well-known, UiO-67 MOF, which has the formula $Zr_6O_4(OH)_4(bpdc)_6$ (bpdc = para-biphenyldicarboxylic acid) with a $[Ru(bpy)_3]^{2+}$ analogue (RuDCBPY-UiO-67). By replacing one bpy ligand with 2,2′-bipyridine-5,5′-dicarboxylic acid (dcbpy), the dcbpy ligand can replace bpdc and the complex may be incorporated into the backbone of the framework (RuDCBPY-UiO-67, Figure 1.3.4 b).[31] In order to further understand the effects of coordination into the MOF structure on the excited-state properties of the chromophore, Maza et al. probed the photophysics as a function of the RuDCBPY doping concentration (Figure 1.3.4 a).[32] At low doping concentrations, photophysics are similar to those observed for the complex inDMF solution, since the majority of the complex occupies the pores, filled with DMF. At higher concentrations, biphasic emission decays were observed, with a long lifetime component that decreased with increasing doping concentration and a concentration independent, short lifetime component. The former was ascribed to intermolecular energy transfer between neighboring chromophores in the backbone of the MOF (Figure 1.3.4 b), while the latter was attributed to emission from RuDCBPY complexes encapsulated in the pores (Figure 1.3.4 c). Based on the observed k_{RET} (1.6×10^5 s^{-1} at low doping concentrations to 5.4×10^6 s^{-1} at higher concentrations) and distance dependence ($1/r^4$), it was proposed that energy transfer occurs through an energy transfer mechanism that lies somewhere between weak and very weak dipole-dipole coupling regimes of dipole-dipole energy transfer.

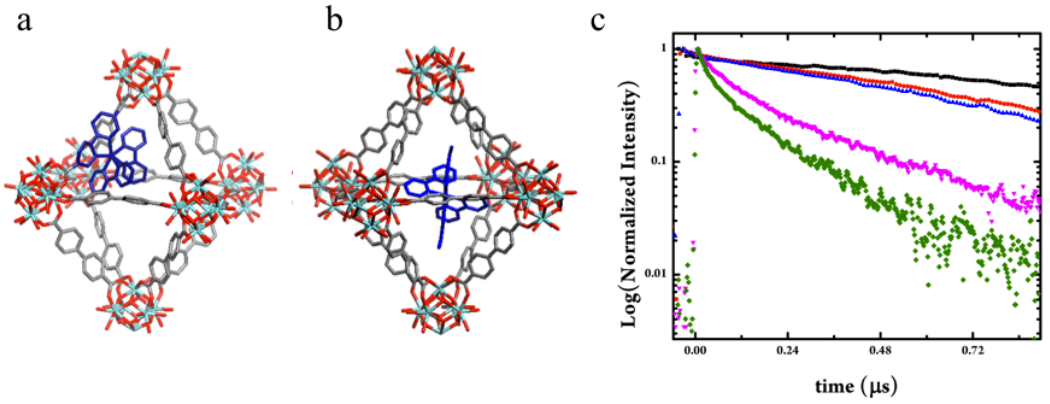

Figure 1.3.4. Representation of UiO-67 with $[Ru(bpy)_2(dcbpy)]^{2+}$ (a) incorporated into the framework and (b) encapsulated in an octahedral cavity. (c) Emission lifetime decays of RuDCBPY-UiO-67 at various RuDCBPY loadings: 3 m*m* (black), 7 m*m* (red), 16 m*m* (blue), 21 m*m* (pink), and 45 m*m* (green). Adapted with permission from ref. 22.

In a subsequent study, the dimensionality of energy transfer was shown to be dependent upon doping concentration.[33] The overall distribution of RuDCBPY in RuDCBPY-UiO-67 MOF crystallites was estimated using confocal fluorescence microscopy. At saturated concentrations, the chromophores are evenly distributed throughout the MOF, with metal-to-metal distances of ~ 21 Å. In this case, the ^{3}MLCT lifetime is believed to deactivate through three-dimensional Ru to Ru resonance energy transfer. On the other hand, at lower doping concentrations, the distances were found to be variable, with higher concentrations of complex located at the edges of the MOF crystal. In the latter case, quenching appears to be dominated by a two-dimensional resonance energy transfer mechanism.

1.3.3. TTA-based Photon Upconversion in MOFs

TTA-UC is a promising means of means of overcoming the thermodynamic efficiency limit of photovoltaic cells by harnessing sub-bandgap photons. While TTA-UC has predominantly been explored in solutions, integration into solar energy devices requires translation from solution-

based systems to solid-state TTA-UC materials. To this end, donor/acceptor chromophores have been suspended in rubbery polymer matrices (ie. polyurethane and polybutyl acrylate), however upconversion efficiencies were significantly reduced due to phase separation, aggregation, reabsorption, and back-transfer.[5-6] One approach to possibly avoid these drawbacks is immobilization of the sensitizer/acceptor chromophores into MOFs, which would enable control over their distances and relative spatial orientations.

TTA-UC in MOFs was first explored by Kimizuka et al.[34] Although this article has since been recalled due to irreproducibility of the solid-state upconversion emission at the low excitation intensity and reported triplet diffusion constants, the upconverted emission from MOF dispersions in benzene and PMMA have been reproduced. In this study, a series of zinc-based MOFs containing 4,4′-(anthracene-9,10-diyl)dibenzoate (adb) were with different molecular orientations were synthesized in order to investigate the structure-property relationship. The series of MOFs includes $[Zn_2(adb)_2bpy]_n$ (**1**, bpy = 4,4′-bipyridine), $[Zn_2(adb)_2dabco]_n$ (**2**, dabco = 1,4-diazabicyclo[2.2.2]octane) and $[Zn(adb)(DEF)_2]_n$ (**3**, DEF, *N,N*′-diethylformamide). The MOF structures were determined from single-crystal X-ray diffraction analysis (Figure 1.3.5). MOFs **1** and **2** form 2D, interpenetrating pillared structures while MOF **3** consists of 1D interpenetrating chains. The distances between anthracene planes in the MOFs are 5.0 Å and 7.6 Å for **1**, 4.8 Å for **2**, and 9.0 Å for **3**. Upon 365 nm excitation, the three MOFs display adb-based emission with a maximum around 440 nm. To probe UC, the MOF crystals were dispersed in deaerated solutions of the sensitizer, PtOEP and upconverted emission around 440 nm was observed from the three samples following irradiation with 532 nm light. The efficiency of TTET (Φ_{ET}) from the sensitizer to acceptor was estimated from the phosphorescence lifetimes of PtOEP in the absence (τ_0, ~ 85 μs) and presence (τ) of the MOF crystals. Using the equation $\Phi_{ET} = 1 - \tau/\tau_0$, the efficiencies of

MOFs 1, 2 and 3 were 12%, 8% and 59%, respectively. TTA-based mechanism was confirmed by measurements of the upconverted emission intensity as a function of excitation power. The threshold excitation intensities (I_{th}) were determined from UC emission intensity power dependency measurements and were found to be 2.4, 1.5 and 1.5 mW/cm^2 for MOFs **1**, **2** and **3**, respectively. The TTA-UC quantum yields (Φ_{UC}) were determined to be 0.43%, 0.34% and 4.3%, for MOFs **1**, **2** and **3**, respectively (Table 1.3.1).

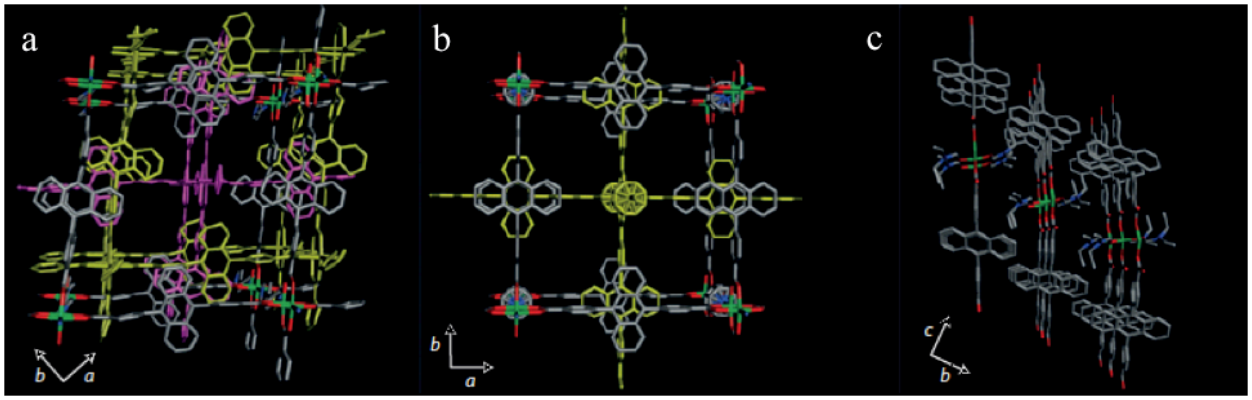

Figure 1.3.5. Crystal structures of (a) $[Zn_2(adb)_2bpy]_n$ (**1**), (b) $[Zn_2(adb)_2dabco]_n$ (**2**) and (c) $[Zn(adb)(DEF)_2]_n$ (**3**). Adapted with permission from ref. 34.

Table 1.3.1. Summary of TTA-UC data for **1**, **2** and **3**.[34]

	I_{th} (mW/cm^2)	Φ_{UC}
1	2.4	0.43 %
2	1.5	0.34 %
3	1.5	4.3 %

In another study, Howard and coworkers demonstrated triplet energy migration across heterojuctions of sensitizer-based to acceptor-based surface-anchored MOFs (SURMOFs) and subsequent upconverted fluorescence via TTA.[35] The SURMOF heterojunctions comprise a series of A–B–A heterostructures, where A is the acceptor/emitter layer, and B the sensitizer layer, both constructed from dicarboxylate-based ligands and Zn^{2+} nodes (Figure 1.3.6). Using layer-by-layer

techniques, the emitter layer, containing 4,4′-(anthracene-9,10-diyl)dibenzoate (ADB) organic linkers, was grown onto the surfaces of a Si substrate. The sensitizer layer, with Pd(II) 5,15-diphenyl-10,20-di(4-carboxyphenyl) porphyrin (Pd-DCP) linkers, was then deposited directly on top, followed by another emitter layer. Following excitation at 532 nm, upconverted emission from the ADB ligands of the emitter layer was observed. Therefore, the triplet-excited states diffuse across the B–A heterojunction via electron transfer to the emitter layer, where they decay through TTA-UC. The efficiency of triplet transfer from the sensitizer to emitter layer was found to be 58 ± 6 % and the overall Φ_{UC} was about 0.1 %. Possible factors limiting the quantum efficiency, in this system could be the quantum efficiency of singlet emission on the emitter, which was found to be 1.8%. A redshift was observed in the time-resolved emission of the emitter layer alone (i.e. in the absence of the sensitizer layer) after ~ 100 ps, which was attributed to aggregate formation. This aggregate formation inhibits TTA-UC processes occurs, resulting in the reduced quantum efficiency.

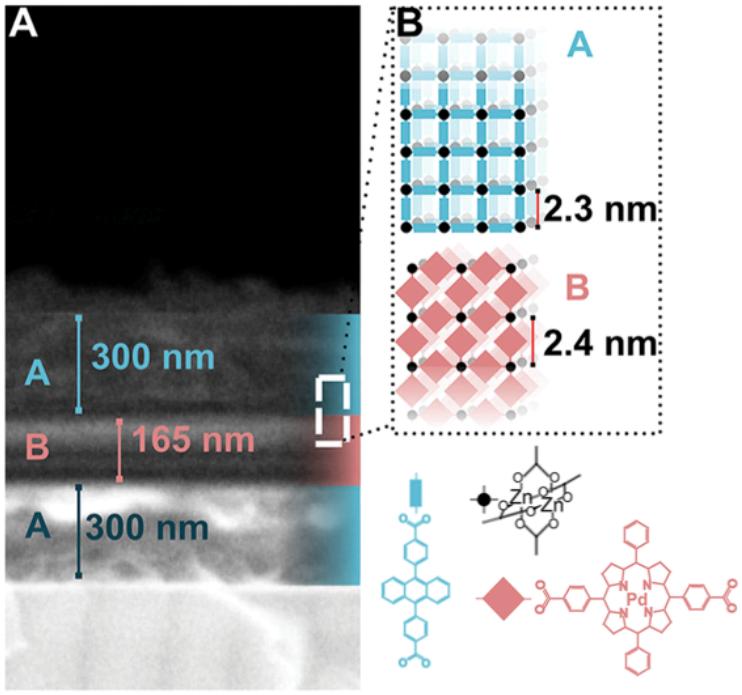

Figure 1.3.6. (a) SEM cross-section of a A–B–A SURMOF heterostructure on a Si substrate and (b) Schematic illustration of the heterostructure with the emitter layer, A, containing ADB represented in blue and the sensitizer layer, B, comprising Pd-DCP in red. Adapted with permission from reference 35.

1.4. Conclusions

The unique properties of MOFs afford a useful tool for systematic energy transfer studies, which can provide a more thorough understanding of structure-activity relationships to advance the design of efficient light-harvesting energy conversion materials. The modular nature of MOFs allows for incorporation of a wide array of chromophores and has led to the development of a variety of photoactive MOFs with wide-ranging applications. Long-distance, directional energy transfer has been demonstrated in MOFs containing metalloporphyrins and transition-metal complexes. Furthermore, MOFs have shown a proclivity to enhance energy-transfer processes. Energy transfer studies in the RUDCBPY MOFs revealed that the mechanisms of ET in MOFs are complex and dependent upon factors such as chromophore concentrations, distances and location

in the framework. MOFs have also proven to be viable platforms for designing TTA-UC materials and provide a versatile scaffold for modifying the three-dimensional orientation of chromophores. A deeper understanding of the factors that influence energy transfer dynamics in MOFs is necessary for the rational design of MOFs as highly-efficient light-harvesting and energy conversion materials.

1.5. Project Description

The work presented in this dissertation aims explore the structure-photophysical property relationships in MOFs to provide further insight into the factors governing energy-transfer processes in these materials. First, the effects of acceptor ligand spatial arrangement on TTA-UC efficiency is systematically investigated to determine how TTA-UC efficiencies can be enhanced in MOFs. To this end, three Zr-based MOFs were constructed from three different anthracene derivatives. In chapter 2, the effects of immobilization within the MOF on the photophysical properties of the ligands are examined. Chapter 3 discusses their propensity for photon upconversion. Secondly, in order to establish optimal distances for energy transfer in porphyrinic MOFs, the effects of porphyrin spacing on the rate of energy transfer is explored in Chapter 4. The spacing between porphyrin layers in a Zn-based pillared paddlewheel MOF was systematically tuned by variation of the pillar ligand. Fluorescence quenching studies were performed to determine the rates of energy transfer across this series.

1.6. References

1. Allendorf, M. D.; Bauer, C. A.; Bhakta, R. K.; Houk, R. J. T., Luminescent Metal-Organic Frameworks. *Chem. Soc. Rev.* **2009,** *38* (5), 1330.

2. Hu, Z.; Deibert, B. J.; Li, J., Luminescent Metal–Organic Frameworks for Chemical Sensing and Explosive Detection. *Chem. Soc. Rev.* **2014,** *43* (16), 5815-5840.

3. Zhou, H.-C.; Kitagawa, S., Metal–Organic Frameworks (MOFs). *Chem. Soc. Rev.* **2014,** *43* (16), 5415-5418.

4. Rowe, J. M.; Hay, J. M.; Maza, W. A.; Chapleski, R. C.; Soderstrom, E.; Troya, D.; Morris, A. J., Systematic Investigation of the Excited-State Properties of Anthracene-Dicarboxylic Acids. *J. Photochem. Photobiol. A* **2017,** *337*, 207-215.

5. Blankenship, R. E., Antenna Complexes and Energy Transfer Processes. In *Molecular Mechanisms of Photosynthesis*, Blackwell Science Ltd: Oxford, UK, 2002.

6. Valeur, B., *Molecular Fluorescence: Principles and Applications*. Wiley-VCH: Weinheim, Germany, 2001.

7. Lakowicz, J. R., *Principles of Fluorescence Spectroscopy*. Springer: New York, NY, 2006.

8. Ceroni, P.; Balzani, V., Photoinduced Energy and Electron Transfer Processes. In *The Exploration of Supramolecular Systems and Nanostructures by Photochemical Techniques. Lecture Notes in Chemistry*, Springer: Dordrecht, Netherlands, 2012; Vol. 78, pp 21-38.

9. Parker, C. A.; Hatchard, C. G., Sensitised Anti-Stokes Delayed Fluorescence. *Proc. Chem. Soc. Lond.* **1962**, 386-387.

10. Trupke, T.; Green, M. A.; Würfel, P., Improving Solar Cell Efficiencies by Up-Conversion of Sub-Band-Gap Light. *J. Appl. Phys.* **2002,** *92* (7), 4117-4122.

11. Singh-Rachford, T. N.; Castellano, F. N., Photon Upconversion Based on Sensitized Triplet–Triplet Annihilation. *Coord. Chem. Rev.* **2010,** *254* (21-22), 2560-2573.

12. Castellano, F. N.; McCusker, C. E., MLCT Sensitizers in Photochemical Upconversion: Past, Present, and Potential Future Directions. *Dalton Trans.* **2015,** *44* (41), 17906-17910.

13. Islangulov, R. R.; Kozlov, D. V.; Castellano, F. N., Low Power Upconversion Using MLCT Sensitizers. *Chem. Comm.* **2005,** (30).

14. Baluschev, S.; Yakutkin, V.; Miteva, T.; Wegner, G.; Roberts, T.; Nelles, G.; Yasuda, A.; Chernov, S.; Aleshchenkov, S.; Cheprakov, A., A General Approach for Non-Coherently Excited Annihilation Up-Conversion: Transforming the Solar-Spectrum. *New J. Phys.* **2008,** *10* (1).

15. Sasaki, Y.; Amemori, S.; Kouno, H.; Yanai, N.; Kimizuka, N., Near Infrared-to-Blue Photon Upconversion by Exploiting Direct S–T Absorption of a Molecular Sensitizer. *J. Mater. Chem. C.* **2017,** *5* (21), 5063-5067.

16. Kim, J.-H.; Deng, F.; Castellano, F. N.; Kim, J.-H., High Efficiency Low-Power Upconverting Soft Materials. *Chem. Mater.* **2012,** *24* (12), 2250-2252.

17. 16. Cheng, Y. Y.; Khoury, T.; Clady, R. G. C. R.; Tayebjee, M. J. Y.; Ekins-Daukes, N. J.; Crossley, M. J.; Schmidt, T. W., On the Efficiency Limit of Triplet–Triplet Annihilation for Photochemical Upconversion. *Phys. Chem. Chem. Phys.* **2010,** *12* (1), 66-71.

18. Crosby, G. A.; Demas, J. N., Measurement of Photoluminescence Quantum Yields. Review. *J. Phys. Chem.* **1971,** *75* (8), 991-1024.

19. Bachilo, S. M.; Weisman, R. B., Determination of Triplet Quantum Yields from Triplet−Triplet Annihilation Fluorescence. *J. Phys. Chem. A.* **2000,** *104* (33), 7711-7714.

20. 19. Monguzzi, A.; Mezyk, J.; Scotognella, F.; Tubino, R.; Meinardi, F., Upconversion-induced Fluorescence in Multicomponent Systems: Steady-state Excitation Power Threshold. *Phys. Rev. B.* **2008,** *78* (19).

21. Heine, J.; Müller-Buschbaum, K., Engineering Metal-based Luminescence in Coordination Polymers and Metal–Organic Frameworks. *Chem. Soc. Rev.* **2013,** *42* (24).

22. Mauzerall, D., Porphyrins, Chlorophyll, and Photosynthesis. In *Photosynthesis I*, 1977; pp 117-124.

23. Lee, C. Y.; Farha, O. K.; Hong, B. J.; Sarjeant, A. A.; Nguyen, S. T.; Hupp, J. T., Light-Harvesting Metal–Organic Frameworks (MOFs): Efficient Strut-to-Strut Energy Transfer in Bodipy and Porphyrin-Based MOFs. *J. Am Chem. Soc.* **2011,** *133* (40), 15858-15861.

24. So, M. C.; Jin, S.; Son, H.-J.; Wiederrecht, G. P.; Farha, O. K.; Hupp, J. T., Layer-by-Layer Fabrication of Oriented Porous Thin Films Based on Porphyrin-Containing Metal–Organic Frameworks. *J. Am Chem. Soc.* **2013,** *135* (42), 15698-15701.

25. Son, H.-J.; Jin, S.; Patwardhan, S.; Wezenberg, S. J.; Jeong, N. C.; So, M.; Wilmer, C. E.; Sarjeant, A. A.; Schatz, G. C.; Snurr, R. Q.; Farha, O. K.; Wiederrecht, G. P.; Hupp, J. T., Light-Harvesting and Ultrafast Energy Migration in Porphyrin-Based Metal–Organic Frameworks. *J. Am Chem. Soc.* **2013,** *135* (2), 862-869.

26. Roundhill, D. M., Photochemistry, Photophysics, and Photoredox Reactions of $Ru(bpy)_3^{2+}$ and Related Complexes. In *Photochemistry and Photophysics of Metal Complexes*, 1994; pp 165-215.

27. Kalyanasundaram, K., Photophysics, Photochemistry and Solar Energy Conversion with Tris(bipyridyl)ruthenium(II) and its Analogues. *Coord. Chem. Rev.* **1982,** *46*, 159-244.

28. Thompson, D. W.; Ito, A.; Meyer, T. J., [Ru(bpy)3]2+* and Other Remarkable Metal-to-Ligand Charge Transfer (MLCT) Excited States. *Pure Appl. Chem.* **2013,** *85* (7).

29. Kent, C. A.; Mehl, B. P.; Ma, L.; Papanikolas, J. M.; Meyer, T. J.; Lin, W., Energy Transfer Dynamics in Metal−Organic Frameworks. *J. Am Chem. Soc.* **2010,** *132* (37), 12767-12769.

30. Lin, J.; Hu, X.; Zhang, P.; Van Rynbach, A.; Beratan, D. N.; Kent, C. A.; Mehl, B. P.; Papanikolas, J. M.; Meyer, T. J.; Lin, W.; Skourtis, S. S.; Constantinou, M., Triplet Excitation Energy Dynamics in Metal–Organic Frameworks. *T J.Phys. Chem. C.* **2013,** *117* (43), 22250-22259.

31. Wang, C.; Xie, Z.; deKrafft, K. E.; Lin, W., Doping Metal–Organic Frameworks for Water Oxidation, Carbon Dioxide Reduction, and Organic Photocatalysis. *J. Am. Chem. Soc.* **2011,** *133* (34), 13445-13454.

32. Maza, W. A.; Morris, A. J., Photophysical Characterization of a Ruthenium(II) Tris(2,2′-bipyridine)-Doped Zirconium UiO-67 Metal–Organic Framework. *J.Phys. Chem. C.* **2014,** *118* (17), 8803-8817.

33. Maza, W. A.; Padilla, R.; Morris, A. J., Concentration Dependent Dimensionality of Resonance Energy Transfer in a Postsynthetically Doped Morphologically Homologous Analogue of UiO-67 MOF with a Ruthenium(II) Polypyridyl Complex. *J. Am Chem. Soc.* **2015,** *137* (25), 8161-8168.

34. Mahato, P.; Monguzzi, A.; Yanai, N.; Yamada, T.; Kimizuka, N., Fast and Long-Range Triplet Exciton Diffusion in Metal-Organic Frameworks for Photon Upconversion at Ultralow Excitation Power. *Nat. Mater.* **2015,** *14* (9), 924-930.

35. Oldenburg, M.; Turshatov, A.; Busko, D.; Wollgarten, S.; Adams, M.; Baroni, N.; Welle, A.; Redel, E.; Wöll, C.; Richards, B. S.; Howard, I. A., Photon Upconversion at Crystalline Organic-Organic Heterojunctions. *Adv. Mater.* **2016,** *28* (38), 8477-8482.

36. Miteva, T.; Roberts, A.; Nelles, G.; Yakutkin, V.; Baluschev, S. 44.5L: Late-News Paper: All-organic, Transparent Up-conversion Displays with Tailored Excitation and Emission Wavelengths. *SID 08 Digest*. **2008,** 665-668.

2. Synthesis, Characterization and Luminescent Properties of Two New Zr(IV) Metal-Organic Frameworks Based on Anthracene Derivatives

2.1. Introduction

In recent years, luminescent MOFs have been investigated for a variety of applications, including sensing of small molecules, light-emitting devices, photocatalysts as well as bioimaging and drug delivery.[1-2] Different components of a framework and interactions between them can give rise to the luminescent behavior, such as metal nodes (lanthanides), aromatic organic ligands, metal-to-ligand charge transfer (MLCT) interactions, ligand-to-metal charge transfer (LMCT) interactions or from guest species.[2,3] Ligand-based luminescence is particularly advantageous since the optical properties of the material may be fine-tuned via ligand functionalization or postsynthetic modifications.[4] Furthermore, the well-defined crystalline nature of MOF scaffolds affords an excellent platform for studying structure-function relationships.[5]

MOFs assembled from luminescent organic ligands often exhibit similar optical properties to the free ligand. However, these properties are altered to varying degrees due to coordination to the metal, π–π interactions, as well as MLCT or LMCT interactions.[2,6-7] In order to rationally design luminescent MOFs for specific applications, an in depth understanding of the excited-state properties of the ligand and the effect of incorporation into a MOF structure is necessary. Herein, two anthracene derivatives, 2,6-anthracenedicarboxylic acid (2,6-ADCA) and 1,4-anthracenedicarboxylic acid (1,4-ADCA), were used to construct the UiO-type Zr-based MOFs, 2,6-MOF and 1,4-MOF, respectively. We recently reported a detailed study of the photophysical properties of these ligands.[8] The addition of two carboxylic acid groups onto the aromatic ring system has a pronounced effect on the behavior of the parent anthracene moiety, which depends

on their location and protonation state. The excited state properties of the 2,6-MOF and 1,4-MOF were investigated and compared to those of the free ligand in solution.

2.2. Results

2.2.1. Synthesis and Characterization of 2,6- and 1,4-MOFs

Synthesis of the 2,6-MOF and 1,4-MOFs was adopted from previously reported methods for the UiO-66 framework with minor modifications.[9-11] Briefly, for the 2,6-MOF, 0.1 mmol $ZrCl_4$ and 0.1 mmol 2,6-ADCA were dissolved in 5 mL DMF along with 60 eq. formic acid as the modulator. The mixture was sonicated for 15 minutes followed by heating at 120 ºC for 24 hours. To synthesize the 1,4-MOF, 0.1 mmol $ZrCl_4$, and 0.1 mmol 1,4-ADCA and 80 eq. acetic acid were added to 3 mL DMF, the mixture was sonicated for 15 minutes and then heated at 100 ºC for 12 hours. The powder X-ray diffraction (PXRD) patterns of the 2,6-MOF and 1,4-MOF are shown in Figure 2.2.1 a and Figure 2.2.2 a, respectively. The diffraction data confirmed the formation of crystalline materials with a relatively large lattice spacing, as indicated by the presence of peaks below 10º 2θ, a telltale sign of framework structures. SEM images (Figure 2.2.1 b) revealed that the 2,6-ADCA MOF forms octahedral particles with an average size ~200 nm. On the other hand, the 1,4-ADCA MOF crystallized into rod-shaped particles, several microns in size (Figure 2.2.2 b). The internal surface area of the synthesized frameworks was assessed using N_2 sorption experiment at 77 K. Fitting the data to the BET model gave 711.49 m^2g^{-1} surface area with and a pore volume of 14.86 cm^3g^{-1} for 2,6-ADCA analogue (Figure 2.7.2 a). The 1,4-MOF on the other hand, exhibited a BET surface area of 378.09 m^2g^{-1}, and pore volume of 52.02 cm^3g^{-1} (Figure 2.7.2 b). Thermogravimetric analysis of the MOFs revealed that decomposition of the framework occurs at ~ 450 ºC for the 2,6-MOF (Figure 2.7.3 a) and ~ 500 ºC for the 1,4-MOF (Figure 2.7.3 b), as evidenced by a large weight drop due to the ligand

breakdown. The initial ~ 20% weight losses are attributed to the removal of solvent molecules from the pores of the MOF. The remaining percent weights (53% for 2,6-MOF and 26% for 1,4-MOF), correspond to ZrO_2 formed after the decomposition of the anthracene linkers.[12]

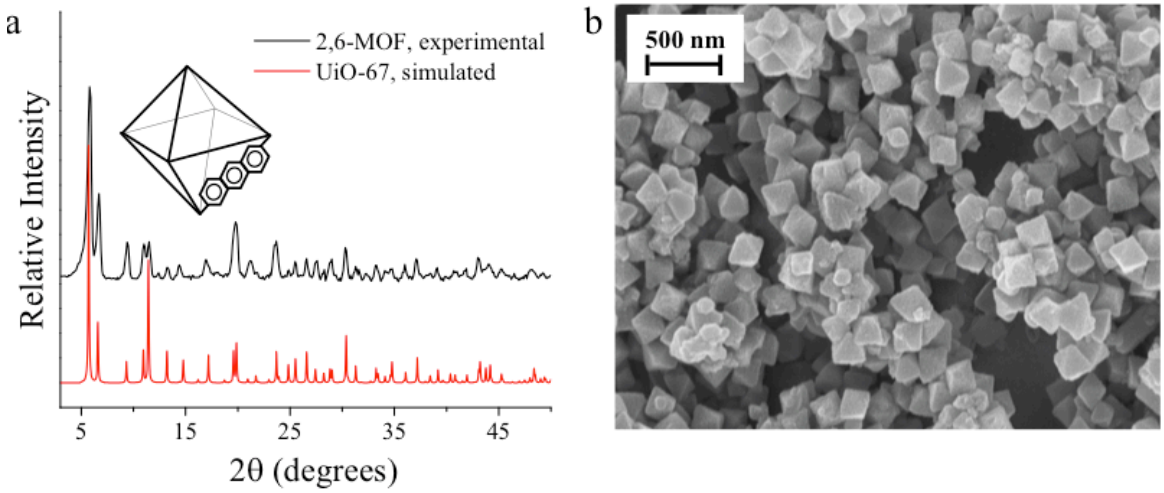

Figure 2.2.1. (a) PXRD patterns of the 2,6-MOF (black) compared to the simulated powder pattern of UiO-67 (red, from ref. 13) and (b) SEM image of 2,6-MOFs.

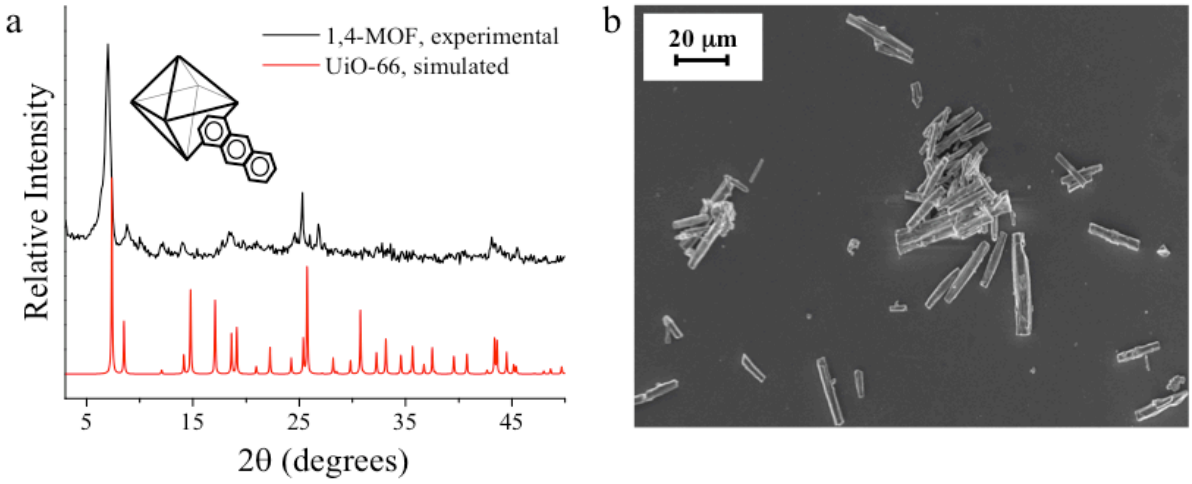

Figure 2.2.2. (a) PXRD patterns of 1,4-MOF (black) compared to the simulated powder pattern of UiO-66 (red, from ref. 14) and (b) SEM image of 1,4-MOFs.

2.2.2. Excited-State Properties

To examine how the ground and excited-state properties of the ligands are affected by coordination to Zr^{4+} in the MOF structure, the photophysics of these materials were compared to that of the protonated (ADCA) and deprotonated (ADC^{2-}) ligands in solution. The absorption and emission spectra of the ADCA-based MOFs are shown in Figure 2.2.3 (the respective excitation spectra are shown in Figure 2.7.4), along with that of the corresponding protonated (ADCA) and deprotonated (ADC^{2-}) ligands.

The absorption spectrum of the 2,6-MOF is significantly broadened compared to that of 2,6-ADCA and 2,6-ADC^{2-}, while the five sharp absorption bands, observed in the spectrum of 2,6-ADCA, are discernable in the framework spectrum. The 1,4-ADC Zr MOF displays a diffuse absorption spectrum, similar to that of 1,4-ADCA ligand. The absorption spectra of the 2,6-MOF and 1,4-MOFs are redshifted by 4 nm and 7 nm, respectively, relative to protonated ligands and 21 nm and 27 nm compared to the deprotonated forms.

The emission spectrum of the 2,6-MOF closely resembles that of the protonated, 2,6-ADCA ligand, with similar vibronically structured emission bands, and is only slightly blueshifted by ~ 2 nm relative to the free ligand. The 1,4-MOF displays a broad emission, with a maximum (λ_{max}) at ~ 465 nm, in between that of 1,4-ACDA (532 nm) and 1,4-ADC^{2-} (430 nm).

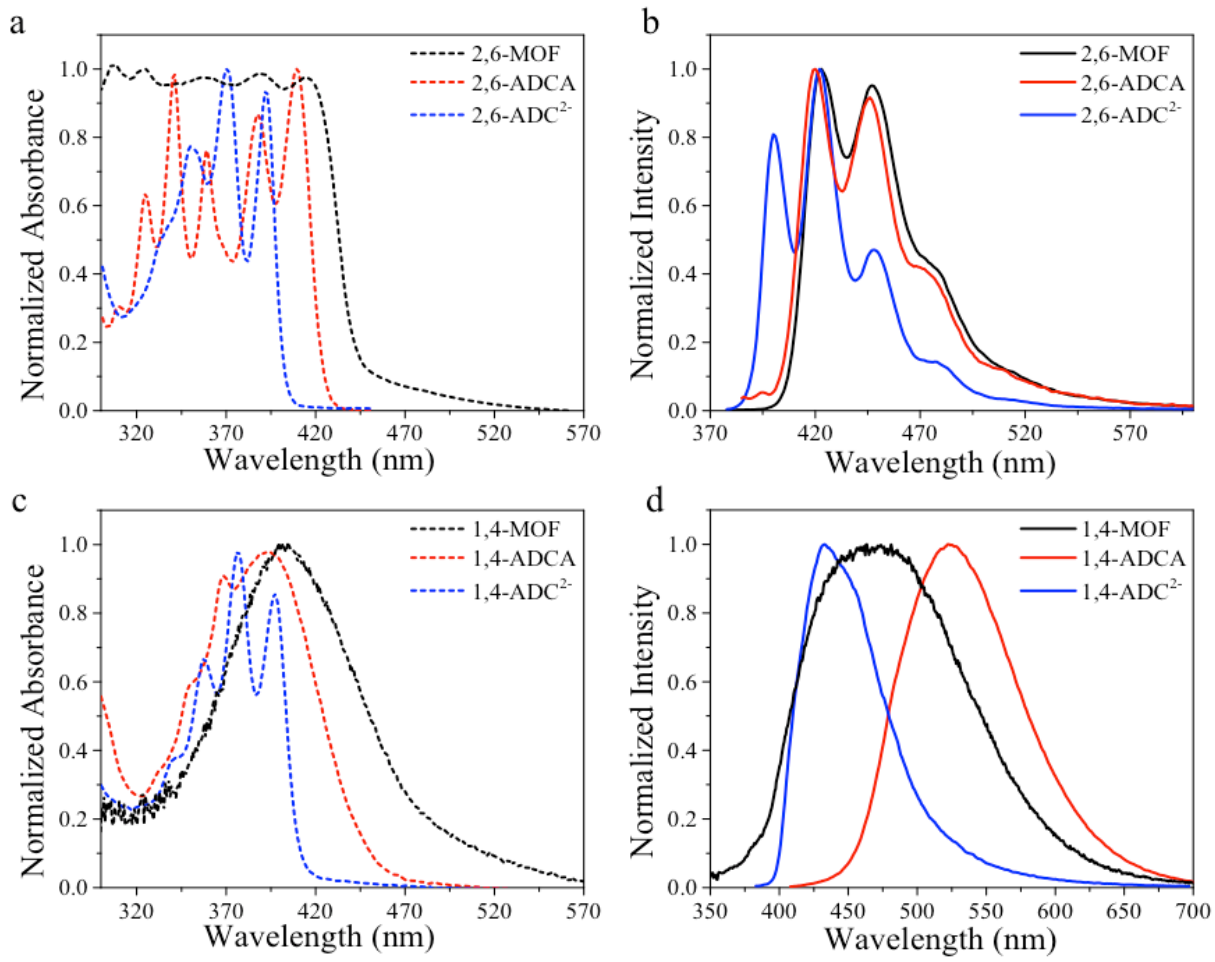

Figure 2.2.3. Absorption and emission spectra of 2,6-ADCA (A, B), 1,4-ADCA (C, D) in acidic DMF (ADCA, red), basic DMF (ADC^{2-}, blue) and incorporated into the MOF (black). λ_{ex} = 390 nm for 2,6-ADCA and 2,6-MOF, 370 nm for 2,6-ADC^{2-}, 400 nm for 1,4-ADCA and 1,4-MOF and 375 nm for 1,4-ADC^{2-}.

The 2,6-MOF exhibited a mono-exponential florescence decay, with a lifetime (τ_f) of 16.6 ± 1.1 ns (Figure 2.7.5–2.6.7 and Table 2.2.1) and quantum yield (Φ_f) of 0.87 ± 0.04 comparable to that observed for 2,6-ADCA in solution, and are ascribed to linker-based emission. The 1,4-MOF emission decay exhibits biexponential behavior; with different lifetime values obtained for the emission decay at in the higher (~400 – 450 nm) and lower (~500 – 550 nm) energy regions of the spectrum (Figure 2.2.4, Table 2.2.1). Global analysis of the emission decay yielded lifetime

components of τ_1 = 7.5 ± 0.1 ns and τ_2 = 19.9 ± 0.1 ns. The shorter lifetime component, τ_1, lies between that of 1,4-ADCA and 1,4-ADC^{2-}, while τ_2 is much longer than the lifetime of either the free 1,4-ADCA or 1,4-ADC^{2-} ligands in solution.

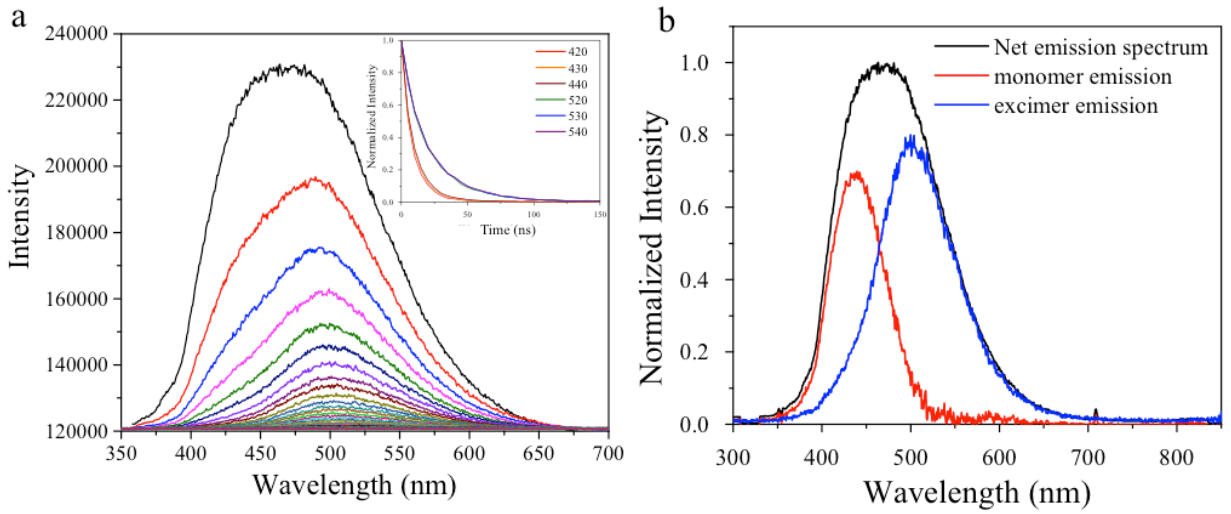

Figure 2.2.4. Time-resolved emission spectrum of 1,4-ADCA from 0 ns – 300 ns (a) and monomer (red) and excimer (blue) emission spectra obtained from global analysis of the net (black) emission spectrum (b).

Table 2.2.1. Summary of absorption and emission data, fluorescence lifetimes and quantum yields of the Zr-MOFs and anthracene-based linkers in solution and inside the frameworks.[8]

	$\lambda_{max,abs}$ (nm)	$\lambda_{max,em}$ (nm)	τ_1 (ns)	τ_2 (ns)	Φ_f
2,6-MOF	415	421	16.6 ± 1.1	–	0.87 ± 0.04
2,6-ADCA	410	423	15.2 ± 0.2	–	0.82 ± 0.08
2,6-ADC^{2-}	371	422	6.2 ± 0.05	–	0.11 ± 0.02
1,4-MOF	405	465	7.5 ± 0.1	19.9 ± 0.1	0.002 ± 0.0001
1,4-ADCA	393	550	12.5 ± 0.1	–	0.19 ± 0.04
1,4-ADC^{2-}	377	433	3.5 ± 0.1	–	0.07 ± 0.02

2.3. Discussion

2.3.1. Structural Characterization

The structures of the 2,6-MOF and 1,4-MOF were analyzed by comparing their powder patterns to the well-known UiO-67 and UiO-66 frameworks, respectively, because crystals large enough for single-crystal X-ray analysis could not be obtained.[13-14] The PXRD pattern of the 2,6-MOF is compared with that of UiO-67, in which the $[Zr_6(\mu_3\text{-}O)_4(\mu_3\text{-}OH)_4]^{12-}$ secondary building units (SBUs) are capped by 12 carboxylate groups from biphenyl-4,4′-dicarboxylate (BPDC) ligands resulting in an extended cubic structure. It is expected that functionalization of 2 and 6 positions around the anthracene ring system will results in a ligand with a similar length and shape as BPDC (a priori). The peaks observed in the powder pattern of the 2,6-MOF match well with the simulated PXRD patterns UiO-67. Le Bail refinement of the 2,6-MOF data (Figure 2.7.1) indicated a UiO-type structure with a unit cell parameter a = 26.97 Å, which correlates with the length of the 2,6-ADCA ligand. The SEM images show that the 2,6-MOFs form the quintessential octahedral-shaped crystals characteristic of UiO structures.

The binding nature for the 1,4-MOF would likely be similar to that of UiO-66, composed of 1,4-benzenedicarboxylate (BDC) ligands. The PXRD pattern obtained for the 1,4-MOF has distinct similarities to that of UiO-66, while not a direct match. The PXRD peaks appear broadened, which may indicate that some amorphous material is present. Furthermore, the SEM images show that the shape of the 1,4-MOF is that of large rod-shaped crystals not expected for UiO-66. While UiO-type octahedral-shaped crystals have been synthesized from 1,4-napthalene dicarboxylate ligands, the additional benzene ring of 1,4-ADCA may impose too much steric within the framework, giving rise to a large degree of defects within the crystal structure and the observed differences of the 1,4-MOF.[23] That said, rod-like structures are exhibited by Zr-MOFs including porphyrinic MOFs in the PCN series.[15] Repeated attempts to synthesize higher-quality crystals for advanced structural analysis were unsuccessful.

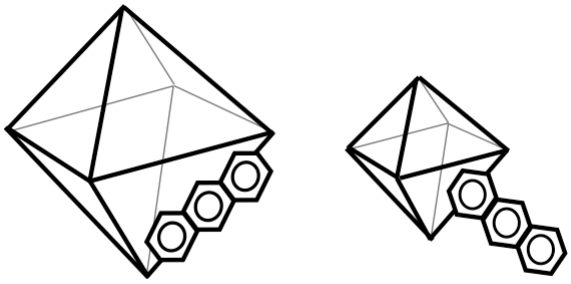

Figure 2.3.1. Cartoon representation of 2,6-MOF and possible 1,4-MOF structures.

2.4. Excited-State Properties

The vibronic structure observed in the absorption spectrum of 2,6-ADCA is attributed to the $^1A_1 \rightarrow {}^1L_b$ electronic transitions, polarized along the longitudinal axis of the anthracene plane. Functionalization of anthracene along this axis, at the 2 and 6 positions, with the electron-withdrawing carboxylic acid groups stabilized these transitions, resulting in the observed intense, vibronically structured $^1A_1 \rightarrow {}^1L_b$ bands.[6] The similar vibronic structure observed in the absorption spectrum of the 2,6-MOF indicates that the $^1A_1 \rightarrow {}^1L_b$ transitions remain stabilized upon coordination into the MOF. The emission spectrum of the 2,6-MOF closely resembles that of 2,6-ADCA in solution. Taken together, the similarity between the vibronic bands in the absorption and emission spectra of the framework and the free ligand reveal that incorporation of the 2,6-ADCA derivative into the MOF has negligible effects on the $^1A_1 \rightarrow {}^1L_a$ transition.

The fluorescence lifetime (τ_f) and quantum yield (Φ_f) of the 2,6-MOF ($\tau_f = 16.6 \pm 1.1$ ns, $\Phi_f = 0.87 \pm 0.04$) are very similar to that of 2,6-ADCA ($\tau_f = 15.2 \pm 0.2$ ns, $\Phi_f = 0.82 \pm 0.08$). τ_f and Φ_f are defined by equations 2.2.1 and 2.2.2, respectively, where k_r is the rate of radiative decay and k_{nr} is the rate of non-radiative decay.[21] The slight increase in both the fluorescence lifetime (τ_f) and quantum yield (Φ_f) could be attributed to steric restraint imposed on the chromophore by the

MOF scaffold, which reduces non-radiative decay pathways.[7,15,17] Slight differences in the crystal structure between batches of MOF powders synthesized may contribute to error in these values. The carboxylate functionalities were previously found to display slight resonance interactions with the anthracene unit of 2,6-ADCA and therefore, rotation of these units resulted in non-radiative energy disipation in the ligand.[8] The rotation of these functional groups that can occur in dilute solutions is largely supressed when they are bound to the Zr-oxo clusters.

$$\tau_f = \frac{1}{k_r + k_{nr}} \tag{2.2.1}$$

$$\Phi_f = \frac{k_r}{k_r + k_{nr}} \tag{2.2.2}$$

In contrast to the 2,6-MOF, 1,4-MOF exhibits substantial band broadening and a significant redshift in the observed absorption spectrum. This behavior is indicative of intermolecular interactions (π-π stacking) between the anthracene moieties.[17] The magnitude of the effect of π-interactions on the photophysical properties of anthracenes is sensitive to the distance between chromophores, as well as their relative orientation. Considering the short axis of anthracene (7.8 Å) and the size of potential MOF cages in Zr-MOFs, the long axis of 1,4-ADCA (11.8 Å) could potentially protrude into the pore and significantly interact with other anthracenes through a π overlap.[17,19] In the future, these ligands could be integrated into frameworks based on other metals to further vary their spatial separation with in the MOF.

The photoluminescence data for 1,4-MOF also indicate modulation of the photophysical properties upon MOF incorporation, potentially due to π–π interactions. The emission spectrum of 1,4-MOF is significantly broadened and does not resemble that of either protonated or deprotonated free linker (ADCA or ADC^{2-}). Furthermore, the biexponential lifetime behavior of the 1,4-MOF emission indicate the presence of two populations of chromophores. Considering the possibilities, the two populations could result from (1) encapsulated vs. incorporated anthracene

linkers,[18] (2) perfect vs. defected attachment of linkers within the framework, or (3) monomeric vs. excimer emission.

Global spectral fitting of the emission spectra enables the determination of the unique emission profiles for the two populations (Figure 2.2.4). The population exhibiting the shorter lifetime component (7.5 ± 0.1 ns) resembles the emission profile for 1,4-ADC^{2-}. The observed lifetime is slightly longer than that for 1,4-ADC^{2-}. We previously showed that the excited-state properties of 1,4-ADCA and 1,4-ADC^{2-} are significantly affected by both resonance interactions between the carboxylate groups and aromatic plane as well as free rotation of these functional groups.[8] Coordination of the ligand at the 1 and 4 positions imposes some steric hindrance that limits rotation of the carboxylates and decreases the associated vibrational relaxation pathways, giving rise to a longer fluorescence lifetime. Therefore, we assign the higher energy (shorter lifetime) population to that of monomeric linker emission.[24]

To assign the longer, lower-energy emissive population, the three potential situations enumerated above were considered. Due to the dramatically decreased quantum yield (Φ_f = 0.002 ± 0.0001), the third possibility, excimer formation, is most likely. An encapsulated population would be expected to behave similarly to the protonated free linker in solution. A defect population could resemble either protonated or deprotonated linker with similar lifetime and quantum yield. While the lifetime observed (19.9 ± 0.1 ns) could potentially be expected for a population resembling ADCA in a rigidified environment, the quantum yield suggests otherwise.[25] Excimer formation is known to result in both an increased lifetime and decreased quantum yield as observed here. Additionally, excimers exhibit redshifted emission spectra relative to monomeric emission. Considering the assignment of the shorter-lived component to monomeric linker emission, the same trend is observed here (435 nm vs. 503 nm). Additionally, excimer formation has previously

been observed in anthracene crystals and also resulted in ground-state and/or static quenching.[8,16] Given the preceding discussion, it is likely that 1,4-MOF forms an excimer between neighboring/adjacent anthracene units facilitated by π-π interactions. To further test this hypothesis, a different metal ion, such as zinc or aluminium, could be used to form the SBUs and provide a different arrangement of the chromophores within the crystal.[26-27]

2.5. Conclusions

The photophysics of the two anthracene derivatives, 2,6-ADCA and 1,4-ADCA, were shown to be altered upon coordination to the zirconium-based nodes in the two frameworks, 2,6-MOF and 1,4-MOF. The unique fluorescent properties of the ligands, as well as individual framework structure, resulted in distinctive luminescent behavior. The distances between anthracene units and their orientation within the framework dictate the extent of intermolecular interactions. In the 1,4-MOF, where the anthracene units are in the appropriate orientation and proximity to one another, there is efficient π-orbital overlap, giving rise to excimer formation. Whereas in the 2,6-MOF, the anthracene units are spatially separated, π– π interactions are considerably weaker, and as a result, and the emissive properties resemble that of the free linker in solution. The study provides an example of structure-dependence of MOF photophysical properties, which is facilitated by through-space interactions between chromophores. Furthermore, it was demonstrated that luminescent properties of a framework can be controlled by the functionalization of appropriate positions around the anthracene moiety.

2.6. Acknowledgements

This material is based upon work supported by the U.S. Department of Energy, Office of Science, Office of Basic Energy Sciences, under Award Number DE-SC0012446.

2.7. Supplemental Information

2.7.1. Experimental

2.7.1.1. Materials

2,6-anthracenedicarboxylic acid (2,6-ADCA) and 1,4-anthracenedicarboxylic acid (1,4-ADCA) were synthesized as previously described, and characterized by 1H NMR spectroscopy.[8] All other chemicals and solvents including, ZrCl4, N,N′-dimethylformamide (DMF, HPLC grade > 99%), acetic acid (reagent grade > 99%), and formic acid (reagent grade > 99%) were used as received without further purification from Alfa Aesar, Fisher Scientific, or Sigma-Aldrich.

2.7.1.2. Synthesis of 2,6-MOF

$ZrCl_4$ (23.3 mg, 0.1 mmol) and 2,6-ADCA (26.6 mg, 0.1 mmol) were added to a 2-dram vial along with DMF (5 mL) and formic acid (60 equivalents). The vial was capped and sealed with Teflon tape and the mixture was ultrasonicated for 15 minutes. The vial was then placed in an oven and heated at 120 ºC for 24 hours. The reaction solution was centrifuged immediately and the solvent was decanted off. The isolated solid was washed with DMF and centrifuged again until the solution was clear. The DMF was decanted off and the solid was dried under vacuum for 3 days.

2.7.1.3. Synthesis of 1,4-MOF

$ZrCl_4$ (23.3 mg, 0.1 mmol) and 1,4-ADCA (26.6 mg, 0.1 mmol) were added to a 2-dram vial along with DMF (3 mL) and acetic acid (80 equivalents). The vial was capped and sealed with Teflon tape and the mixture was ultrasonicated for 15 minutes. The vial was then placed in an oven and heated at 100 ºC for 12 hours. The reaction solution was centrifuged immediately and the

solvent was decanted off. The isolated solid was washed with DMF and centrifuged again until the solution was clear. The DMF was decanted off and the solid was dried under vacuum for 3 days.

2.7.1.4. Powder X-ray diffraction (PXRD)

PXRD patterns of MOF samples were obtained using a Rigaku Miniflex 600 with Cu(Kα) radiation (Cu−Kα = 1.5418 Å) in continuous scanning mode (10.0°/min) and a resolution of 0.1° 2θ. Le Bail refinement of the 2,6-MOF powder pattern was performed using Rietica for Windows v2.1 software.

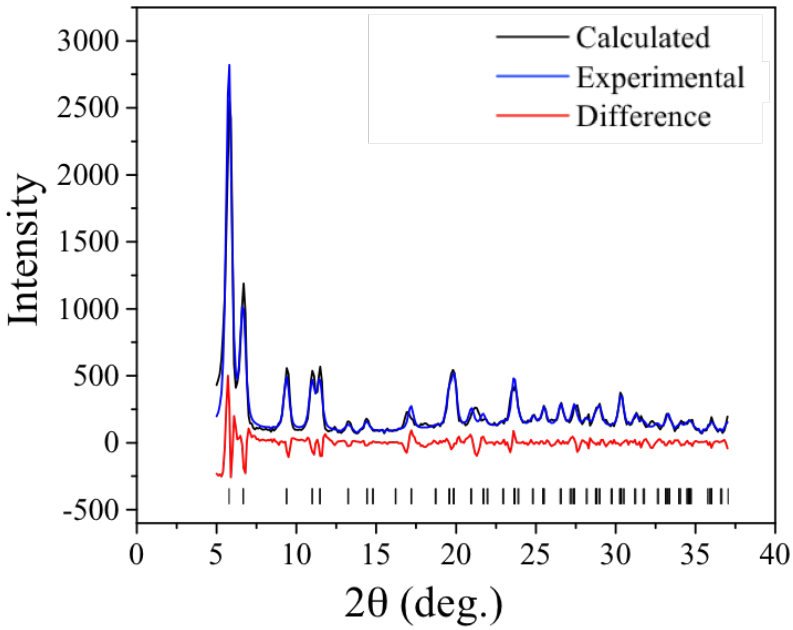

Figure 2.7.1. X-ray analysis of 2,6-MOF with the experimental PXRD pattern (blue), the calculated refined profile (black), and the difference (red).

2.7.1.5. Scanning electron microscopy (SEM)

SEM images were collected with a Leo/Zeiss 1550 Schottky field-emission scanning electron microscope equipped with an in-lens detector, operating at 5 kV.

2.7.1.6. Gas Sorption Isotherms

The N_2 sorption isotherm measurements were collected on a Quantachrome Autosorb-1 at 77 K. The samples were placed in a 6 mm large bulb sample cell, which was degassed under vacuum for 24 h at 120 °C. The surface areas of the materials were determined by fitting the adsorption data within the 0.05-0.3 P/P_0 pressure range to the BET and Langmuir equations.

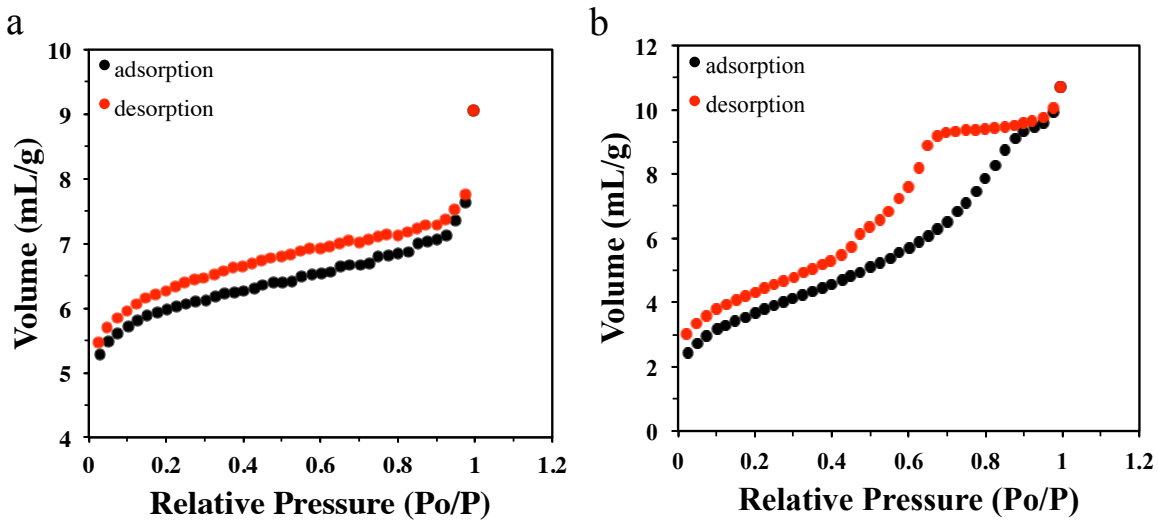

Figure 2.7.2. N_2 sorption isotherms of 2.6-MOF (a) and 1,4-MOF (b).

2.7.1.7. Thermogravimetric Analysis (TGA)

A Q-series TGA from TA instruments was used to analyze thermal stability of materials. 10 mg of sample in a high temperature platinum pan were heated under N_2 from 25 °C to 600 or 800 °C at a heating rate of 10 °C/min.

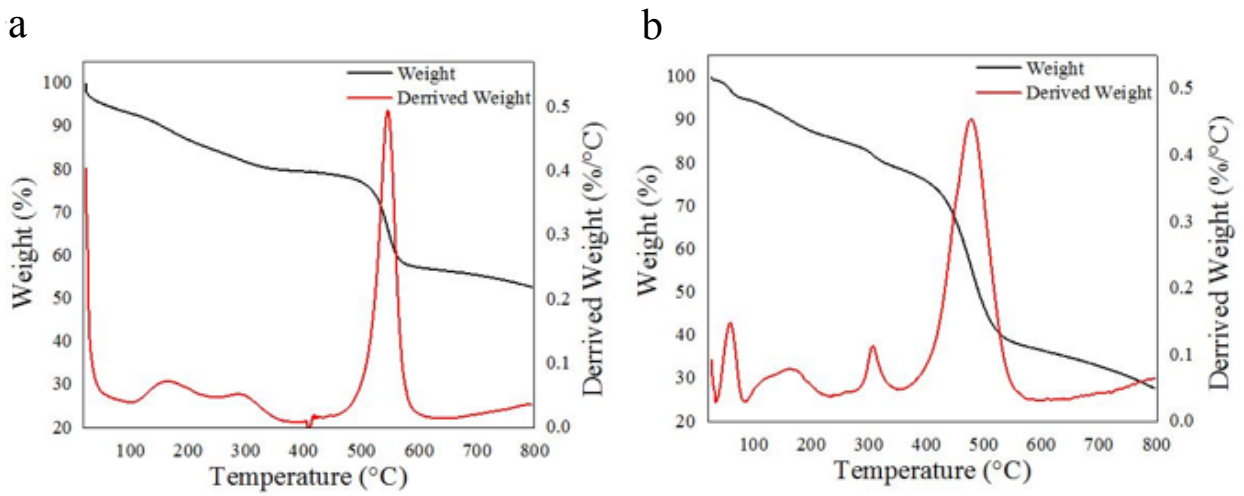

Figure 2.7.3. TGA profile of 2,6-MOF (a) and 1,4-MOF (b).

2.7.1.8. Steady-state Absorption Spectroscopy

The steady-state absorption spectra of the ligands were obtained using an Agilent Technologies 8453 UV-Vis diode array spectrophotometer (1 nm resolution) where the spectra were recorded with samples prepared in a 1 cm quartz cuvette. The same instrument was used to obtain diffuse reflectance spectra of MOF powders, where the sample compartment was replaced with an integration sphere. The powder samples were diluted by mixing with $BaSO_4$ (~ 90 %).

2.7.1.9. Steady-state Emission Spectroscopy and Time-Resolved Emission Lifetimes

Approximately 3 mg of MOF powder were suspended in 3 mL DMF and the sample was continuously stirred during the emission measurements. The ligand samples were prepared at concentrations of ~ 8 μM in DMF. The protonated (ADCA) and deprotonated (ADC^{2-}) ligand samples were prepared in aqueous solutions, using HCl or NaOH to achieve pH values of ~ 2 and 10.5, respectively. Quantum yields of fluorescence and steady-state emission spectra of the ADCA compounds were measured in DMF. The steady-state emission spectra were obtained using a

QuantaMaster Model QM-200-4E where the sample compartment was replaced with an integrating sphere (PTI). The excitation light source was a 75 W Xe arc lamp (Newport). The detector was a thermoelectrically cooled Hamamatsu 1527 photomultiplier tube (PMT). Kinetic traces were analyzed using Origin.

Time-resolved fluorescence lifetimes were obtained via the time-correlated single photon counting technique (TCSPC) with the same QuantaMaster Model QM-200-4E emission spectrophotometer from Photon Technology, Inc. (PTI) equipped with a 350 nm LED and a Becker & Hickl GmbH PMH-100 PMT detector with time resolution of < 220 ps FWHM. Florescence lifetime decays were deconvoluted from the time-dependent florescence signal and the instrument response function using the fluorescence decay analysis software, DecayFit, available online (Fluortools, www.fluortools.com, Figure 2.7.6–2.6.7).

To ensure stability of the MOF and the absence of free linker, the solutions were syringe filtered and emission was monitored at the maximum wavelength of emission for each ligand after the emission experiments were completed.

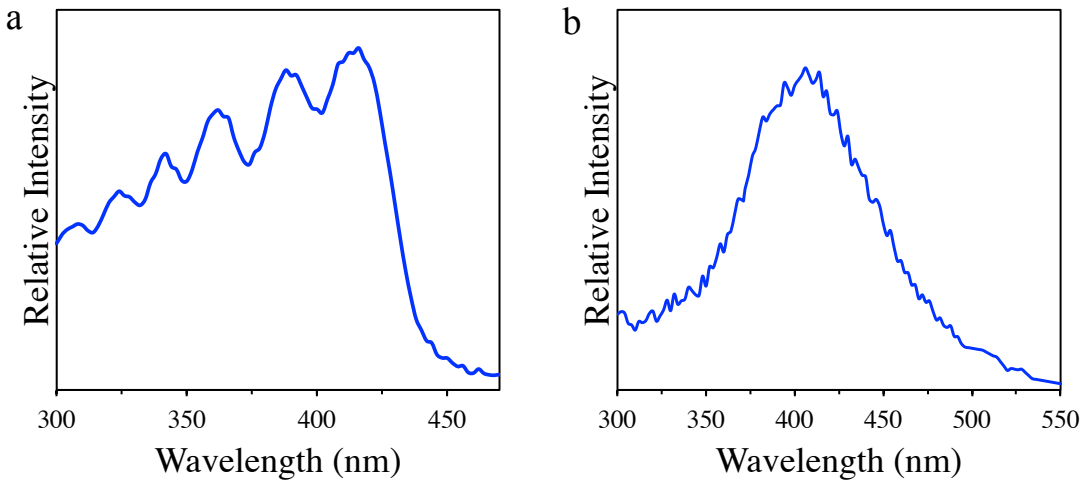

Figure 2.7.4. Excitation spectra of the 2,6-MOF, λ_{em} = 460 nm (a) and the 1,4-MOF, λ_{em} = 570 nm (b).

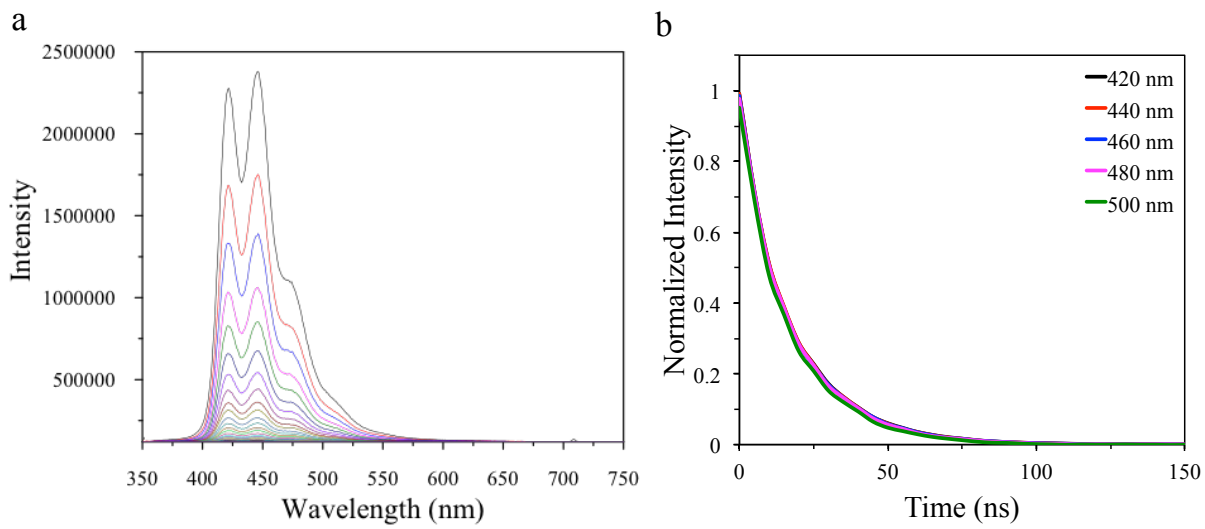

Figure 2.7.5. 2,6-MOF Time resolved emission decay spectra (a) of 2,6-MOF and decay curves (b) at selected wavelengths.

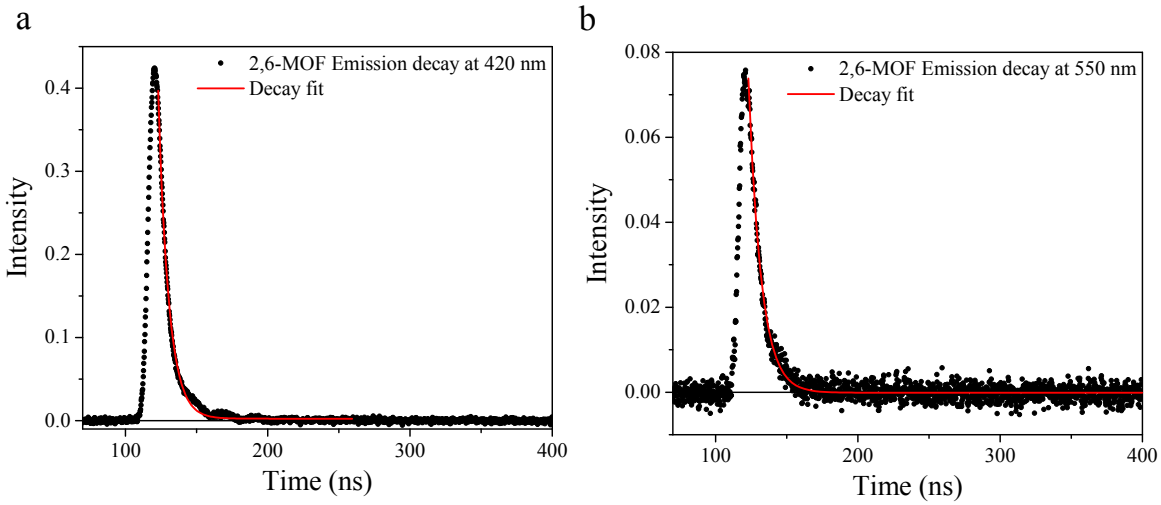

Figure 2.7.6. 2,6-MOF emission decay measured at 420 nm (a) and 550 nm (b) and respective mono-exponential fits (red line).

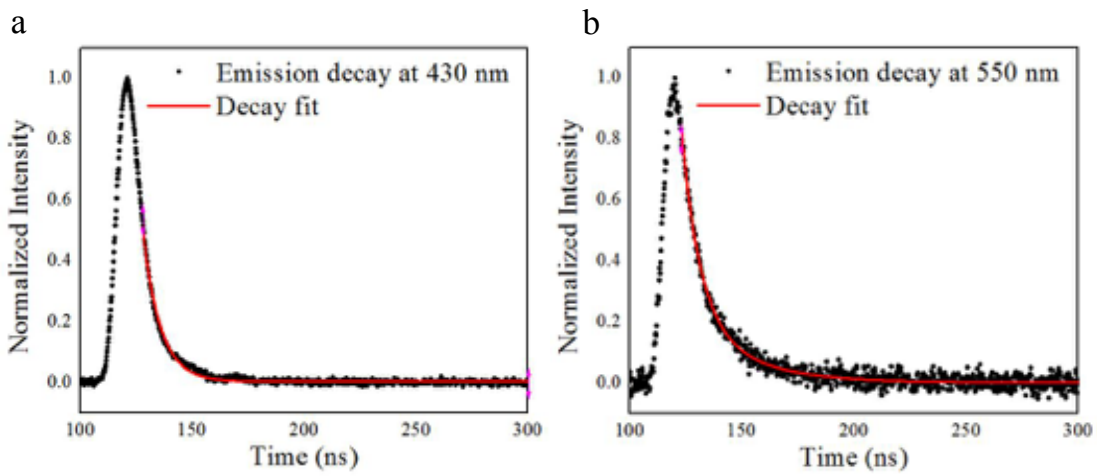

Figure 2.7.7. 1,4-MOF emission decay measured at 430 nm (a) and 550 nm (b) and respective mono-exponential fits (red line).

2.8. References

1. Hu, Z.; Deibert, B. J.; Li, J., Luminescent metal–organic frameworks for chemical sensing and explosive detection. *Chem. Soc. Rev.* **2014,** *43* (16), 5815-5840.

2. Allendorf, M. D.; Bauer, C. A.; Bhakta, R. K.; Houk, R. J. T., Luminescent Metal-Organic Frameworks. *Chem Soc Rev* **2009,** *38* (5), 1330.

3. Zhu, J.; Shaikh, S.; Mayhall, N.; Morris, A. J. Energy Transfer in Metal Organic Frameworks. 2018, Book chapter, *in press*.

4. Inokuma, Y.; Yoshioka, S.; Ariyoshi, J.; Arai, T.; Hitora, Y.; Takada, K.; Matsunaga, S.; Rissanen, K.; Fujita, M., X-ray Analysis on the Nanogram to Microgram Scale Using Porous Complexes. *Nature* **2013,** *495* (7442), 461-466.

5. Lu, W.; Wei, Z.; Gu, Z.-Y.; Liu, T.-F.; Park, J.; Park, J.; Tian, J.; Zhang, M.; Zhang, Q.; Gentle Iii, T.; Bosch, M.; Zhou, H.-C., Tuning the Structure and Function of Metal–Organic Frameworks Via Linker Design. *Chem. Soc. Rev.* **2014,** *43* (16), 5561-5593.

6. Meek, S. T.; Greathouse, J. A.; Allendorf, M. D., Metal-Organic Frameworks: A Rapidly Growing Class of Versatile Nanoporous Materials. *Adv. Mater.* **2011,** *23* (2), 249-267.

7. Perry IV, J. J.; Feng, P. L.; Meek, S. T.; Leong, K.; Doty, F. P.; Allendorf, M. D., Connecting Structure with Function in Metal–Organic Frameworks to Design Novel Photo- and Radioluminescent Materials. *J. Mater. Chem.* **2012,** *22* (20).

8. Rowe, J. M.; Hay, J. M.; Maza, W. A.; Chapleski, R. C.; Soderstrom, E.; Troya, D.; Morris, A. J., Systematic Investigation of the Excited-State Properties of Anthracene-Dicarboxylic Acids. *J. Photochem. Photobiol. A* **2017,** *337*, 207-215.

9. Katz, M. J.; Brown, Z. J.; Colón, Y. J.; Siu, P. W.; Scheidt, K. A.; Snurr, R. Q.; Hupp, J. T.; Farha, O. K., A Facile Synthesis of UiO-66, UiO-67 and Their Derivatives. *Chem. Comm.* **2013,** *49* (82).

10. Pu, S.; Xu, L.; Sun, L.; Du, H., Tuning the Optical Properties of the Zirconium-UiO-66 Metal-Organic Framework for Photocatalytic Degradation of Methyl Orange. *Inorg. Chem. Comm.* **2015,** *52*, 50–52.

11. Schaate, A.; Roy, P.; Godt, A.; Lippke, J.; Waltz, F.; Wiebcke, M.; Behrens, P., Modulated Synthesis of Zr-Based Metal-Organic Frameworks: From Nano to Single Crystals. *Chem. Euro. J.* **2011,** *17* (24), 6643-6651.

12. Tranchemontagne, D. J.; Hunt, J. R.; Yaghi, O. M., Room Temperature Synthesis of Metal-Organic Frameworks: MOF-5, MOF-74, MOF-177, MOF-199, and IRMOF-0. *Tetrahedron.* **2008,** *64* (36), 8553-8557.

13. Øien, S.; Wragg, D.; Reinsch, H.; Svelle, S.; Bordiga, S.; Lamberti, C.; Lillerud, K. P. Detailed Structure Analysis of Atomic Positions and Defects in Zirconium Metal–Organic Frameworks. *Cryst. Growth Des.*, **2014**, *14* (11), pp 5370–5372.

14. Valenzano, L.; Civalleri, B.; Chavan, S.; Bordiga, S.; Nilsen, M. H.; Jakobsen, S.; Lillerud, K. P.; Lamberti, C., Disclosing the Complex Structure of UiO-66 Metal Organic Framework: A Synergic Combination of Experiment and Theory. *Chem. Mater.* **2011,** *23* (7), 1700-1718.

15. Kelty, M. L.; Morris, W.; Gallagher, A. T.; Anderson, J. S.; Brown, K. A.; Mirkin, C. A.; Harris, T. D., High-Throughput Synthesis and Characterization of Nanocrystalline Porphyrinic Zirconium metal–Organic Frameworks. *Chem. Comm.* **2016,** *52* (50), 7854-7857.

16. Lakowicz, J. R. *Subcell. Biochem.* **1988,** *13*, 89-126.

17. Jas, G. S.; Wang, Y.; Pauls, S. W.; Johnson, C. K.; Kuczera, K., Influence of Temperature and Viscosity on Anthracene Rotational Diffusion in Organic Solvents: Molecular Dynamics Simulations and Fluorescence Anisotropy Study. *J. Chem. Phys.* **1997,** *107* (21), 8800-8812.

18. Maza, W. A.; Morris, A. J., Photophysical Characterization of a Ruthenium(II) Tris(2,2′-bipyridine)-Doped Zirconium UiO-67 Metal–Organic Framework. *J. Phys. Chem. C.* **2014,** *118* (17), 8803-8817.

19. Hong, D. H.; Suh, M. P., Enhancing CO2Separation Ability of a Metal-Organic Framework by Post-Synthetic Ligand Exchange with Flexible Aliphatic Carboxylates. *Chem. Euro. J* **2014,** *20* (2), 426-434..

20. de Melo, J. S. S.; Costa, T.; de Castro, C. S.; Maçanita, A. L., Photophysics of Fluorescently Labeled Oligomers and Polymers. In *Photochemistry*, **2013**, 59-126.

21. Valeur, B.; Berberan-Santos, M. N., *Molecular Fluorescence: Principles and Applications, Second Edition*. Wiley-VCH Verlag & Co. KGaA, Boschstr. : Weinheim, Germany, 2012, 61.

22. Sugino, M.; Araki, Y.; Hatanaka, K.; Hisaki, I.; Miyata, M.; Tohnai, N., Elucidation of Anthracene Arrangement for Excimer Emission at Ambient Conditions. *Cryst. Growth Des.* **2013,** *13* (11), 4986-4992.

23. Butova, V. V.; Budnyk, A. P.; Guda, A. A.; Lomachenko, K. A.; Bugaev, A. L.; Soldatov, A. V.; Chavan, S. M.; Øien-Ødegaard, S.; Olsbye, U. Lillerud, K. P.; Atzori, C.; Bordiga, S; Lamberti, C. Modulator Effect in UiO-66-NDC (1,4-Naphthalenedicarboxylic Acid) Synthesis and Comparison with UiO-67-NDC Isoreticular Metal− Organic Frameworks. *Cryst. Growth Des*. **2017,** *17*, 5422−5431.

24. Cui, Y.; Yue, Y.; Qian, G.; Chen, B. Luminescnent Functional Metal–Organic Frameworks. *Chem. Rev*. **2012,** *112* (2), 1126-1162.

25. Mataga, M.; Tomura, M.; Nishimura, H. Fluorescence Decay Times of Naphthalene and Naphthalene Excimers. *Mol. Phys*. **1965,** 367-375.

3. Sensitized photon upconversion in anthracene-based metal-organic frameworks

3.1. Introduction

Triplet-triplet annihilation-based upconversion (TTA-UC) is a process by which low energy photons are converted into higher energy photons.[1-3] Thus, TTA-UC has been proposed as a means of increasing solar cell efficiency by reducing sub-bandgap spectral losses. The mechanism of TTA-UC involves sensitizer chromophores, which absorb lower-energy light and undergo intersystem crossing to the triplet state. An acceptor chromophore is then promoted directly to the triplet state via a Dexter-type electron exchange mechanism from the sensitizer. Two triplet excited state acceptors can interact an undergo TTA, resulting in a singlet-state acceptor and fluorescence of higher-energy light. For many applications, including solar cell devices, solid-state upconversion systems are ideal. Solid-state upconversion systems typically involve suspension of the chromophores in soft-materials and glasses. However, this approach does not provide the ability to control molecular orientation and distance and as a result, these materials display greatly reduced upconversion efficiencies compared to solution-based systems.[4,5] That said, recent work by Hanson et al. introduced a strategy for spatial control using self-assembled bilayers in which the donor and sensitizer molecules are linked together through a Zn(II) ion.[6]

Metal-organic frameworks (MOFs) provide an excellent platform for solid-state molecular upconversion. Their high surface area, rigid crystalline structure and porous nature provide a robust means of controlling molecular orientation, which can enhance molecular coupling, resulting in improved photophysical energy-transfer processes. Additionally, the synthetic tunability of MOFs allows for the excitation and emission wavelengths to be altered by judicious choice of metal nodes and organic linkers. Furthermore, MOFs have demonstrated a proclivity for

efficient photo-driven energy migration and reactivity.[7-14] The Kimizuka group first reported TTA-UC in a zinc MOF containing 9,10-dipyridyl anthracene (DPA) based ligands MOF, although values of recorded efficiencies were later called into question.[15] Later, Howard et al. demonstrated triplet energy transfer across heterojunctions of zinc MOFs from a Pd(II)porphyrin–containing sensitizer layer to a DPA-based emitter layers, followed by UC from the emitter layers.[16] However, the optimal distances and orientations for TTA-UC systems have not been defined. In the current study, we explore TTA-UC in three Zr MOFs constructed from three anthracene dicarboxylate (ADC) derivatives, 9,10-ADC (9,10-MOF), 2,6-ADC (2,6-MOF) and 1,4-ADC (1,4-MOF) in order to develop design rules for molecular and spatial orientation in MOFs.

3.2. Results and Discussion

Anthracene and several of its derivatives have been utilized in TTA-UC systems in combination with a Pd porphyrin sensitizer.[17,18] We recently described the photophysical properties of the three anthracene dicarboxylic acid derivatives listed above in dilute solutions.[19] Functionalization of anthracene with the electron-withdrawing carboxylate groups alters the excited-state properties of the parent molecule to various degrees depending on the location on the ring system. Therefore, we first probed UC in DMF solutions of each ADCA ligand (6.0×10^{-4} M) and Pd(II) mesoporphyrin IX (PdMP, 4.0×10^{-6} M). Following 532 nm excitation, UC emission was observed from each anthracene derivative (Figure 3.4.6 –Figure 3.4.8). The lifetime of 9,10-ADCA increased from 4.2 ± 0.03 ns to 1.8 ± 0.1 μs, from 9.0 ± 0.9 ns to 2.3 ± 0.3 μs for 2,6-ADCA, and from 9.6 ± 0.1 ns to 1.6 ± 0.2 μs for 1,4-ADCA.[18] This substantial increase in the emission lifetimes is indicative of energy transfer (ET) from the long-lived triplet excited state of PdMP. As a consequence of this Dexter-type ET process, the emission lifetime of the sensitizer is considerably quenched. The quantum efficiency of energy transfer from the sensitizer to the

acceptor (Φ_{ET}) was estimated from the lifetimes of the sensitizer measured in the presence (τ) and absence (τ_0 = 19.5 ± 0.8 μs) of the acceptor (Figure 3.4.9–Figure 3.4.12). Using the equation 1 – τ/τ_0, Φ_{ET} was found to be ~ 87 %, 91 % and 84 % for the 9,10-ADCA, 2,6-ADCA and 1,4-ADCA samples, respectively. The quantum yield of UC (Φ_{UC}, equation 3.2.1) is given by the product of the quantum yield of intersystem crossing for the sensitizer (Φ_{ISC}), Φ_{ET}, the yield of TTA (Φ_{TTA}) and acceptor florescence quantum yield (Φ_f).

$$\Phi_{UC} = \Phi_{ISC} \times \Phi_{ET} \times \Phi_{TTA} \times \Phi_f \quad (3.2.1)$$

The UC quantum yields were determined experimentally using equation 3.2.2.[20]

$$\Phi_{UC} = 2\Phi_{std}\left(\frac{A_{std}}{A_{UC}}\right)\left(\frac{F_{UC}}{F_{std}}\right)\left(\frac{I_{std}}{I_{UC}}\right)\left(\frac{\eta_{UC}}{\eta_{std}}\right)^2 \quad (3.2.2)$$

Here, A is the absorbance at the excitation wavelength, F is the integrated emission spectrum, I is the excitation intensity and η is the refractive index of the solvent.[2] The factor of 2 is added to adjust for the fact that two photons must be absorbed to generate one emitted photon. For 9,10-ADCA, 2,6-ADCA and 1,4-ADCA, Φ_{UC} was 1.8 %, 2.7 % and 1.3 %, respectively.

The three anthracene-containing ligands were incorporated into Zr-based MOFs and their propensity for photon UC was explored. We previously described the synthesis and photophysics of the 2,6-MOF and 1,4-MOF.[21] The 9,10-MOF was synthesized following a reported procedure.[22] The powder X-ray diffraction (PXRD) pattern of the 9,10-MOF (Figure 3.2.1 a) confirmed the formation of a crystalline material. As shown in the SEM images (Figure 3.2.1 b), the 9,10-MOF forms octahedral crystals ~ 1 μm in size. BET and TGA analysis are provided in the Supplemental Information. Although 9,10-MOF and UiO-66 are isostructural,[22] it is important to elucidate the MOF structure in order to determine the orientation, angle and distance between chromophores.

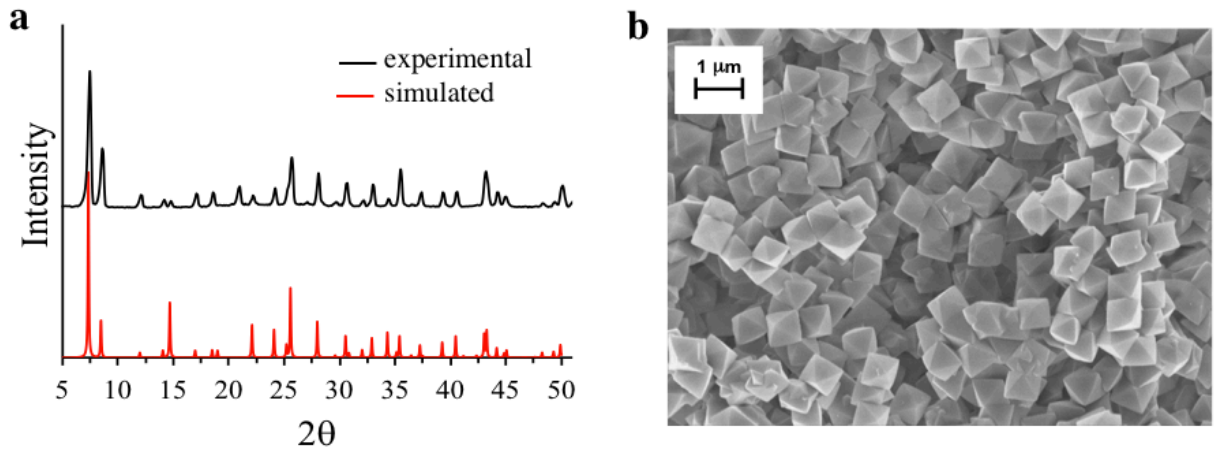

Figure 3.2.1. (a) Experimental PXRD pattern of 9,10-MOF (black) compared with the simulated PXRD pattern (red), (b) SEM image of the 9,10-MOF.

The crystal structure of the 9,10-MOF was determined by synchrotron powder X-ray diffraction (PXRD) at Advanced Photon Source (APS), Argonne National Laboratory (in Argonne, IL, USA). The 9,10-MOF forms a face-centered cubic lattice in the space group Fm-3m with a lattice constant of 20.9073(1) Å. A wire-frame representation of the octahedral and tetrahedral cages of the 9,10-MOF crystal are shown in Figure 3.2.2, along with the structure of the 9,10-ADCA ligand. The distances between nearest anthracene planes in the 9,10-MOF is 7.39 Å. Crystallographic data for 9,10-MOF are summarized in Table 3.4.1. Further details about structure determination and refinement are summarized in the Supplemental Information, Section 3.4.2.

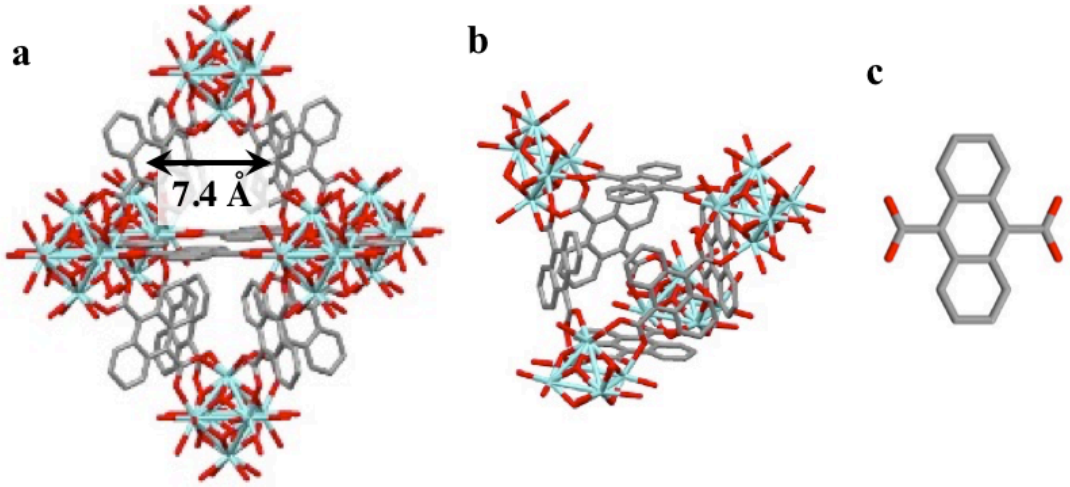

Figure 3.2.2. Wire-frame representation of the octahedral (a) and tetrahedral (b) cages of the 9,10-MOF crystal and the 9,10-ADCA ligand (c).

The absorption and emission spectra of the 9,10-MOF are shown in Figure 3.2.3. The excited-state properties of the 9,10-MOF are comparable to those of the fully protonated ligand.[19] The absorption spectrum of the 9,10-MOF exhibits substantial broadening of the vibronic bands and a large redshift of ~ 75 nm, relative to that of the free ligand. This is indicative of π–π interactions between the anthracene linkers in the ground state.[23] The shape of the 9,10-MOF emission spectrum resembles that of 9,10-ADCA with some broadening of the tail emission. Likewise, both the fluorescence lifetime (Figure 3.4.13) and quantum yield of the 9,10-MOF (τ_f = 6.3 ± 0.6 ns, Φ_f = 0.32 ± 0.10) are with in error of those measured for 9,10-ADCA (τ_f = 5.7 ± 0.3 ns, Φ_f = 0.4 ± 0.05).[19]

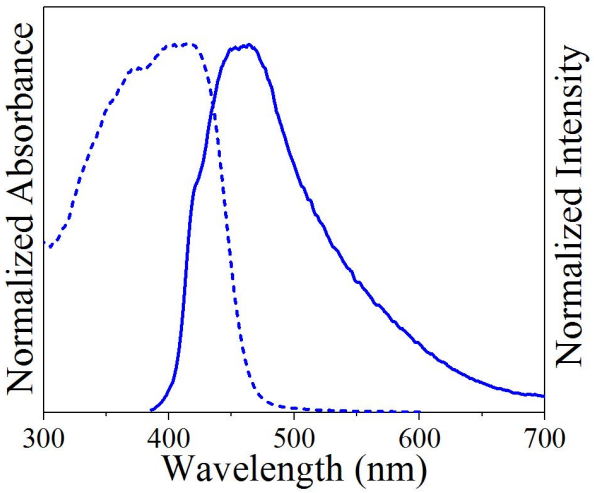

Figure 3.2.3. Normalized absorption (dotted line) and emission (solid line) spectra of the 9,10-MOF, λ_{ex} = 360 nm.

The PdMP sensitizers were anchored to the surface of the MOFs by soaking the powder in a solution of 0.5 mM PdMP in DMF at 80 ºC overnight. The MOFs were then washed several times with fresh DMF to remove excess PdMP. For spectroscopic studies, DMF suspensions of the PdMP@MOF powders (5 mg) were placed in a 24/40 jointed quartz cuvette, capped with a rubber septum and purged with Ar for 1 hour. Upon 532 nm excitation, upconverted emission (λ_{max} ~ 475 nm) was clearly observed from the PdMP@9,10-MOF. However, no sensitized emission was detected from either the PdMP@2,6-MOF or PdMP@1,4-MOF samples measured under the same conditions. To confirm the stability of the MOF to the laser pulse, the sample was syringe filtered and the UV-vis absorption spectrum of the solution was recorded to ensure that no absorbance from the free ligand was observed.

The figures of merit (Φ_f, Φ_{UC}, and I_{th}) for upconversion of PdMP@9,10-MOF were determined via time-resolved photoluminescence spectroscopy. The lifetime of the upconverted emission from PdMP@9,10-MOF was τ_f = 423 ns. The Φ_{ET} was estimated to be ~ 96 % (Figure 3.4.14). By employing equation 3.2.2, a Φ_{UC} of 0.23 % was calculated. To further confirm a TTA-based

mechanism of UC in the PdMP@9,10-MOF, the UC emission was measured as a function of incident laser power (Figure 3.2.4 a). For a TTA-based UC mechanism, the UC emission intensity displays a quadratic dependence in the lower power region where the kinetics are limited by the triplet-state population and becomes linear at higher excitation power where TTA dominates the kinetics.[24-26] The double logarithmic plot of the UC emission intensity of the 9,10-MOF as a function of excitation power density is shown in Figure 3.2.4 b. As anticipated, this plot yielded a slope of ~ 2 at low power density, indicative of a quadratic dependence, and a slope of ~ 1 at the highest power density. The threshold intensity (I_{th}) defines the intensity at which the triplet acceptor deactivation kinetics are driven by TTA.[26] I_{th} was determined from the intersection of the extrapolated slopes and the quadratic and linear dependences and was found to be 142 mW/cm^2.

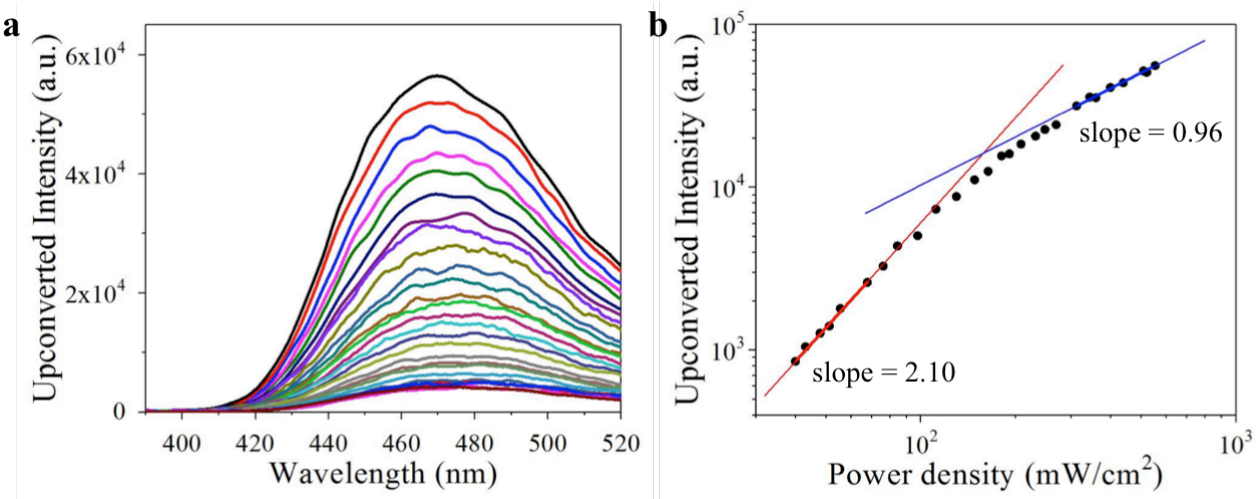

Figure 3.2.4. (a) PdMP@9,10-MOF UC emission map, λ_{ex} = 532 nm (b) Excitation power dependence of UC emission intensity.

Table 3.2.1. Photophysics of ADCA acceptors, PdMP sensitizer and donor-sensitizer pairs

	Φ_f	τ_A (ns)	τ_S (μs)	τ_{UC} (μs)	Φ_{ET}	Φ_{UC}
9,10-ADCA	0.29 ± 0.06	4.2 ± 0.03	2.5 ± 0.02	1.8 ± 0.1	87 %	1.8 %
2,6-ADCA	0.32 ± 0.04	9.0 ±0.9	1.7 ± 0.04	2.3 ± 0.3	91 %	2.7 %
1,4-ADCA	0.27 ± 0.03	9.6 ± 0.1	3.2 ± 0.05	1.6 ± 0.2	84 %	1.3 %
9,10-MOF	0.32 ± 0.10	5.7 ± 0.3	0.6 ± 0.07	0.3 ± 0.1	96 %	0.46 %

Φ_A = acceptor fluorescence quantum yield, τ_A = acceptor fluorescence lifetime, τ_{UC} = upconverted fluorescence lifetime, τ_S = sensitizer fluorescence lifetime in the presence of acceptor, Φ_{ET} = energy transfer quantum efficiency, Φ_{UC} = upconversion quantum yield.

The reduced Φ_{UC} of the MOF relative to the free ligand is likely due to the fact that the PdMP molecules are confined to the surface of the micron-size MOF crystallites. The amount of PdMP in 5 mg of PdMP@9,10-MOF was determined by absorption spectroscopy and found to be 3.0×10^{-9} mol and the amount of anthracene in the same sample was calculated to be 1.1×10^{-6} mol (1×10^{-6} M and 3.6×10^{-4} M, respectively). Based on the size of the MOF crystals (~ 0.5 – 1 μm), for internal anthracene units to be active in the upconversion process, energy transfer between anthracene units must occur efficiently over large distances. Long distance energy transfer has been observed in MOFs.[7-14] Further studies into the energy transfer propensity of the MOFs presented herein are underway. However, there is the potential that anthracene ligands within the MOF are not addressable within the limits of upconversion. Thus, our calculation would represent a lower limit to the upconversion efficiency, as the anthracene concentration would be overestimated via the total absorbance of the MOF at the excitation wavelength. The Φ_{UC} could perhaps be improved by alternate synthetic methods such as reducing the size of the MOF crystallites or introducing larger defects sites to encapsulate PdMP in the interior of the MOF. The Φ_{UC} is dependent upon intrinsic photophysical properties of the sensitizer (Φ_{ISC}) and acceptor (Φ_f) as well as the concentration of the chromophores.[27] Both the Φ_{ET} and Φ_{TTA} are proportional to chromophore concentrations and thus, optimization of these parameters could also improve the

Φ_{UC} and decrease I_{th}.[27] Ideally, the concentration of both sensitizer and acceptor should be increased to maximize Φ_{UC} and Φ_{TTA}, while still low enough to minimize acceptor-to-donor back-ET. Finally, optimization of the chromophore distances and orientations in the MOF could potentially enhance ET processes and improve the overall Φ_{UC}.

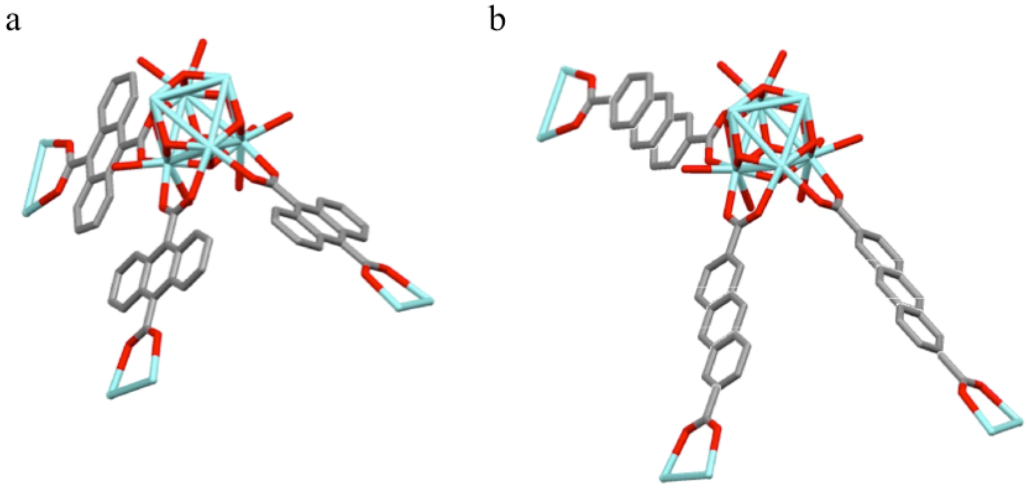

Figure 3.2.5. Representation of the binding geometry of the ADCA ligands around the Zr_6O_4 nodes of 9,10-MOF (a) and 2,6-MOF (b).

Although all three ligands displayed UC emission in solution, only the 9,10-MOF comprises the appropriate arrangement and distance (~ 7.39 Å) between anthracene moieties to enable ET and TTA between the chromophores. The binding geometry of the ADCA ligands about the Zr-nodes of the 9,10-MOF and 2,6-MOF is illustrated in Figure 3.2.5. Refinements of the PXRD data for the 2,6-MOF revealed that this framework is isostructural with UiO-67 and has a lattice constant of 26.97 Å.[21] This corresponds to a distance of ~ 9.53 Å between anthracene planes within the MOF. Although the TTA process requires π-orbital overlap, which, occurs over distances of ~ 10 Å or less, the orientation of the anthracene moieties at this distance does not provide sufficient orbital overlap. In contrast, coordination at the 1 and 4 positions of anthracene is presumed to result in much shorter distances between anthracenes within the 1,4-MOF, assuming a similar

binding configuration at the Zr_6O_4 nodes. In this case, a larger portion of the aromatic plane likely occupies the pores of the 1,4-MOF. Such arrangement allows for strong π–π interactions, which give rise to significant excimer formation.[21, 23] This is corroborated by the broad emission spectrum of the 1,4-MOF (~ 350 – 700 nm), along with a shorter lifetime component (7.5 ns) observed at 400 nm and a longer lifetime component (19.9 ns) at 550 nm.[21] In the 1,4-MOF, the process of excimer formation likely outcompetes ET and TTA processes and is responsible for the absence of UC emission.

3.3. Conclusions

In summary, sensitized upconversion from a zirconium-based anthracenic MOF was demonstrated for the first time. Interestingly, systematic variation of the spacing between the acceptor anthracene units had dramatic effect on the upconversion efficiency. Specifically, only the 9-10-MOF demonstrated upconverted emission. The distance between anthracene linkers in the 2,6-MOF are too large for TTA to occur, while the short distances in the 1,4-MOF inhibit upconversion through competitive excimer formation. The results confirm the anticipated design rules with regard to three-dimensional structure and anthracene spacing to promote upconversion within MOFs. Method to increase the efficiency of the process (concentration studies and further control over orbital and dipole overlap) are areas of continued investigation.

3.4. Supplemental Information

3.4.1. MOF Synthesis and Characterization

3.4.1.1. Materials

9,10-anthracenedicarboxylic acid (9,10-ADCA) 2,6-anthracenedicarboxylic acid (2,6-ADCA) and 1,4-anthracenedicarboxylic acid (1,4-ADCA) were used from a prior study.[19] The 2,6-

MOF and 1,4-MOF were synthesized according to previously described methods.[20] Meso-porphyrin IX (MP) was obtained from frontier scientific. Dimethylformamide was purchased from Alfa-Aeser and used as received. To prepare Pd(II) mesoporphyrin IX (PdMP), MP (0.12 mmol) and K_2PdCl_4 (0.24 mmol) were added to DMF (4 mL) and the solution was refluxed overnight. The product precipitated upon the addition of DI water then collected by filtration and dried under vacuum. To anchor PdMP to the surface of 9,10-MOF, 5 mg of MOF were added to a 1.5 mM solution of PdMP in DMF and heated at 45 ºC for 3 hours then soaked at RT overnight. Excess PdMP was removed by washing with DMF and the surface-modified 9,10-MOFs were collected via centrifugation. All other chemicals and solvents including, $ZrCl_4$, *N,N′*-dimethylformamide (DMF, HPLC grade > 99%), acetic acid (reagent grade > 99%), and formic acid (reagent grade > 99%) were used as received without further purification from Alfa Aesar, Fisher Scientific, or Sigma-Aldrich.

3.4.1.2. Synthesis of 9,10-MOF

The 9,10-MOFs were synthesized using the procedures previously described for UiO-66 and UiO-66(An) with some modifications.[22] $ZrCl_4$ (23.3 mg, 0.1 mmol) and 9,10-ADCA (26.6 mg, 0.1 mmol) were added to a 3-dram vial along with DMF (3 mL) and acetic acid (0.6 mL, 120 equivalents). The vial was capped and sealed with Teflon tape and the mixture was ultrasonicated for 15 minutes. The vial was then placed in an oven and heated at 120 ºC for 24 hours. The reaction solution was filtered immediately collect and a light-yellow powder was collected via vacuum filtration then washed with DMF and ethanol and dried in air.

3.4.1.3. Scanning Electron Microscopy (SEM)

SEM images were collected with a Leo/Zeiss 1550 Schottky field-emission scanning electron microscope equipped with an in-lens detector, operating at 5 kV. Le Bail refinement of the 2,6-MOF powder pattern was performed using Rietica for Windows v2.1 software.

3.4.1.4. Powder X-ray Diffraction (PXRD)

PXRD patterns of MOF samples were obtained using a Rigaku Miniflex 600 with Cu(Kα) radiation (Cu−Kα = 1.5418 Å) in continuous scanning mode (10.0°/min) and a resolution of 0.1° 2θ.

3.4.1.5. Gas Sorption Isotherms

N_2 sorption isotherm measurements were collected on a Quantachrome Autosorb-1 at 77 K. The samples were placed in a 9 mm large bulb sample cell, which was degassed under vacuum for 24 h at 120 °C. The surface areas of the materials were determined by fitting the adsorption data within the 0.05-0.25 P/P_0 pressure range to the BET equations.

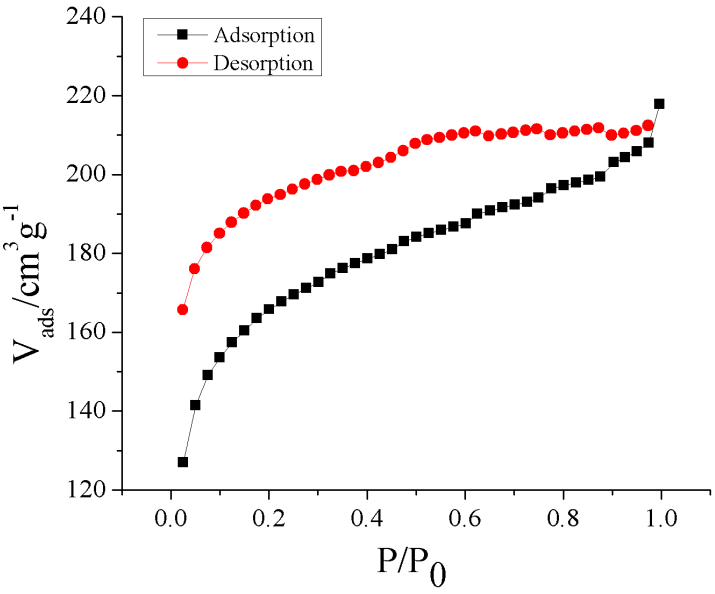

Figure 3.4.1. N_2 sorption isotherm of 9,10-MOF. The Brunauer–Emmett–Teller (BET) surface area of 560 m^2g^{-1} and a pore volume of 0.3191 cm^3g^{-1} were calculated from N_2 adsorption isotherms at 77 K, which is consistent with previous reported values.[22]

3.4.1.6. Thermogravometric Analysis (TGA)

TGA data was collected using a Q-series TGA from TA instruments to analyze thermal stability of materials. 10 mg of sample in a high temperature platinum pan were heated under N_2 from 25 °C to 800 °C at a heating rate of 10 °C/min.

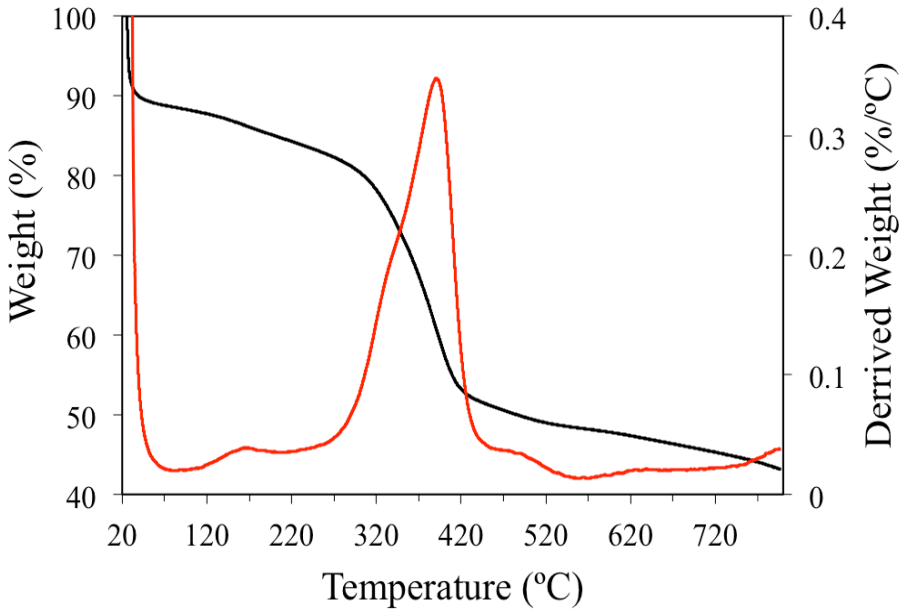

Figure 3.4.2. TGA profile of 9,10-MOF. Thermogravimetric analysis (TGA) of the MOF revealed decomposition of the framework occurs at ~ 350 ºC. The initial ~ 20 % weight losses are attributed to solvent removal from the pores and the residual 40 % weight corresponds to ZrO_2 formed after linker decomposition.

3.4.2. Structure Determination and Refinement of 9,10-MOF

Synchrotron X-ray powder diffraction of the 9,10-MOF was measured on Beamline 17-BM at Advanced Photon Source (APS), Argonne National Laboratory (in Argonne, IL, USA). The beamline operates in transmission geometry, and is equipped with a PerkinElmer® amorphous silicon area detector that collects two-dimensional diffraction images thru program QXRD.[29] The image data of the 9,10-MOF was integrated with program GSAS-II to an XRD profile of the

intensity versus 2-theta format.[30] Indexing of the XRD profile and further refinement analysis was performed with TOPAS version 5. The X-ray wavelength was 0.45260 Å.

Indexing results suggested a face-centered cubic lattice with a lattice constant of 20.9073(1) Å and five candidate space groups, F23, Fm-3, F432, F-43m and Fm-3m. The XRD of 9,10-MOF is similar to that of the well-known UiO-66, which has a space group of Fm-3m and an edge length of 20.7004 Å.[30] From the chemistry point of view, 9,10-anthracenedicarboxylate in the 9,10-MOF and benzene-1,4-dicarboxylate in UiO-66 are both bidentate and have the same symmetry. Based on the similarities in both the XRD and the chemical components, the 9,10-MOF is very likely to be isostructural with the UiO-66. An initial structure model of the 9,10-MOF was built based on UiO-66 with the correct ligand. Pawley refinement confirmed the lattice and the space group (Table 3.4.1, Figure 3.4.3). The initial Rietveld refinement showed a poor fit of this framework-only model to the data, as the synthesized sample contained solvent molecules, most likely DMF and water. Adding free oxygen atoms and DMF molecules in the pore improved the fit, but not to level of goodness satisfactory for publishing the refinement. This is due to the inadequacy of approaching the disordered solvent electron density with oxygen atoms or molecular moieties. Hence instead the Difference Envelope Density (DED) ρ_{Δ} method was applied to illustrate the solvent distribution and to further confirm the framework structure.

The DED method has been used very successfully for estimation of MOF guest molecules positions and differences in the framework structures.[32-34] It requires only a few reflection intensities from a PXRD pattern for input. In this application of studying the 9,10-MOF, 10 low angle reflection integrated intensities (F^2_{obs}) were extracted the previous Pawley refinement and used for generation of Structure Envelope (SE) Densities.

Table 3.4.1. Final *R*-factors and main refinement parameters of the Pawley whole pattern decompositions.

Compound	**9,10-MOF**
Crystal system	Cubic
Space group	*F m -3 m*
a [Å]	20.9073(1)
d_{min} [Å]	0.96
R_p [%]	1.24
R_{wp} [%]	1.65
GOF	1.37

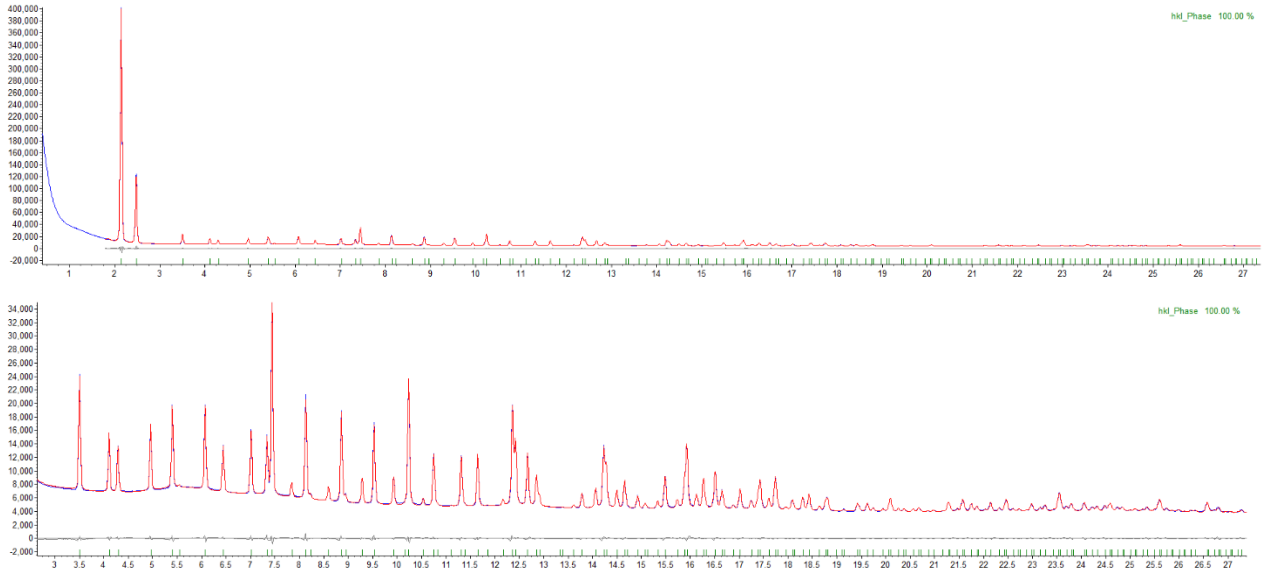

Figure 3.4.3. Pawley refinement plots of the 9,10-MOF XRD data: the whole pattern (top) and an enlarged view of region excluding the two strong low angle peaks (bottom).

3.4.2.1. Calculation of structure factor phases

The initial model of the 9,10-MOF was used to generate the structure factor phases. In case of the UiO-66, the structural model was taken from a previous publication with the unit cell changed to match that of the 9,10-MOF, a = 20.9073 Å.[22] The ideal intensities F^2_{calc} for these structures were calculated with XFOG program from SHELXTL software package.[35] Using these intensities the structure factor phases for the reflections were generated with LIST 2 instruction in the INS-file via SHELXL software.

3.4.2.2. Generation and visualization of envelope densities

Reflections {111}, {002}, {022}, {311}, {222}, {004}, {331}, {422}, {333} and {044} were chosen for Structure Envelope (SE) densities generation in both cases. Combination of F^2_{calc} and were used for generation of the calculated SE densities for the 9,10-MOF and UiO-66 ρ_{calc}, while the combinations of F^2_{obs} a and φ^{calc}_{hkl} were used to create observed SE density ρ_{obs} for the 9,10-MOF. SE densities was produced by SUPERFLIP software in XPLOR format and visualized with UCSF Chimera software (Figure 3.4.4 a and b).[36-37] The contents of input SUPERFLIP files (INFIP-format files) can be found below. Difference Envelope Densities (DED) ρ_{Δ} (Figure 3.4.4 c and Figure 3.4.5) were generated similarly as previously described. DED built from ρ_{obs} and ρ_{calc} for the 9,10-MOF (Figure 3.4.4 c) contains peaks which are located only in the pores of the framework and correspond to the disordered solvent molecules within the cavities. It is important to mention that we did not observe any peaks located in close proximity to the atomic positions of the framework. This suggests the overall structural model for the framework of the 9,10-MOF is correct. In addition, DED $\rho_{\Delta UiO\text{-}66}$ shows the difference between ρ_{obs} for the 9,10-MOF and ρ_{calc} for the UiO-66 (Figure 3.4.5). Besides similar solvent peaks, this DED map also contains peaks on each side of the benzene ring, which is attributed to the signal from the two additional rings of the anthracene. This also confirms the presence and layout of the anthracenedicarboxylate ligand in the structure of the 9,10-MOF.

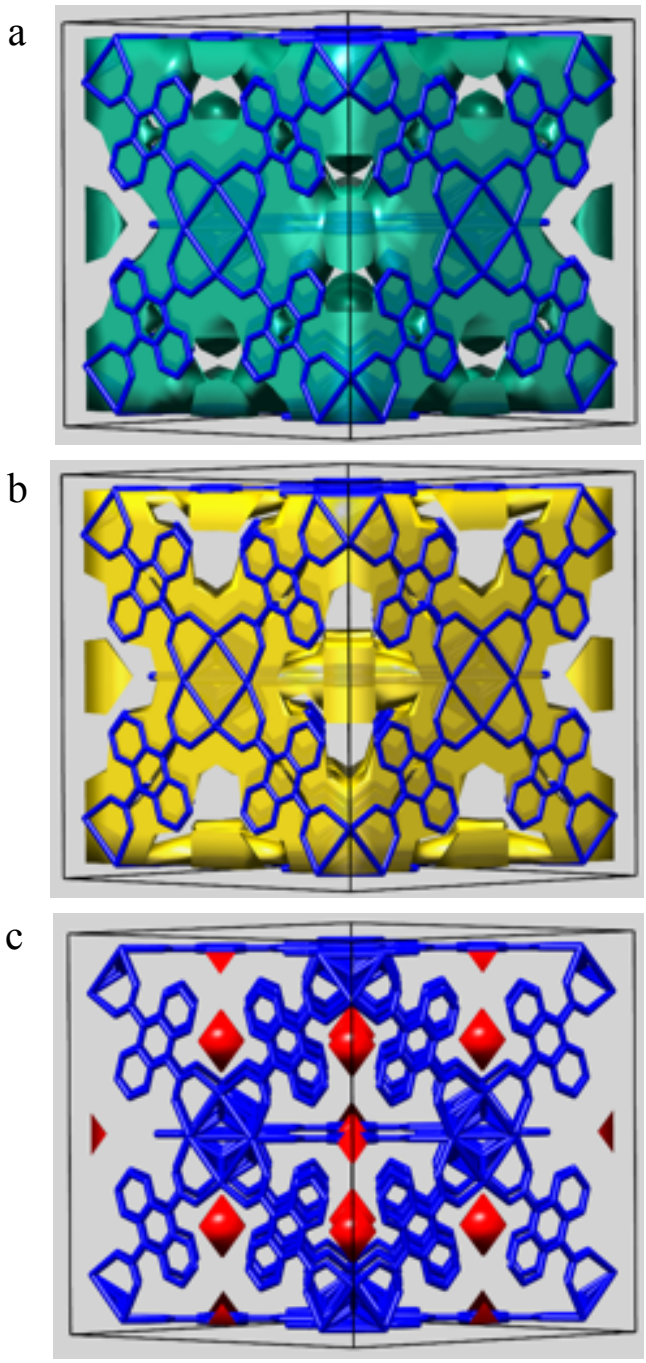

Figure 3.4.4. Structural model of the 9,10-MOF overlapped with Structure Envelopes generated from 9,10-MOF data sets: observed, ρ_{obs} (a) calculated, ρ_{calc} (b) and their Difference Envelope Density, ρ_{Δ} (c).

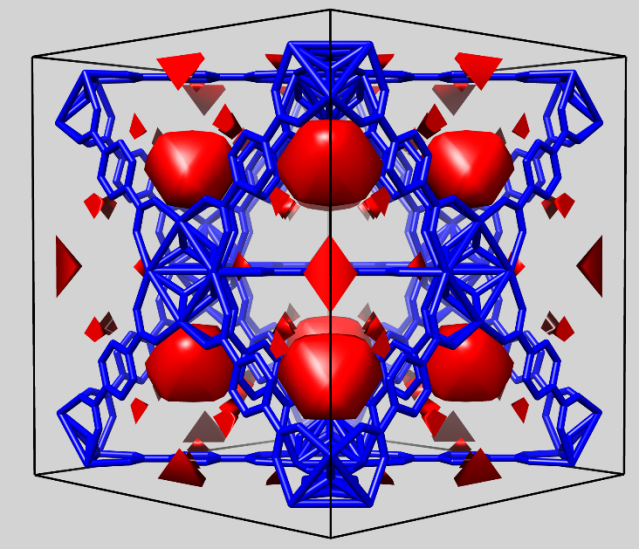

Figure 3.4.5. Structural model of UiO-66 overlapped with Difference Envelope Density $\rho_{\Delta UiO\text{-}66}$ generated as the difference between ρ_{obs} for the 9,10-MOF and ρ_{calc} for UiO-66.

3.4.3. Spectroscopic Measurements

3.4.3.1. Steady-State Absorption Spectroscopy

The steady-state absorption spectra were obtained using an Agilent Technologies 8453 UV-Vis diode array spectrophotometer (1 nm resolution) where the spectra were recorded with samples prepared in a 1 cm quartz cuvette. The same instrument was used to obtain diffuse reflectance spectra of MOF powders, where the sample compartment was replaced with an integration sphere. The powder samples were diluted by mixing with $BaSO_4$.

3.4.3.2. Steady-state Emission Spectroscopy and Time-Resolved Emission Lifetimes

Approximately 3 mg of MOF powder were suspended in 3 mL DMF, all samples were purged with argon before measurements were performed and the sample was continuously stirred during the emission measurements. The ligand samples were prepared at concentrations of ~ 8 μM

in DMF. The protonated (ADCA) and deprotonated (ADC^{2-}) ligand samples were prepared in aqueous solutions, using HCl or NaOH to achieve pH values of ~ 2 and 10.5, respectively.

Time-resolved fluorescence lifetime of the 9,10-MOF was obtained via the time-correlated single photon counting technique (TCSPC) with a modified QuantaMaster Model QM-200-4E emission spectrophotometer from Photon Technology, Inc. (PTI) equipped with a 350 nm LED and a Becker & Hickl GmbH PMH-100 PMT detector with time resolution of < 220 ps FWHM. Florescence lifetime decays were deconvoluted from the time-dependent florescence signal and the instrument response function using the fluorescence decay analysis software, DecayFit, available online (Fluortools, www.fluortools.com. For power dependence studies, the excitation source was replaced by a 532 nm continues wave laser and the incident power was tuned using neutral density filters.

Quantum yields of fluorescence and steady-state emission spectra were measured in DMF. The steady-state emission spectra were obtained using the same QuantaMaster Model QM-200-4E where the sample compartment was replaced with an integrating sphere (PTI). The excitation light source was a 75 W Xe arc lamp (Newport). The detector was a thermoelectrically cooled Hamamatsu 1527 photomultiplier tube (PMT). Measurements were performed in triplicate using three separately prepared suspensions of MOF. Kinetic traces were analyzed using Origin.

To ensure stability of the MOF and the absence of free linker, the solutions were syringe filtered and emission was monitored at the maximum wavelength of emission for each ligand after the emission experiments were completed.

3.4.3.3. Sample Preparation for UC Measurements

Sample solutions of 0.35 mM ADCA ligand and 43 μM PdMP were prepared in DMF and deaerated by purging with Ar for ~ 30 minutes. The MOF powders were suspended in DMF and the samples were deaerated by purging with Ar for ~ 1 hour.

3.4.3.4. Upconversion Measurements

Single wavelength emission decay kinetics spectra were recorded using an LP 920 laser flash photolysis system (Edinburgh Instruments) equipped with a PMT detector (R928, Hamamatsu), using either a 355 nm or 532 nm Nd:YAG laser (Spectra-Physics Quanta-Ray Lab) operating at 1 Hz as the excitation source. This same laser system, equipped with an image intensified CCD (ICCD) camera detector, was used to collect time-gated emission spectra. The upconversion quantum efficiencies (Φ_{UC}) and energy transfer efficiencies (Φ_{ET}) were determined from this data by comparing the prompt and delayed fluorescence signals.

3.4.4. Supplementary Figures

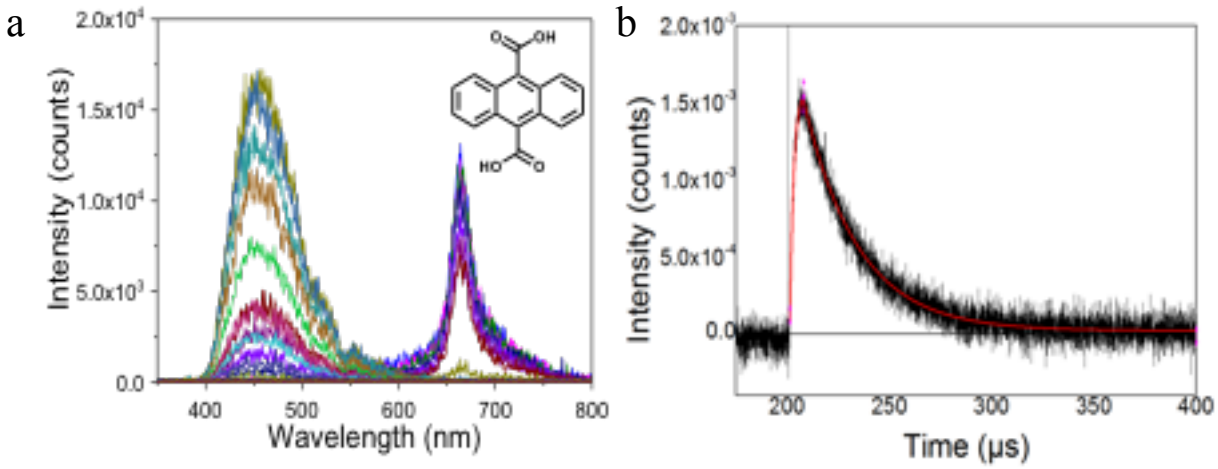

Figure 3.4.6. Time-resolved emission map for sample of 9,10-ADCA/PdMP sample excited at 532 nm (a), emission decay measured at 460 nm excited at 532 nm and monoexponential decay fit. (b)

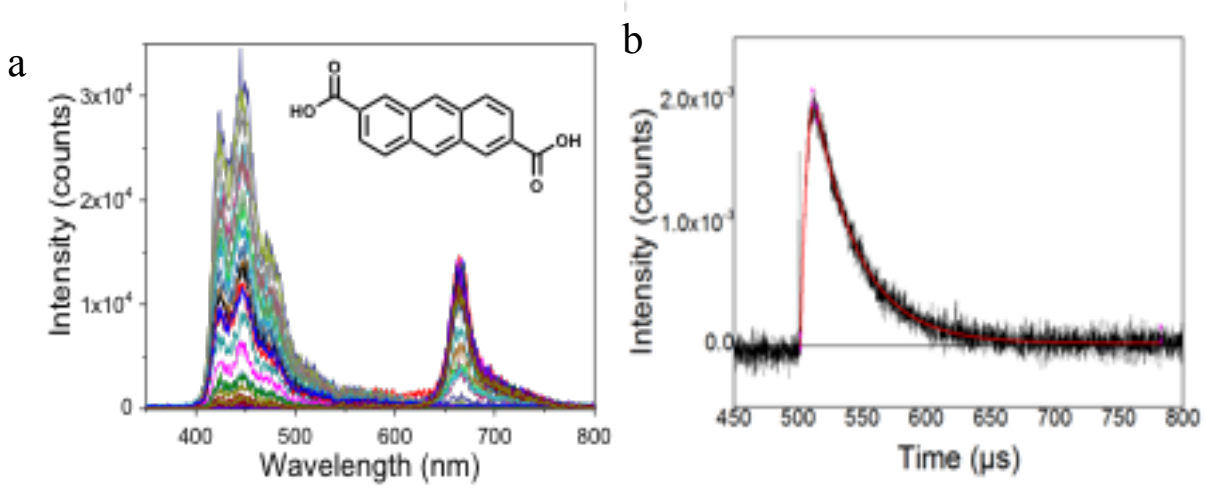

Figure 3.4.7. Time-resolved emission map for sample of 2,6-ADCA/PdMP sample excited at 532 nm (a), emission decay measured at 440 nm excited at 532 nm and monoexponential decay fit (b).

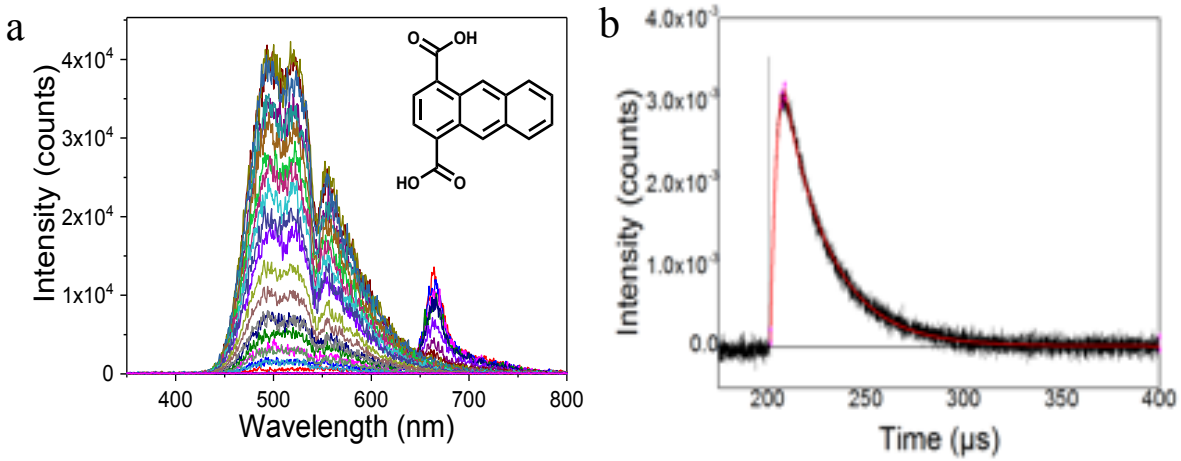

Figure 3.4.8. Time-resolved emission map for sample of 1,4-ADCA/PdMP excited at 532 nm (a), emission decay measured at 440 nm excited at 532 nm and monoexponential decay fit (b).

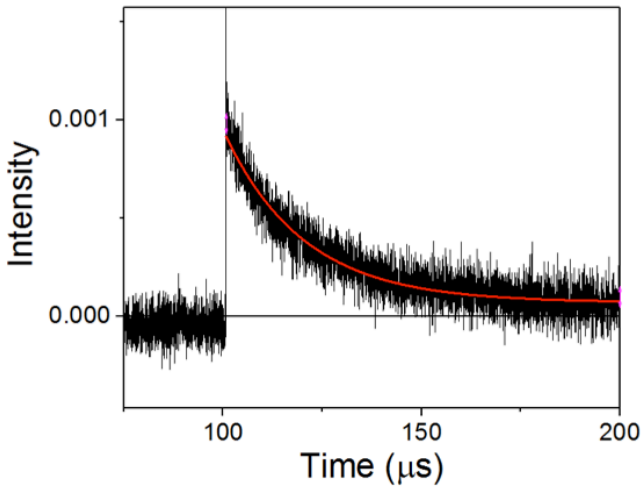

Figure 3.4.9. Emission decay measured at 666 nm excited at 532 nm for sample for PdMP in DMF and monoexponential decay fit.

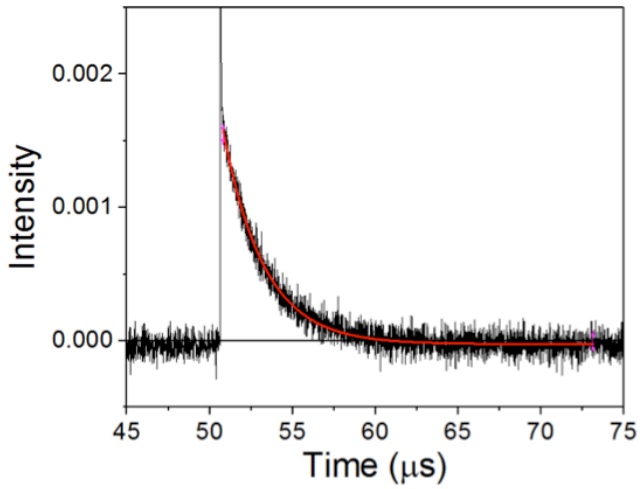

Figure 3.4.10. Emission decay measured at 666 nm excited at 532 nm for sample for 9,10-ADCA/PdMP sample and monoexponential decay fit.

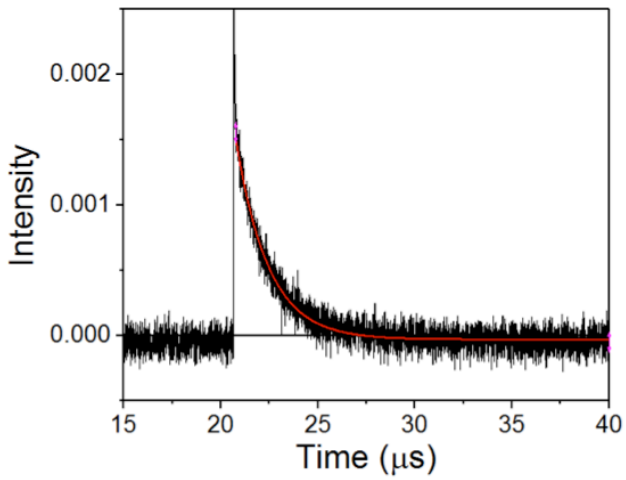

Figure 3.4.11. Emission decay measured at 666 nm excited at 532 nm for sample for 2,6-ADCA/PdMP sample and monoexponential decay fit

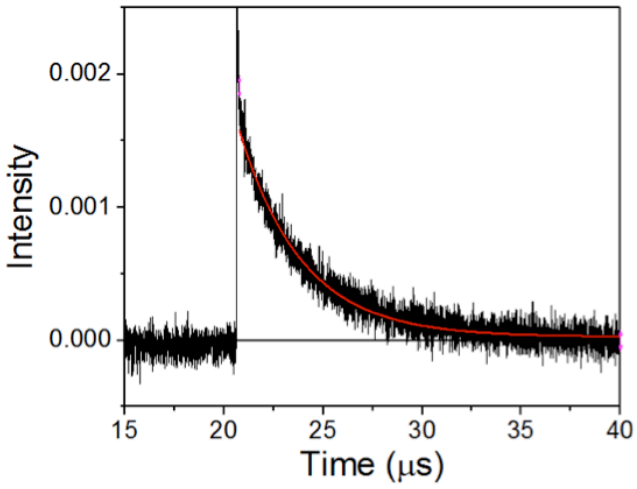

Figure 3.4.12. Emission decay measured at 666 nm excited at 532 nm for sample for 1,4-ADCA/PdMP sample and monoexponential decay fit.

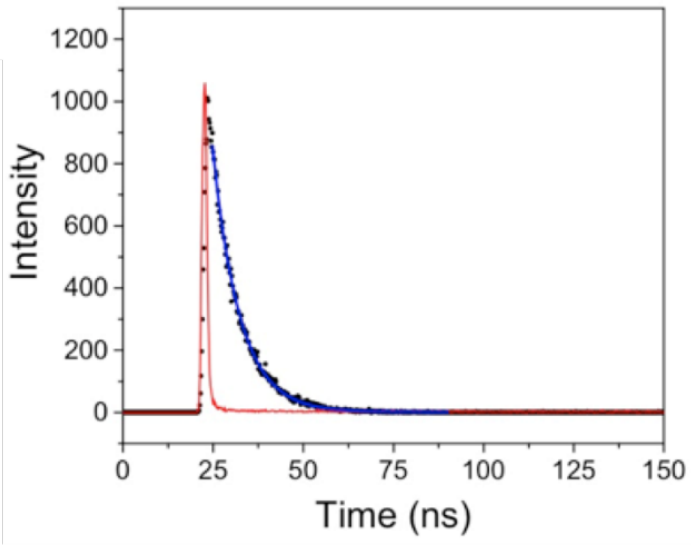

Figure 3.4.13. Raw data from TCSPC measurement of 9,10-MOF emission at 370 nm using 310 nm excitation (black circles), including the instrument response function (red line) and lifetime decay fit (blue line).

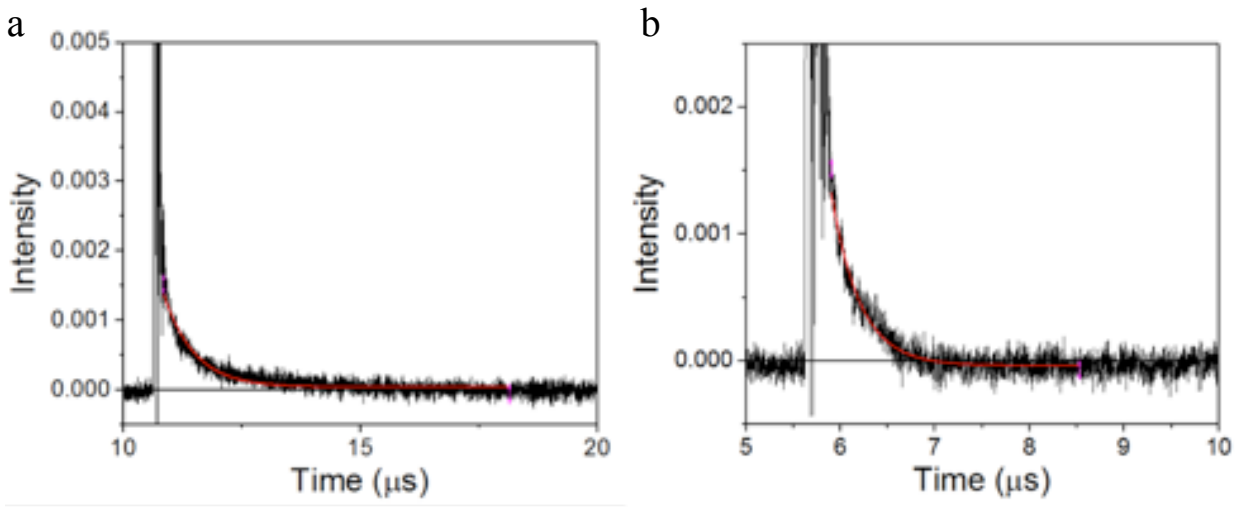

Figure 3.4.14. PdMP@9,10-MOF emission kinetics measured at 470 nm (a) and 666 nm (b) under 532 nm excitation.

3.5. References

1. Trupke, T.; Green, M. A.; Würfel, P., Improving Solar Cell Efficiencies by Up-Conversion of Sub-Band-Gap Light. *J. Appl. Phys.* **2002,** *92* (7), 4117-4122.

2. Singh-Rachford, T. N.; Castellano, F. N., Photon Upconversion Based on Sensitized Triplet–Triplet Annihilation. *Coord. Chem. Rev.* **2010,** *254*, 2560-2573.

3. Schulze, T. F.; Schmidt, T. W., Photochemical Upconversion: Present Status and Prospects for its Application to Solar Energy Conversion. *Energy. Environ. Sci.* **2015,** *8* (1), 103-125.

4. Islangulov, R. R.; Lott, J.; Weder, C.; Castellano, F. N., Noncoherent Low-Power Upconversion in Solid Polymer Films. *J. Am Chem. Soc.* **2007,** *129* (42), 12652-12653.

5. Jiang, X.; Guo, X.; Peng, J.; Zhao, D.; Ma, Y., Triplet–Triplet Annihilation Photon Upconversion in Polymer Thin Film: Sensitizer Design. *ACS Appl. Mater. Interfaces.* **2016,** *8* (18), 11441-11449.

6. Hill, S. P.; Banerjee, T.; Dilbeck, T.; Hanson, K., Photon Upconversion and Photocurrent Generation via Self-Assembly at Organic–Inorganic Interfaces. *J. Phys. Chem. Lett.* **2015,** *6* (22), 4510-4517.

7. Kent, C. A.; Liu, D.; Meyer, T. J.; Lin, W., Amplified Luminescence Quenching of Phosphorescent Metal–Organic Frameworks. *J. Am. Chem. Soc.* **2012,** *134* (9), 3991-3994.

8. Kent, C. A.; Mehl, B. P.; Ma, L.; Papanikolas, J. M.; Meyer, T. J.; Lin, W., Energy Transfer Dynamics in Metal-Organic Frameworks. *J. Am. Chem. Soc.* **2010,** *132* (37), 12767-9.

9. Lee, C. Y.; Farha, O. K.; Hong, B. J.; Sarjeant, A. A.; Nguyen, S. T.; Hupp, J. T., Light-Harvesting Metal–Organic Frameworks (MOFs): Efficient Strut-to-Strut Energy Transfer in Bodipy and Porphyrin-Based MOFs. *J. Am. Chem. Soc.* **2011,** *133* (40), 15858-15861.

10. Lin, J.; Hu, X.; Zhang, P.; Van Rynbach, A.; Beratan, D. N.; Kent, C. A.; Mehl, B. P.; Papanikolas, J. M.; Meyer, T. J.; Lin, W.; Skourtis, S. S.; Constantinou, M., Triplet Excitation Energy Dynamics in Metal–Organic Frameworks. *J. Phys. Chem. C* **2013,** *117* (43), 22250-22259.

11. Maza, W. A.; Padilla, R.; Morris, A. J., Concentration Dependent Dimensionality of Resonance Energy Transfer in a Postsynthetically Doped Morphologically Homologous Analogue of UiO-67 MOF with a Ruthenium(II) Polypyridyl Complex. *J. Am. Chem. Soc.* **2015,** *137* (25), 8161-8168.

12. Son, H.-J.; Jin, S.; Patwardhan, S.; Wezenberg, S. J.; Jeong, N. C.; So, M.; Wilmer, C. E.; Sarjeant, A. A.; Schatz, G. C.; Snurr, R. Q.; Farha, O. K.; Wiederrecht, G. P.; Hupp, J. T., Light-Harvesting and Ultrafast Energy Migration in Porphyrin-Based Metal–Organic Frameworks. *J Am. Chem. Soc.* **2013,** *135* (2), 862-869.

13. Wang, C.; Lin, W., Diffusion-Controlled Luminescence Quenching in Metal−Organic Frameworks. *J. Am. Chem. Soc.* **2011,** *133* (12), 4232-4235.

14. Maza, W. A.; Morris, A. J., Photophysical Characterization of a Ruthenium(II) Tris(2,2′-bipyridine)-Doped Zirconium UiO-67 Metal–Organic Framework. *J. Phys. Chem. C* **2014,** *118* (17), 8803-8817.

15. Mahato, P.; Monguzzi, A.; Yanai, N.; Yamada, T.; Kimizuka, N., Fast and Long-Range Triplet Exciton Diffusion in Metal-Organic Frameworks for Photon Upconversion at Ultralow Excitation Power. *Nat. Mater.* **2015,** *14* (9), 924-930.

16. Oldenburg, M.; Turshatov, A.; Busko, D.; Wollgarten, S.; Adams, M.; Baroni, N.; Welle, A.; Redel, E.; Wöll, C.; Richards, B. S.; Howard, I. A., Photon Upconversion at Crystalline Organic-Organic Heterojunctions. *Adv. Mater.* **2016,** *28* (38), 8477-8482.

17. Deng, F.; Blumhoff, J.; Castellano, F. N., Annihilation Limit of a Visible-to-UV Photon Upconversion Composition Ascertained from Transient Absorption Kinetics. *J. Phys. Chem. A* **2013,** *117* (21), 4412-4419.

18. Gray, V.; Dzebo, D.; Lundin, A.; Alborzpour, J.; Abrahamsson, M.; Albinsson, B.; Moth-Poulsen, K., Photophysical Characterization of the 9,10-disubstituted Anthracene Chromophore and its Applications in Triplet–Triplet Annihilation Photon Upconversion. *J. Mater. Chem. C* **2015,** *3* (42), 11111-11121.

19. Rowe, J. M.; Hay, J. M.; Maza, W. A.; Chapleski, R. C.; Soderstrom, E.; Troya, D.; Morris, A. J., Systematic Investigation of the Excited-State Properties of Anthracene-Dicarboxylic Acids. *J. Photochem. Photobiol. A* **2017,** *337*, 207-215.

20. Crosby, G. A.; Demas, J. N., Measurement of Photoluminescence Quantum Yields. Review. *J. Phys. Chem.* **1971,** *75* (8), 991-1024.

22. Pu, S.; Xu, L.; Sun, L.; Du, H., Tuning the Optical Properties of the Zirconium-UiO-66 Metal-Organic Framework for Photocatalytic Degradation of Methyl Orange. *Inorg. Chem. Comm.* **2015,** *52*, 50–52.

23. Chandross. E. A.; Furguson, J. Absorption and Excimer Fluorescence Spectra of Sandwich Dimers of Substituted Anthracenes, *J. Chem. Phys*. **1966,** *45* (10), 3554-3564.

24. Haefele, A.; Blumhoff, J.; Khnayzer, R. S.; Castellano, F. N., Getting to the (Square) Root of the Problem: How to Make Noncoherent Pumped Upconversion Linear. *J. Phys. Chem. Lett.* **2012,** *3* (3), 299-303.

25. Jones, S.; Atherton, J. C. C.; Elsegood, M. R. J.; Clegg, W., Dimethyl 9,10-anthracenedicarboxylate: A Centrosymmetric Transoid Molecule. *Acta. Cryst. C.* **2000,** *56* (7), 881-883.

26. Monguzzi, A.; Mezyk, J.; Scotognella, F.; Tubino, R.; Meinardi, F., Upconversion-Induced Fluorescence in Multicomponent Systems: Steady-State Excitation Power Threshold. *Phys. Rev. B* **2008,** *78* (19), 195112.

27. Monguzzi, A.; Tubino, R.; Hoseinkhani, S.; Campione, M.; Meinardi, F., Low Power, Non-coherent sensitized Photon Up-conversion: Modelling and Perspectives. *Phys. Chem. Chem. Phys.* **2012,** *14* (13).

28. Katz, M. J.; Brown, Z. J.; Colón, Y. J.; Siu, P. W.; Scheidt, K. A.; Snurr, R. Q.; Hupp, J. T.; Farha, O. K., A Facile Synthesis of UiO-66, UiO-67 and Their Derivatives. *Chem. Comm.* **2013,** *49* (82).

29. http://qxrd.sourceforge.net/

30. Toby, B. H.; Von Dreele, R. B., GSAS-II: The Genesis of a Modern Open-Source All-Purpose Crystallography Software Package. *J. Appl. Cryst.* **2013,** *46* (2), 544-549.

31. Cavka, J. H.; Jakobsen, S.; Olsbye, U.; Guillou, N.; Lamberti, C.; Bordiga, S.; Lillerud, K. P., A New Zirconium Inorganic Building Brick Forming Metal Organic Frameworks with Exceptional Stability. *J. Am. Chem. Soc.* **2008,** *130* (42), 13850-13851.

32. Chen, Y.-P.; Liu, Y.; Liu, D.; Bosch, M.; Zhou, H.-C., Direct Measurement of Adsorbed Gas Redistribution in Metal–Organic Frameworks. *J. Am. Chem. Soc.* **2015,** *137* (8), 2919-2930.

33. Wriedt, M.; Sculley, J. P.; Yakovenko, A. A.; Ma, Y.; Halder, G. J.; Balbuena, P. B.; Zhou, H.-C., Low-Energy Selective Capture of Carbon Dioxide by a Pre-designed Elastic Single-Molecule Trap. *Angew. Chem. Int. Ed.* **2012,** *51* (39), 9804-9808.

34. Yakovenko, A. A.; Wei, Z.; Wriedt, M.; Li, J.-R.; Halder, G. J.; Zhou, H.-C., Study of Guest Molecules in Metal–Organic Frameworks by Powder X-ray Diffraction: Analysis of Difference Envelope Density. *Cryst. Grow. Des.* **2014,** *14* (11), 5397-5407.

35. Sheldrick, G. M. *SHELXTL 2008/4 Structure Determination Software Suite*. Bruker AXS, Madison, Wisconsin, USA, **2008**.

36. Palatinus, L.; Chapuis, G., SUPERFLIP: A Computer Program for the Solution of Crystal Structures by Charge Flipping in Arbitrary Dimensions. *J. Appl. Cryst.* **2007,** *40* (4), 786-790.

37. Pettersen, E. F.; Goddard, T. D.; Huang, C. C.; Couch, G. S.; Greenblatt, D. M.; Meng, E. C.; Ferrin, T. E., UCSF Chimera: A Visualization System for Exploratory Research and Analysis. *J. Comput. Chem.* **2004,** *25* (13), 1605-1612.

4. Tuning the Interchromophore Distances in Pillared Paddlewheel Zn-porphyrin MOFs as Platforms for Systematic Energy-Transfer Studies

4.1. Introduction

Natural photosynthetic systems contain highly ordered arrays of chromophores to absorb sunlight and efficiently funnel the energy to a reaction center. Energy harvesting materials that mimic natural photosynthetic processes are of interest due to their potential applications in solar energy conversion. Porphyrins are often used as photosensitizers in constructing artificial photosynthetic systems because of their structural and chromophoric similarity to chlorophyll pigments found in nature.[1] Owing to their modularity and highly-ordered crystal structures, metal-organic frameworks (MOFs) provide a good platform for systematic studies of energy-transfer processes. Furthermore, MOFs have shown a proclivity for efficient energy transfer.[2-7] Long-range, directional energy transfer has been demonstrated in MOFs comprising Zn(II) porphyrin-based struts.[6,8]

Recently, Hupp et. al. showed that energy transfer is further enhanced when the distance between the chromophores is reduced.[9] In this study, solvent-assisted linker exchange (SALE) was performed on a MOF thin-film comprising pillared paddlewheel free-base porphyrins in order to collapse the 3D framework to a 2D framework. Spectroscopic studies indicated that excitons travel through ~ 6–8 porphyrin layers in the 3D films and ~ 9−11 layers in 2D films.

In order to further understand the factors that govern energy transfer in porphyrin-based MOFs, we have synthesized a series of three MOFs containing Zn(II) meso-tetra(4-carboxyphenyl) porphyrin (ZnTCPP) as the struts and either pyrazine (pyz, PYZ-MOF), 4,4′-bipyridine (bpy, BPY-MOF) or 1,4-di(4-pyridyl)benzene (dpbz, DPBZ-MOF) as the pillars (L2, Figure 4.1.1). The photophysical properties of the MOFs were characterized by steady-state diffuse

reflectance, and steady-state emission spectroscopy and time-correlated single-photon counting (TCSPC) measurements. Fluorescence quenching studies were performed to gain insight into the effects of porphyrin separation distance on energy transfer processes in the MOFs.

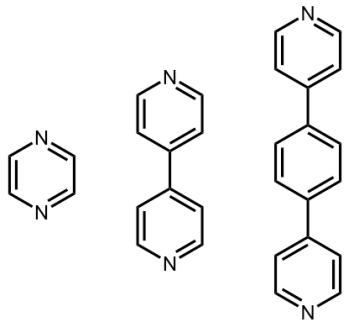

Figure 4.1.1. Structures of pyradine, 4,4′-bipyridine and 1,4-di(4-pyridyl)benzene ligands.

4.1.1. Synthesis and Structural Characterization

The ZnTCPP-L2 MOFs were synthesized using slight modifications of previously reported methods.[10] $Zn(NO_3)_2$•$6H_2O$ (0.054 mmol) and H_2TCPP (0.029 mmol) were added to a 1-dram vial along with 1.2 mL of DMF. The solutions were sonicated for ~ 5 minutes, then placed in an oven and heated to 80 ºC at a rate of 1 ºC/min and held for 2 hours. After 2 hours, L2 (0.029 mmol) and 0.5 mL of 0.03 M HNO_3 in ethanol was added and the reaction mixture was heated at 80 ºC for ~ 16 hours then cooled to room temperature at a rate of 1ºC/min. The reaction solution was decanted and the resulting small, purple MOF crystals were washed several times with DMF.

MOF single-crystals were obtained following the synthetic procedure described above, with the amounts of ZnTCPP and L2 reduced to 0.027 mmol and 0.0145 mmol, respectively, and analyzed by single-crystal X-ray diffraction (XRD) analysis. The quality of the XRD data obtained for PYZ-MOF and DPBZ-MOF was too weak to determine the crystal structures, though single-crystal XRD analysis of BPY-MOF (Figure 4.1.2) revealed that the MOF contains 2D networks of ZnTCPP ligands connected by $Zn_2(COO)_4$ paddlewheel clusters (secondary building units,

SBUs) paddlewheel layer. The distance between the paddlewheel layers (ZnTCPP to Zn SBU) was found to be ~ 11.5 Å, and the solvent between the layers was disordered.

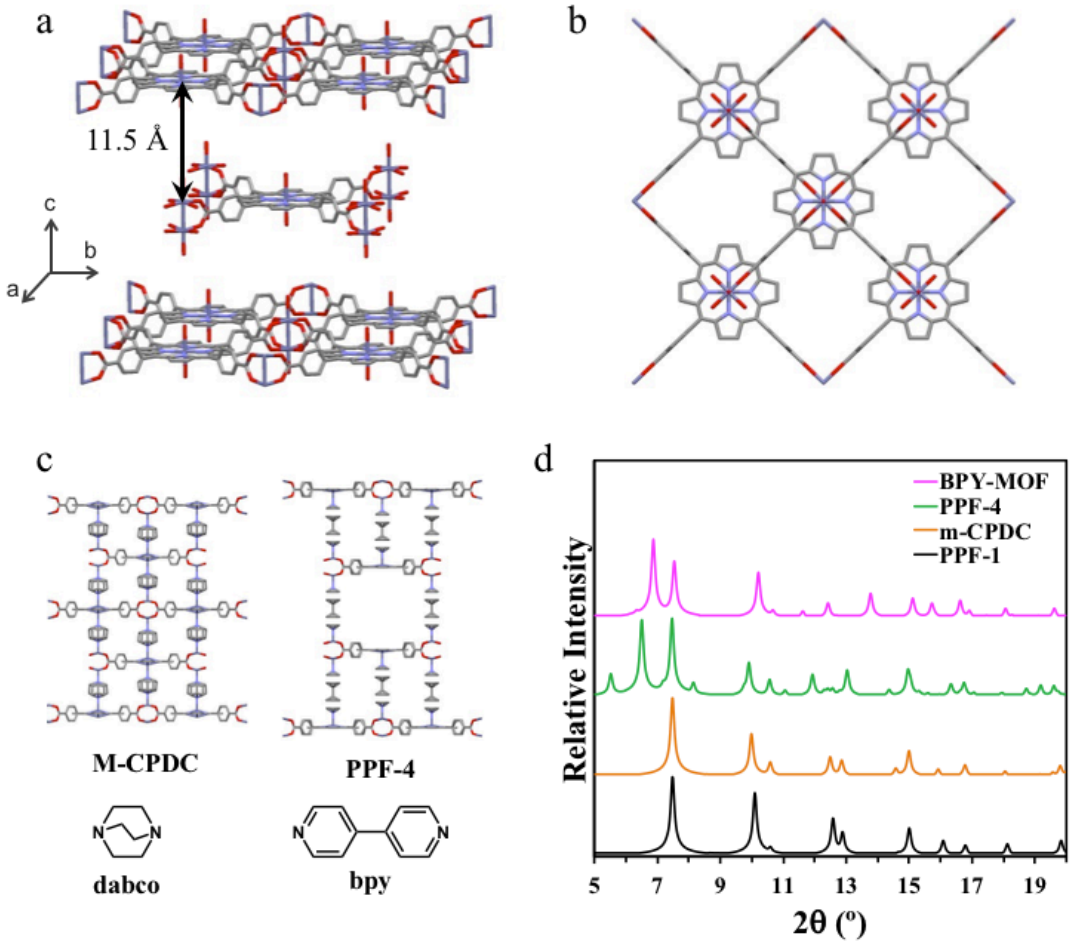

Figure 4.1.2. Single-crystal XRD structure obtained for BPY-MOF (a) and view down the *c*-axis showing the configuration of the 2D ZnTCPP/Zn paddlewheel layers (b), the crystal structures of m-CPDC and PPF-4, from references 9 and 11, illustrating two different types of pillared formation in ZnTCPP/Zn paddlewheel MOFs with the corresponding dabco and bpy pillar ligands shown below (c) along with the calculated PXRD patterns (d) of the BPY-MOF (pink), PPF-4 (green), m-CPBC (orange) and PPF-1 (black) from 9, 11 and 10.

The structure of PYZ-MOF is likely analogous to a previously reported Zn paddlewheel framework, m-CPDC, composed of ZnTCPP layers pillared by diaza-[2.2.2]bicycrooctan (dabco) ligands (Figure 4.1.3 c).[10] The PXRD pattern of mCPB calculated from the single-crystal XRD

data is shown in Figure 4.1.2 d along with the simulated PXRD patterns of PPF-4 and PPF-1, obtained from the referenced papers.[10-11] The peak at 7.5º 2θ is ascribed to the distance between the ZnTCPP and Zn-paddlewheel components (~ 11.8 Å), measured from the plane of the 2D ZnTCPP/Zn paddlewheel.[11-12] Additionally, the peak at ~ 7º 2θ that appears in the pattern of BPY-MOF, as well as the three reference MOFs, corresponds with the distance between layers.[12] DPBZ-MOF is expected to have a similar structure to BPY-MOF, with larger spacing between layers due to the length of the ligand.

The crystallinity of PYZ-MOF, BPY-MOF and DPBZ-MOF was assessed using synchrotron powder X-ray diffraction (PXRD) techniques and the PXRD patterns (Figure 4.1.3 a) were compared to the simulated powder pattern of BPY-MOF (PPF-4).[10] The characteristic peak at ~ 7.5 º 2θ is visible in the experimental powder patterns of all three MOFs, which indicates that each MOF comprises ZnTCPP/Zn paddlewheel layers. The most intense peaks in the simulated PXRD pattern for BPY-MOF, specifically ~ 6.3º, 6.9º, 10.2º and 12.4º, are clearly discernable in experimental pattern. Furthermore, these peaks are distinctly present in the powder patterns of PYZ-MOF and DPBZ-MOF, suggesting that the three MOFs are isostructural. The SEM images (Figure 4.1.3 b, c and d) reveal that the three ZnTCPP-L2 MOFs form square, plate-like structures ~ 80 – 100 μm in size. The amorphous material on the surface of the BPY-MOF crystals DPBZ-is likely responsible for the additional sharp peak that appear in the experimental PXRD pattern of the MOF.

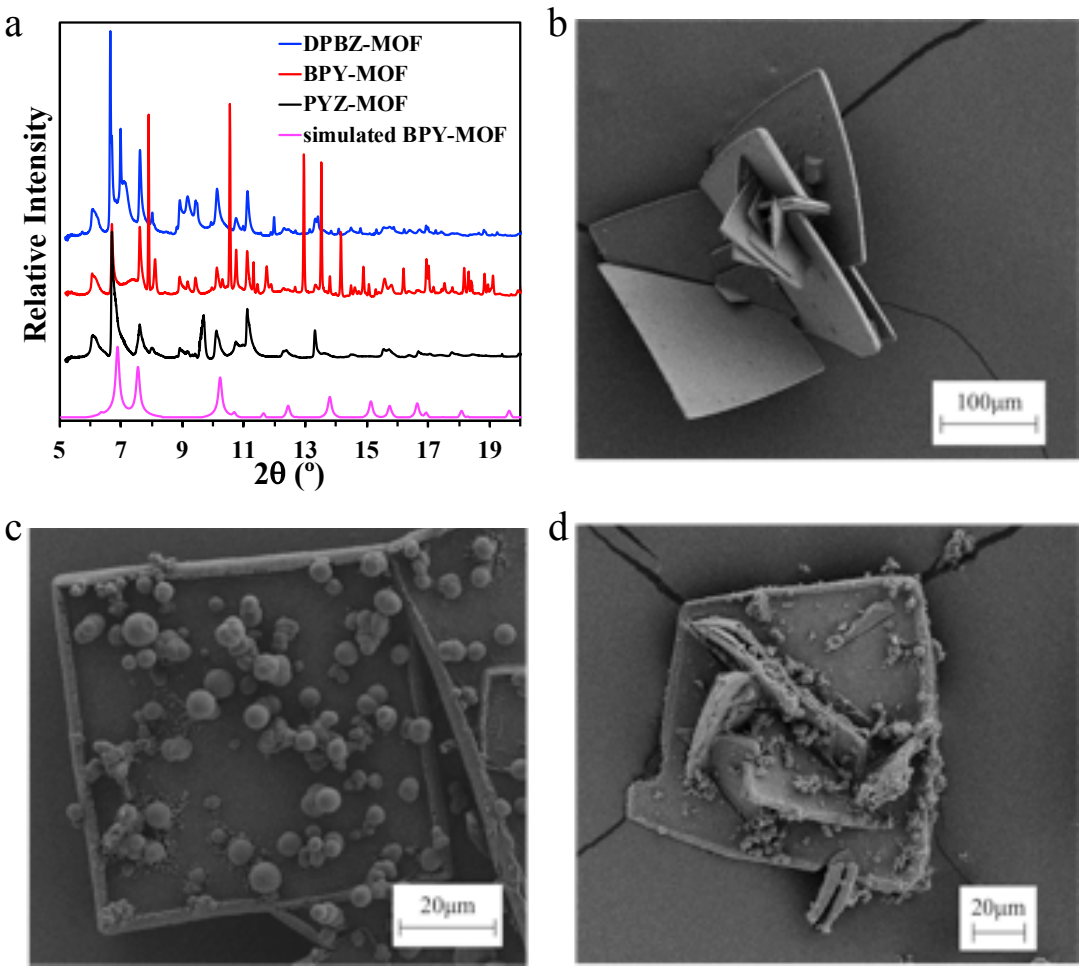

Figure 4.1.3. PXRD patterns (a) calculated from single crystal XRD data of BPY-MOF (black) and experimental PXRD patterns of PYZ-MOF (red), BPY-MOF (blue) and DPBZ-MOF (magenta) along with SEM images of PYZ-MOF (b), BPY-MOF (c) and DPBZ-MOF (d).

4.1.2. Photophysical Properties

The diffuse reflectance spectra and emission spectra of the PYZ-MOF, BPY-MOF and DPBZ-MOF are shown in Figure 4.1.4 along with the absorption and emission spectra of the ZnTCPP compound in DMF (~ 1.8 μM). In dilute DMF solution, ZnTCPP exhibits a soret band (S_0–S_2) with maximum absorbance at 429 nm and Q bands centered around 523 nm, 565 nm and 605 nm (S_0–S_1).[13] The characteristic ZnTCPP soret band and Q bands, are apparent in the diffuse reflectance spectra of the MOFs. The positions of the absorption peaks of the MOFs are unshifted

relative to ZnTCPP in DMF, but are significantly broadened due to strong ZnTCPP aggregation effects.[14] Additionally, absorption band broadening can also result from ligation of the pillar ligand to the Zn-center of TCPP. Such phenomena have been observed for 5-coordinate ZnTCPP-L (species, where L = pyz or bpy).[15] In solution, the emission spectrum of ZnTCPP displays vibronically structured bands at 608 nm and 660 nm, associated with S_2–S_0 and S_1–S_0 transitions, respectively.[16-17] The observed S_2–S_0 emission violates Kasha's rule, which states that photon emission always occurs from the lowest electronic/vibrational excited state of a molecule, ie. S_1 for ZnTCPP.[18] The intensity of the S_1–S_0 transition band is significantly enhanced in the emission spectra of the MOFs. This increase in intensity is attributed complexation of the pillar ligand to ZnTCPP as the molecular symmetry is reduced from D_{4h} to C_{4V}, which gives rise to increased vibrations and consequently, enhanced intensity of formally symmetry forbidden bands.[15] The large redshift observed in the emission spectra of the MOFs is a result of both complexation and aggregation effects.[13,15] The photoluminescence decays of the MOF were recorded using time-correlated single photon counting (TCSPC). The fluorescence decay of ZnTCPP in DMF was measured at 610 nm and fit to a mono-exponential decay, yielding a lifetime (τ) of 2.13 ± 0.01 ns. The fluorescence decays of PYZ-MOF, BPY-MOF and DPBZ-MOF were recorded at 610 nm (Figure 4.3.2) and the corresponding lifetimes are summarized in Table 4.1.1. The fluorescence lifetimes of the PYZ-MOF, BPY-MOF and DPBZ-MOF were found to be 2.00 ± 0.02 ns, 1.94 ± 0.06 ns and 1.98 ± 0.03 ns, respectively. These are in agreement with previously reported lifetime values.[19] Previous studies have shown a correlation between MOF crystallite size and the binding nature of the ligands in the framework, resulting in discrepancies in the photophysical properties of the MOF. [12]

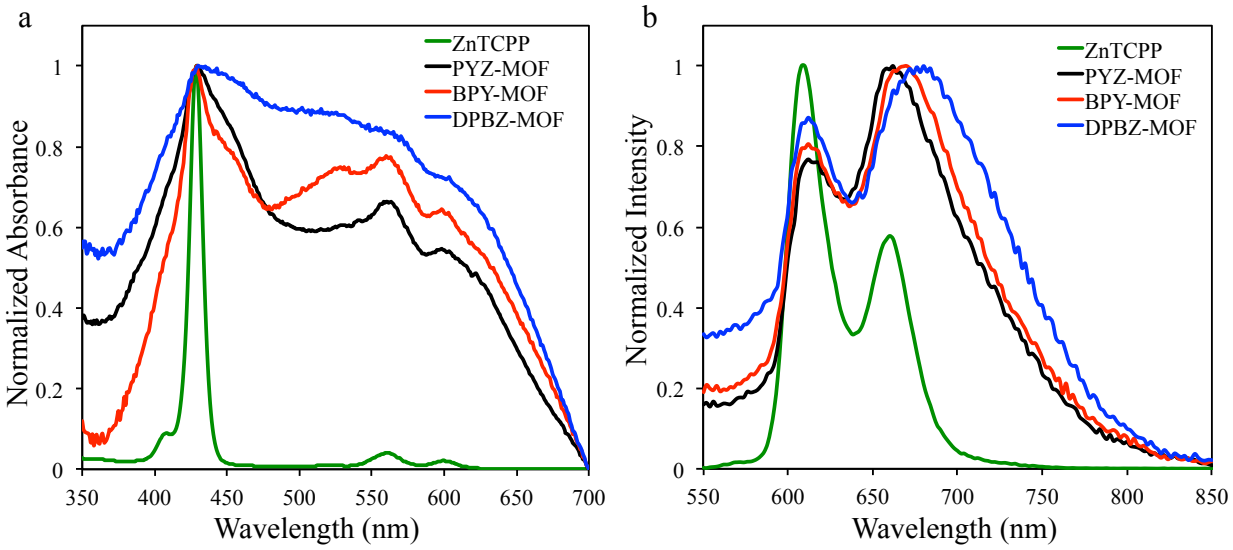

Figure 4.1.4. Diffuse reflectance spectra (a) and emission spectra (b) of ZnTCPP in DMF (green), PYZ-MOF (black), BPY-MOF (red) and DPBZ-MOF (blue), λ_{ex} = 430 nm.

Table 4.1.1. Summary of the photophysical properties of ZnTCPP, PYZ-MOF, BPY-MOF and DPBZ-MOF.

	S_2 λ_{abs} (nm)	S_2 λ_{em} (nm)	S_1 λ_{em} (nm)	τ_1 (ns)
ZnTCPP	429	608	660	2.14 ± 0.09
PYZ-MOF	429	612	662	2.00 ± 0.02
BPY-MOF	429	612	670	1.94 ± 0.05
DPBZ-MOF	429	612	680	1.98 ± 0.03

4.1.3. Fluorescence Quenching Experiments

Fluorescence quenching experiments were carried to gain insight into the effects of ZnTCPP separation distance on the rates of energy transfer. The copper(II) metallated, TCPP (CuTCPP) was chosen as the fluorescence quencher because the Cu(II) compound is non-fluorescent and have been employed in prior studies as efficient quencher of porphyrin emission.[20-22] Although the exact quenching mechanism of CuTCPP is not yet fully understood, some general observations can be derived from these experiments.

The steady-state emission and time resolved luminescence decays of the L2-MOFs were recorded after the addition of 0 – 100 mol % CuTCPP, shown in Figure 4.1.5. Interestingly, the emission intensity of the S_2–S_0 and S1-S_0 bands increases significantly after the of just 1 mol % CuTCPP, until a maximum intensity ~ 3 – 4 mol % observed for all three MOFs. Following the addition of another 1 mol % CuTCPP, florescence quenching is observed. This behavior is attributed to association between the CuTCPP quencher and the MOF.[23] The florescence quenching reaches a plateau after the addition of 50 mol % CuTCPP for PYZ-MOF and BPY-MOF and 70 mol % for DPBZ-MOF. No further quenching is observed in the presence of 100 mol % or excess CuTCPP. The broad, S_1–S_0 emission band is redshifted 4 nm, 10 nm and 14 nm PYZ-MOF, BPY-MOF and DPBZ-MOF in the presence of 100 mol% CuTCPP, respectively. The peak at ~ 725 nm is attributed to scattering of excitation light by the MOF particles. Additionally, no change is observed in the fluorescence lifetimes measured in the absence and presence of CuTCPP at 610 nm and 740 nm. This suggests a static quenching mechanism, such as collisional and/or charge-transfer interactions, is responsible for the observed decreased fluorescence intensity. Time-resolved nanosecond spectroscopic measurements were attempted however, the data was obscured by excessive laser scattering by the MOF crystallites in solution.

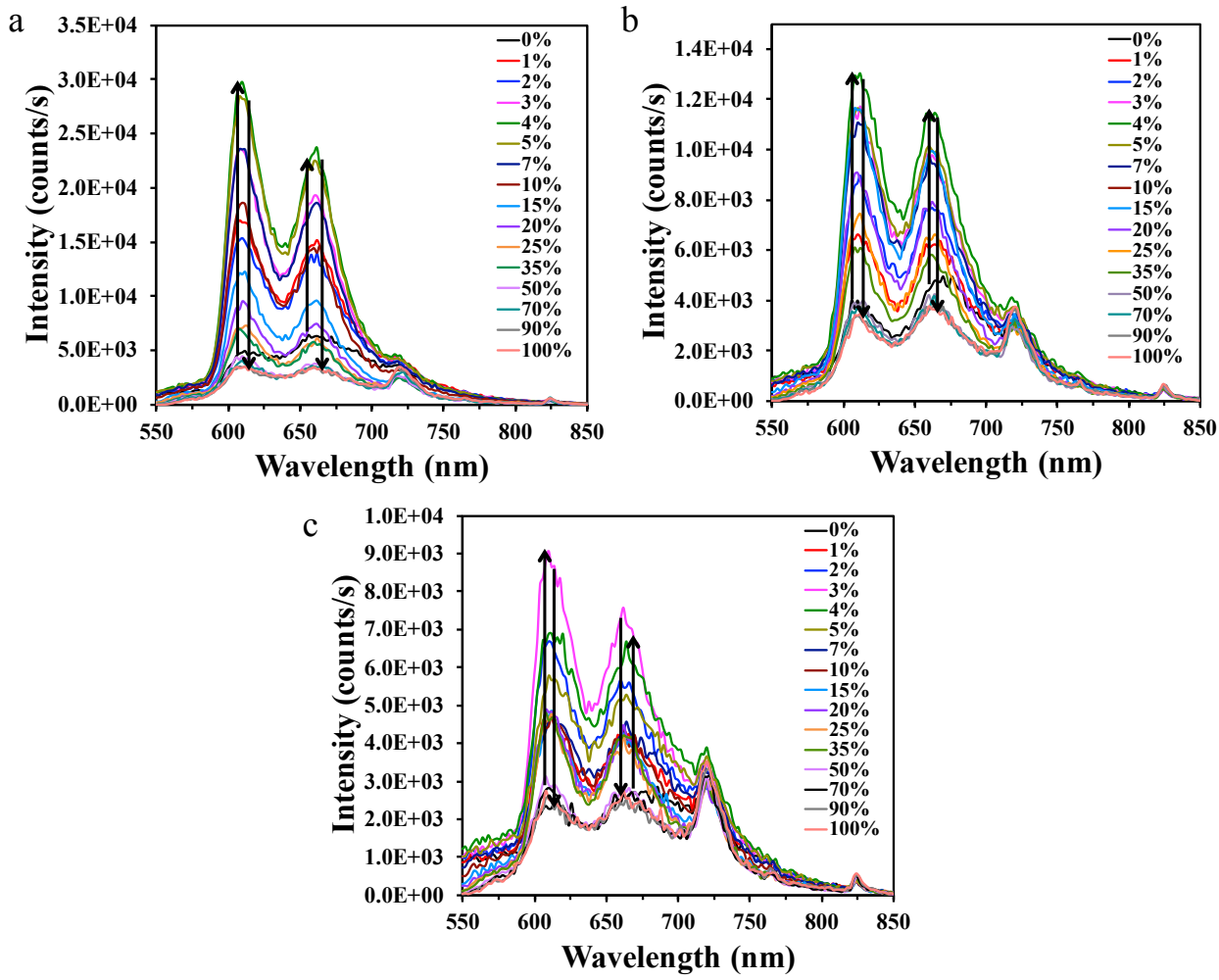

Figure 4.1.5. Steady-state fluorescence quenching of PYZ-MOF (a), BPY-MOF (b) and DPBZ-MOF (c) with increasing [CuTCPP] mol %, measured in DMF, λ_{ex} = 430 nm.

The fluorescence quenching data was analyzed by applying the Stern-Volmer equation (equation 4.1.1), where I_0 and I are the fluorescence intensities in the absence and presence of quencher, [Q] is the concentration of quencher and K_{SV} is the Stern-Volmer quenching constant, given by equation 4.1.2, where k_q is the quenching rate constant and τ_0 the fluorescence lifetime.

$$\frac{I_0}{I} = 1 + K_{SV}[Q] \qquad (4.1.1.)$$

$$K_{SV} = k_q \tau_0 \qquad (4.1.2.)$$

The K_{SV} and k_q values obtained for the L2-MOF series is summarized in Table 4.1.2. As expected, the K_{SV} and k_q values increase with decreasing distance between porphyrins due to enhanced donor-acceptor interactions. Stern-Volmer plots of the dependence of fluorescence intensity as a function quencher concentration exhibit a downward curvature, as shown in Figure 4.1.6. This curvature is attributed to the portion of ZnTCPP moieties inside the MOF that do not come into contact with the CuTCPP quencher. Thus, the fluorescence of these inner chromophores is independent of quencher concentration.[22] This indicates that quenching occurs mainly at the surface of the MOFs and does not migrate the inner ZnTCPP layers, to which the remaining unquenched fluorescence is attributed.

Table 4.1.2. Summary of the Stern-Volmer constants (K_{SV}) and bimolecular quenching rate constants (k_q) obtained for the L2-MOFs.

	K_{SV} (L mol^{-1})	k_q (M^{-1} s^{-1})
PYZ-MOF	13.0×10^{-3}	6.7×10^{-3}
BPY-MOF	07.1×10^{-3}	3.6×10^{-3}
DPBZ-MOF	05.0×10^{-3}	2.5×10^{-3}

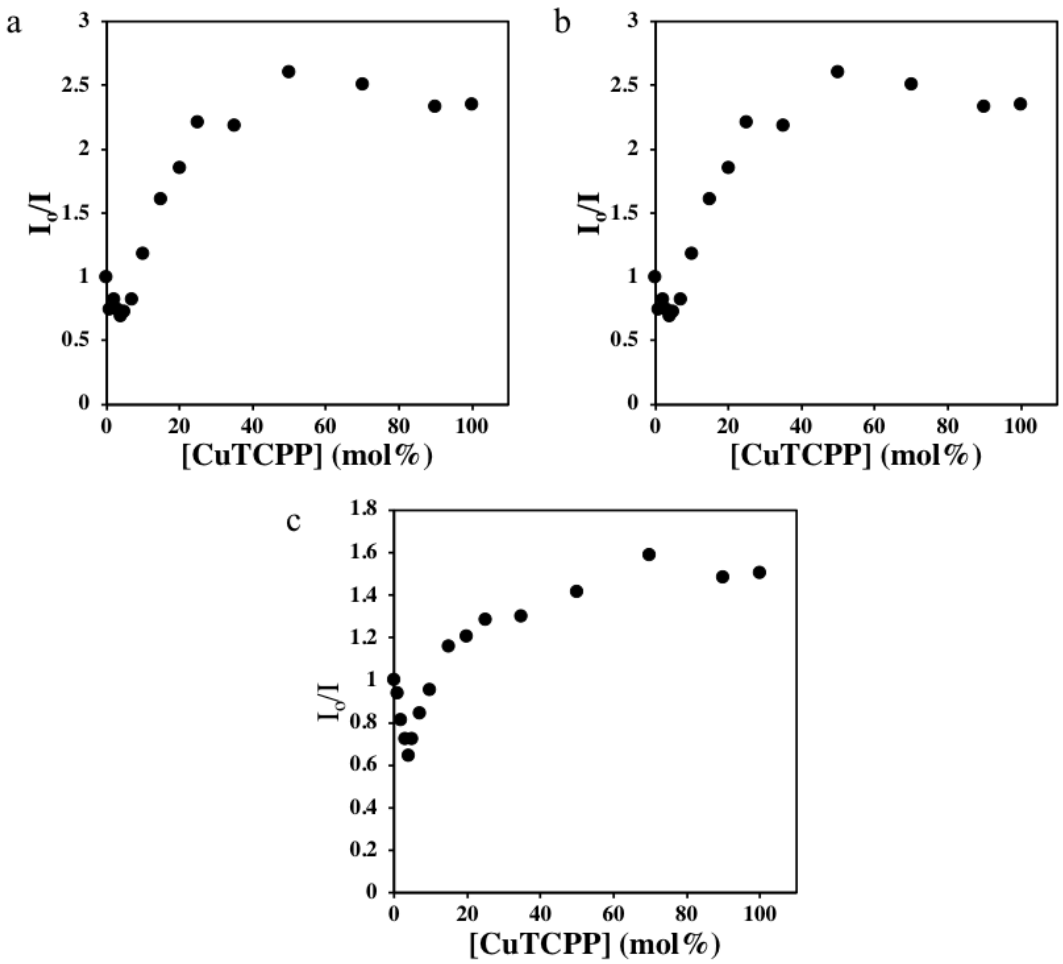

Figure 4.1.6. Stern-Volmer plots for the quenching of fluorescence from PYZ-MOF (a), BPY-MOF (b) and DPBZ-MOF (c).

4.2. Conclusions

In summary, a series of Zn-based MOFs were constructed from ZnTCPP struts and N-heterocyclic pillar ligands of varied lengths. Together, the single-crystal XRD and PXRD data confirm the presence of ZnTCPP/Zn paddlewheel layers and suggest that the layers are linked together through both the ZnO_4 clusters and the Zn of TCPP. The photophysics of the MOFs are dominated by the effects of aggregation, due to the short separation distances between TCPP moieties. These preliminary findings can provide guidance for designing MOF for energy transfer studies.

4.3. Supplemental Information

4.3.1. Materials

1,4-di(4-pyridyl)benzene was synthesized according to literature procedures.[24] All other chemicals and solvents including, meso-tetra(4-carboxyphenyl) porphyrin (H_2TCPP), ZnTCPP, CuTCPP, [1,1′-bis(diphenylphosphino)ferrocene]palladium(II) dichloride (Pd(dppf)Cl_2), pyridine-4-boronic acid, 1,4-dibromobenzene, Na_2CO_3, $ZrCl_4$, pyridine, 4,4′-bipyridine, toluene (reagent grade, > 99%), and *N,N*′-dimethylformamide (DMF, HPLC grade > 99%) were used as received without further purification from Alfa Aesar, Fisher Scientific, or Sigma-Aldrich.

4.3.2. Synthesis of 1,4-di(4-pyridyl)benzene (dpbz)

1,4-di(4-pyridyl)benzene was prepared by the Suzuki coupling of pyridine-4-boronic acid (35 mmol) and 1,4-dibromobenzene (10 mmol),[24] Pd(dppf)$_2Cl_2$ (1 mmol), and Na_2CO_3 (20 mmol) were added to a three neck flask and purged with N_2. 50 mL of deoxygenated 1:1 (v/v) toluene/water was added via cannulation and the solution was refluxed under N_2 for 72 hours with continuous stirring. After cooling to room temperature, the solvent was removed by rotary evaporation. Organic layer was dried over anhydrous $MgSO_4$ and solvent removed via rotary evaporation to afford a brown solid. The product was purified by column chromatography on a silica gel column using 8:5:1 (v/v) ethyl acetate/hexanes/triethylamine as the eluent. Recrystallization from acetonitrile yielded 2.1 mmol of the white dcbz compound. 1H NMR (300 MHz; CDCl3) 8.68,dd,4H; 7.75,s,4H; 7.53,dd,4H.

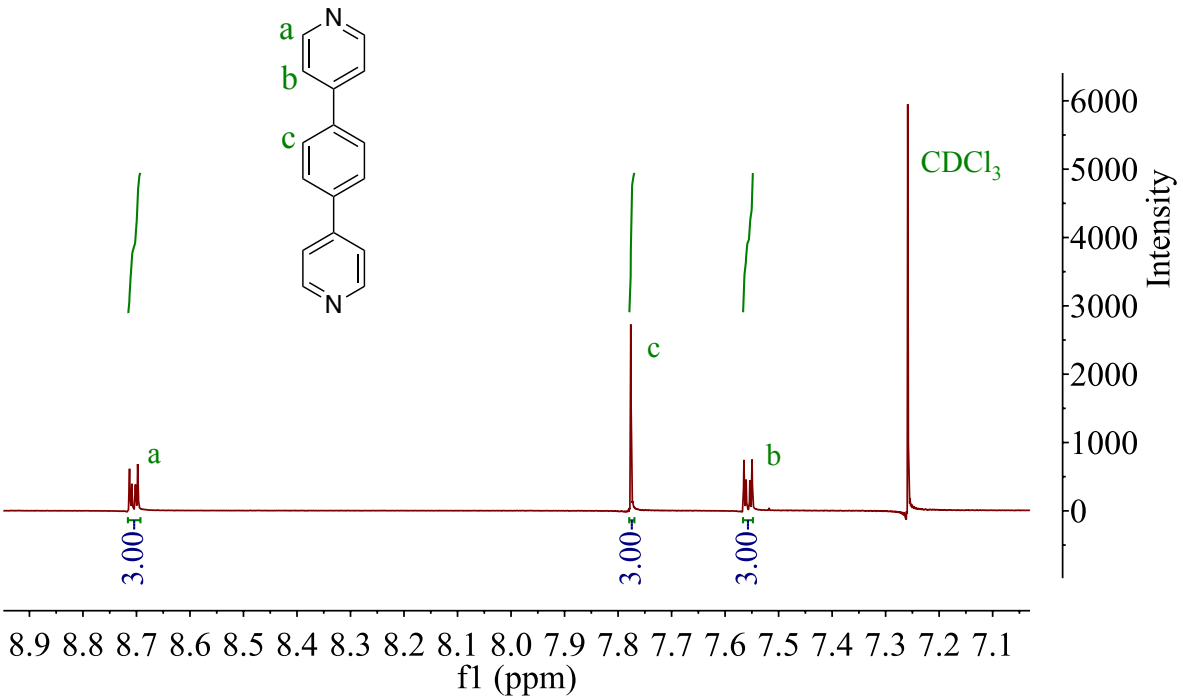

Figure 4.3.1. 1H NMR spectrum of 1,4-di(4-pyridyl)benzene in $CDCl_3$

4.3.3. Scanning Electron Microscopy (SEM)

4.3.3.1. SEM images were collected with a Leo/Zeiss 1550 Schottky field-emission scanning electron microscope equipped with an in-lens detector, operating at 5 kV.

4.3.4. Powder X-ray Diffraction

Synchrotron X-ray powder diffraction of the MOFs were measured on Beamline 17-BM at Advanced Photon Source (APS), Argonne National Laboratory (in Argonne, IL, USA). The X-ray wavelength was 0.45336 Å. The beamline operates in transmission geometry, and is equipped with a PerkinElmer® amorphous silicon area detector that collects two-dimensional diffraction images thru program QXRD.[25] The image data was integrated with program GSAS-II to an XRD profile of the intensity versus 2-theta format.[26]

4.3.5. Single Crystal X-ray Analysis

Single-crystal X-ray diffraction data were collected through the SCrALS (Service Crystallography at Advanced Light Source) program at Beamline 11.3.1 at the Advanced Light Source (ALS), Lawrence Berkeley National Laboratory.

4.3.6. Absorption Spectroscopy

4.3.6.1. Steady-state absorption spectra of the ligands were recorded using an Agilent Technologies 8453 UV-Vis diode array spectrophotometer (1 nm resolution) in a 1 cm quartz cuvette. The same instrument was used to obtain diffuse reflectance spectra of MOF powders, where the sample compartment was replaced with an integration sphere. The powder samples were diluted by mixing with $BaSO_4$.

4.3.7. Steady-State and Time resolved Emission Spectroscopy

Steady-state emission spectra of the porphyrin compounds (~ 1.7 μM) were measured in DMF. 3 mg of the L2-MOF (~ 1.7 μmol of ZnTCPP) were suspended in 2 mL of DMF in a quartz cuvette and the sample was continuously stirred during the emission measurements. A 455 nm short-pass filter was used to reduce scattering of the excitation light. The steady-state emission spectra were obtained using a QuantaMaster Model QM-200-4E where the sample compartment was replaced with an integrating sphere (PTI). The excitation light source was a 75 W Xe arc lamp (Newport). The detector was a thermoelectrically cooled Hamamatsu 1527 photomultiplier tube (PMT).

Time-resolved fluorescence lifetimes were obtained via the time-correlated single photon counting technique (TCSPC) with the same QuantaMaster Model QM-200-4E emission spectrophotometer from Photon Technology, Inc. (PTI) equipped with a 415 nm LED and a Becker & Hickl GmbH PMH-100 PMT detector with time resolution of < 220 ps FWHM. Kinetic traces were analyzed using Origin.

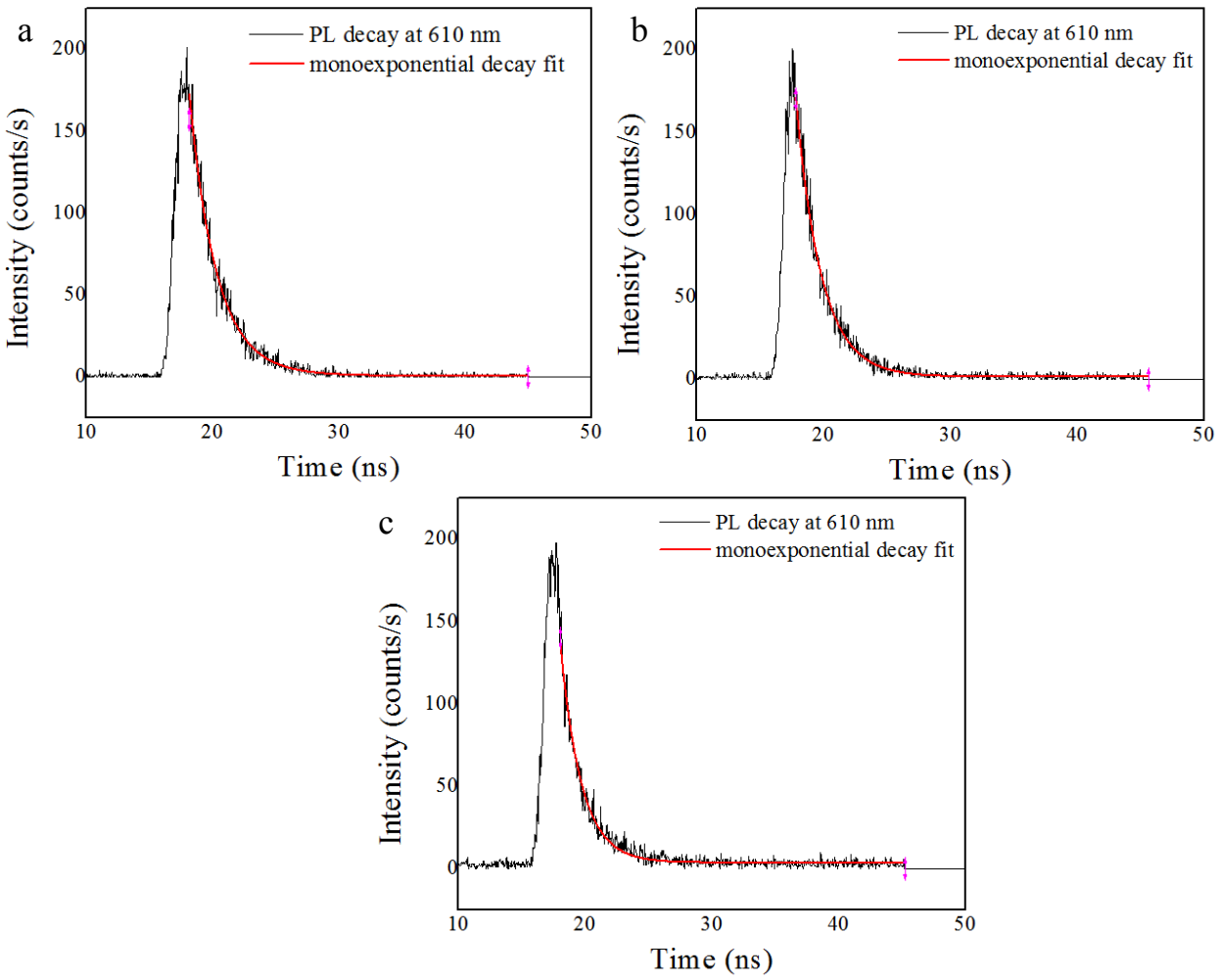

Figure 4.3.2. PYZ-MOF (a) BPY-MOF (b) and DPBZ-MOF emission decay at 610 nm and the monoexponential decay fit (red line). λ_{ex} = 415 nm.

4.4. References

1. Mauzerall, D., Porphyrins, Chlorophyll, and Photosynthesis. In *Photosynthesis I*, 1977; pp 117-124.

2. Kent, C. A.; Mehl, B. P.; Ma, L.; Papanikolas, J. M.; Meyer, T. J.; Lin, W., Energy Transfer Dynamics in Metal−Organic Frameworks. *J. Am Chem. Soc.* **2010,** *132* (37), 12767-12769.

3. Lee, C. Y.; Farha, O. K.; Hong, B. J.; Sarjeant, A. A.; Nguyen, S. T.; Hupp, J. T., Light-Harvesting Metal–Organic Frameworks (MOFs): Efficient Strut-to-Strut Energy Transfer in Bodipy and Porphyrin-Based MOFs. *J. Am Chem. Soc.* **2011,** *133* (40), 15858-15861.

4. Lin, J.; Hu, X.; Zhang, P.; Van Rynbach, A.; Beratan, D. N.; Kent, C. A.; Mehl, B. P.; Papanikolas, J. M.; Meyer, T. J.; Lin, W.; Skourtis, S. S.; Constantinou, M., Triplet Excitation Energy Dynamics in Metal–Organic Frameworks. *J. Phys. Chem.. C.* **2013,** *117* (43), 22250-22259.

5. Maza, W. A.; Morris, A. J., Photophysical Characterization of a Ruthenium(II) Tris(2,2′-bipyridine)-Doped Zirconium UiO-67 Metal–Organic Framework. *J. Phys. Chem.. C.* **2014,** *118* (17), 8803-8817.

6. So, M. C.; Jin, S.; Son, H.-J.; Wiederrecht, G. P.; Farha, O. K.; Hupp, J. T., Layer-by-Layer Fabrication of Oriented Porous Thin Films Based on Porphyrin-Containing Metal–Organic Frameworks. *J. Am Chem. Soc.* **2013,** *135* (42), 15698-15701.

7. Son, H.-J.; Jin, S.; Patwardhan, S.; Wezenberg, S. J.; Jeong, N. C.; So, M.; Wilmer, C. E.; Sarjeant, A. A.; Schatz, G. C.; Snurr, R. Q.; Farha, O. K.; Wiederrecht, G. P.; Hupp, J. T., Light-Harvesting and Ultrafast Energy Migration in Porphyrin-Based Metal–Organic Frameworks. *J. Am Chem. Soc.* **2013,** *135* (2), 862-869.

8. Son, H.-J.; Jin, S.; Patwardhan, S.; Wezenberg, S. J.; Jeong, N. C.; So, M.; Wilmer, C. E.; Sarjeant, A. A.; Schatz, G. C.; Snurr, R. Q.; Farha, O. K.; Wiederrecht, G. P.; Hupp, J. T., Light-Harvesting and Ultrafast Energy Migration in Porphyrin-Based Metal–Organic Frameworks. *J. Am. Chem. Soc.* **2013,** *135* (2), 862-869.

9. Goswami, S.; Ma, L.; Martinson, A. B. F.; Wasielewski, M. R.; K. Farha, O. K.; T. Hupp, J. T. Toward Metal−Organic Framework-Based Solar Cells: Enhancing Directional Exciton

Transport by Collapsing Three-Dimensional Film Structures. *ACS Appl. Mater. Interfaces.* **2016,** *8*, 30863−30870.

10. Choi, E.-Y.; Barron, P. M.; Novotny, R. W.; Son, H.-T.; Hu, C.; Choe, W., Pillared Porphyrin Homologous Series: Intergrowth in Metal−Organic Frameworks. *Inorg, Chem.* **2009,** *48* (2), 426-428.

11. Choi, E.-Y.; Wray, C. A.; Hu, C.; Choe, W., Highly Tunable Metal–Organic Frameworks with Open Metal Centers. *Cryst. Eng. Comm.* **2009,** *11* (4), 553-555.

12. Sakuma, T.; Sakai, H.; Araki, Y.; Wada, T.; Hasobe, T., Control of Local Structures and Photophysical Properties of Zinc Porphyrin-based Supramolecular Assemblies Structurally Organized by Regioselective Ligand Coordination. *Phys. Chem. Chem. Phys.* **2016,** *18* (7), 5453-5463.

13. Karolczak, J.; Kowalska, D.; Lukaszewicz, A.; Maciejewski, A.; Steer, R. P., Photophysical Studies of Porphyrins and Metalloporphyrins: Accurate Measurements of Fluorescence Spectra and Fluorescence Quantum Yields for Soret Band Excitation of Zinc Tetraphenylporphyrin. *J. Phys. Chem. A.* **2004,** *108* (21), 4570-4575.

14. Stevens, A. L.; Joshi, N. K.; Paige, M. F.; Steer, R. P., Photophysics of Zinc Porphyrin Aggregates in Dilute Water–Ethanol Solutions. *J. Phys. Chem. B.* **2017,** *121* (49), 11180-11188.

15. Danger, B. R.; Bedient, K.; Maiti, M.; Burgess, I. J.; Steer, R. P., Photophysics of Self-Assembled Zinc Porphyrin−Bidentate Diamine Ligand Complexes. *J. Phys. Chem. A.* **2010,** *114* (41), 10960-10968.

16. Tripathy, U.; Kowalska, D.; Liu, X.; Velate, S.; Steer, R. P. Photophysics of Soret-Excited Tetrapyrroles in Solution. I. Metalloporphyrins: MgTPP, ZnTPP, and CdTPP. J. Phys. Chem. A 2008, 112, 5824−5833.

17. Tripathy, U.; Steer, R. P. The Photophysics of Metalloporphyrins Excited in Their Soret and Higher Energy UV Absorption Bands. J. Porphyrins Phthalocyanines 2007, 11, 228−243.

18. Kasha, M. *Discuss. Faraday Soc*., **1950,** *9*, 14-19.

19. Donker, H.; van Hoek, A.; van Schaik, W.; Koehorst, R. B. M.; Yatskou, M. M.; Schaafsma, T. J., Spectroscopy and Photophysics of Self-Organized Zinc Porphyrin Nanolayers. 2. Transport Properties of Singlet Excitation. *J. Phys. Chem. B.* **2005,** *109* (36), 17038-17046.

20. Brookfield, R. L.; Ellul, H.; Harriman, A., Luminescence of Porphyrins and Metalloporphyrins. Part 10: Mixed-Metal Dimers. *J. Chem. Soc., Faraday Trans. 2.* **1985,** *81* (12), 1837-1848.

21. Schwarz, F. P.; Gouterman, M.; Muljiani, Z.; H. Dolphin, D., Energy Transfer Between Covalently Linked Metal Porphyrins. *Bioinorg. Chem.* **1972,** *2* (1), 1-32.

22. Lehrer, S., Solute Perturbation of Protein Fluorescence. Quenching of the Tryptophyl Fluorescence of Model Compounds and of Lysozyme by Iodide Ion. *Biochemistry* **2002,** *10* (17), 3254-3263.

23. Otsuki, J.; Takatsuki, M.; Kaneko, M.; Miwa, H.; Takido, T.; Seno, M.; Okamoto, K.; Imahori, H.; Fujitsuka, M.; Araki, Y.; Ito, O.; Fukuzumi, S. Formation of a Supramolecular Porphyrin-Spacer-Acceptor Ternary Complex and Intracomplex Electron Transfer. *J. Phys. Chem. A*. **2003,** *107*, 379-385.

24. Jin, M.-J.; Lee, D.-H., A Practical Heterogeneous Catalyst for the Suzuki, Sonogashira, and Stille Coupling Reactions of Unreactive Aryl Chlorides. *Angew. Chem. Int. Ed.* **2010,** *49* (6), 1119-1122.

25. http://qxrd.sourceforge.net/

26. Toby, B. H.; Von Dreele, R. B., GSAS-II: The Genesis of a Modern Open-Source All-Purpose Crystallography Software Package. *J. Appl. Crystallogr.* **2013,** *46* (2), 544-549.

5. Conclusions and Future Direction

5.1. Conclusions

The influence of chromophore 3D spatial arrangement on the photophysical properties of a material was demonstrated in a series of anthracenedicarboxylate-based MOFs. We have shown that the photophysics of the three anthracene derivatives, 2,6-ADCA and 1,4-ADCA and 9,10-ADCA, are altered to varying degrees upon coordination in a zirconium-based framework, primarily due to the extent of through-space interactions between the chromophores. In the 2,6-MOF, the anthracene units are spatially separated by ~ 13.5 Å and the π– π interactions are negligible. This results in monomeric photophysics, analogous to the free linker in solution. In the 9,10-MOF the anthracene spacing is ~ 7.4 Å and the excited-state properties are very similar to those of the free ligand. On the other hand, the shorter spacing between anthracene units and their orientations in the 1,4-MOF a result in strong π– π interactions that give rise to excimer formation. Additionally, it was demonstrated that luminescent properties of a framework can be controlled by the functionalization of appropriate positions around the anthracene moiety.

Furthermore, the spacing between anthracene chromophores was shown to have a significant effect on TTA-UC efficiency. Specifically, TTA-UC is only observed from the 9-10-MOF. The distance between anthracene linkers in the 2,6-MOF is too large for TTA to occur, while the short distances in the 1,4-MOF hinder upconversion by competitive excimer formation. These results provide guidelines for designing MOFs with the appropriate 3D structure and anthracene spacing to enhance upconversion efficiencies.

To explore the effects of porphyrin spacing on energy transfer efficiencies, a series of ZnTCPP-based pillared paddlewheel MOFs was prepared. The distances between porphyrin layers were controlled by incorporating N-heterocyclic pillar ligands of different lengths in order to explore

the dependence of energy-transfer rates on the distance between porphyrin layers. The ZnTCPP/Zn paddlewheel layers are confirmed by the single-crystal XRD and PXRD data. Additionally, the single-crystal data indicates that the layers are linked through both the ZnO_4 clusters and the Zn of TCPP. Aggregate effects dominate the photophysical properties of the MOFs, due to the short spacing between ZnTCPP moieties. Florescence quenching measurements revealed that the ZnTCPP emission is not fully quenched in the presence of excess CuTCPP. Stern-Volmer analyses yielded a Stern-Volmer constants (K_{SV}) and bimolecular quenching rate constants (k_q) Stern-Volmer plots of the quenching data showed a downward curved shape for all three MOFs in the series. This is attributed to florescence from ZnTCPP moieties inside the MOF. Thus, quenching occurs mainly at the surface of the MOFs and energy does not migrate from ZnTCPP further inside the MOF to fully quench the emission.

5.2. Future Direction

5.2.1.1. Sensitized Photon Upconversion in MOFs

The work presented in this dissertation has provided insight into the structure-photophysical property relationship in metal-organic frameworks, specifically, the spatial arrangement of chromophores required to achieve sensitized photon upconversion. Future studies are aimed at developing MOFs with enhanced UC efficiencies. To this end, future work should aim to define other factors, such as appropriate chromophore concentrations in the MOF and further control to optimize over orbital and dipole overlap. Synthetic approaches should focus on developing MOFs with optimal chromophore geometries that are reasonable stable to laser irradiation and solvent suspension. The 2,6-ADCA and 1,4-ADCA ligands could be incorporated into MOFs based on other metal nodes in order to optimize the distances and orientations of the anthracene moieties and achieve TTA-UC. Preparation of MOFs that contain both the sensitizer and acceptor molecules

within the framework could overcome the concentration limit that contributes to low UC efficiency of the 9,10-MOF MOF. This could be achieved by synthesizing mixed ligand MOFs with appropriate chromophore arrangements.[1-2] Additionally, integration of an acceptor chromophore with a near-unity florescence quantum yield would further improve the overall upconversion yields.[3] Finally, near-IR to visible photon upconversion is ideal for solar energy conversion applications. Future efforts to tune the absorption and emission wavelengths of the MOF in order to achieve near-IR to visible upconversion should focus on determining chromophores with the appropriate photophysical and structural properties.[4]

5.2.1.2. Energy Transfer Dynamics in Porphyrinic MOFs

The work herein has also shown that the efficiency of energy transfer can be enhanced by tuning the distance between MOF porphyrin layers. A large initial increase of florescence intensity was observed in the fluorescence quenching measurements with CuTCPP. To avoid this feature, fluorescence quenching studies are currently underway in our lab, using a lanthanide quencher, such as a Gd^{3+}. The effects of porphyrin spacing on energy transfer efficiency as well as the quenching mechanism will be assessed from these studies.[5] Additionally, the Ln^{3+} may be changed to investigate the different mechanisms of energy transfer in the MOFs.[5] Subsequent studies may be aimed at determining the dependence on porphyrin separation in the distances of energy migration within the MOF.[6] Finally, development of a thin-film preparation of the MOFs may allow for transient absorption studies of these materials.

5.3. References

1. Monica C. So, M. C.; Wiederrecht, G. P.; Mondloch, J. E.; Hupp, J. T.; Farhaa. O. K. Metal-Organic Framework Materials for Light-Harvesting and Energy Transfer. *Chem*. *Commun*. **2015,** *51*, 3501-3510.

2. Singh-Rachford, T. N.; Castellano, F. N., Photon upconversion based on sensitized triplet–triplet annihilation. *Coord. Chem. Rev.* **2010,** *254* (21-22), 2560-2573.

3. Arslan, H. K.; Shekhah, O.; Wieland, D. C. F.; Paulus, M.; Sternemann, C.; Schroer, M. A. Tiemeyer, S.; Tolan, M.; Fischer, R. A.; Wöll, C. Intercalation in Layered Metal-Organic Frameworks: Reversible Inclusion of an Extended π-System. *J. Am. Chem. Soc.* **2011,** *133*, 8158–8161.

3. Amemori, S.; Sasaki, Y.; Yanai, N; Kimizuka, N. Near-Infrared-to-Visible Photon Upconversion Sensitized by a Metal Complex with Spin-Forbidden yet Strong S_0−T_1 Absorption. *J. Am. Chem. Soc*. **2016,** *138*, 8702−8705.

4. Chrysochoos, J; Beyene, K Oxidative Fluorescence Quenching of Zinc Tetraphenylporphyrin (ZnTPP) by Trivalent Lanthanide Ions in Several Solvents: Role of Lanthanide-Induced Singlet–Triplet Crossing. *J. Lumen*. **1999,** *81* 209-218.

5. Son, H.-J.; Jin, S.; Patwardhan, S.; Wezenberg, S. J.; Jeong, N. C.; So, M.; Wilmer, C. E.; Sarjeant, A. A.; Schatz, G. C.; Snurr, R. Q.; Farha, O. K.; Wiederrecht, G. P.; Hupp, J. T., Light-Harvesting and Ultrafast Energy Migration in Porphyrin-Based Metal–Organic Frameworks. *J. Am Chem. Soc.* **2013,** *135* (2), 862-869.